

# Magnetic nanowires and nanotubes with modulated diameters

Dissertation  
zur Erlangung des Doktorgrades  
des Department Physik  
der Universität Hamburg

vorgelegt von  
Eva Kristina Monika Pitzschel  
geb. Reckwell  
aus Haltern/Recklinghausen

Hamburg 2012

Gutachter der Dissertation: Prof. Dr. K. Nielsch  
Prof. Dr. M. Albrecht

Gutachter der Disputation: Prof. Dr. K. Nielsch  
Prof. Dr. H.-P. Oepen

Datum der Disputation: 26.03.2012

Vorsitzender des Prüfungsausschusses: Prof. Dr. M. Rübhausen

Vorsitzender des Promotionsausschusses: Prof. Dr. P. Hauschildt

Dekan der MIN-Fakultät: Prof. Dr. H. Graener

## Abstract

In this dissertation different material systems of magnetic nanostructures are presented, either on the one hand, nanowires and on the other hand, nanotubes. These nanostructures should work as models for the implementation of new data storage applications which should be realized with the controlled motion of magnetic domain walls. Anodic alumina membranes are utilized as templates in which mild and hard anodizations were combined to yield modulations in pore diameter. These diameter modulations should act as nucleation points for the controlled pinning and depinning of domain walls. Nanowires are fabricated by electrodeposition and nanotubes by atomic layer deposition (ALD). Their magnetic properties strongly depend on the presence of diameter modulations both on the ensemble scale and at the single-object level. Theoretical modeling emphasizes the major influence of the magnetostatic interactions between neighboring wires and tubes.

In the first section, nickel nanowires are presented. In single-object measurements it is possible to observe hints of domain wall pinning in some cases. That the pinning occurs at the modulation remains to be shown and should be shown in future studies. Additionally, in the nanowires presented here the pinning is not systematic. Most likely, the energy difference of a domain wall between thick and thin wire segments is too small with respect to the influence of magnetocrystalline anisotropy and thermal fluctuations. Such factors would introduce a stochastic component into the pinning phenomena. Further, the presence of modulations also affects the magnetic properties of wire ensembles. In a simple theoretical framework it is possible to account for the differences between the various types of modulated wires and calculate their enhanced interaction in the array. The model shows limitations for multiple modulations: it is considered this as a likely sign that the diameter modulations influence either the nucleation domain boundaries or their propagation.

In the second part, iron III oxide nanotubes are presented. It is shown, that also here designed structural irregularities have consequences of prime importance on the magnetic characteristics of the tubes as in nanowires. Last, nickel and nickel/cobalt nanotubes are introduced. Starting from nickel, this is the first time the nickel/cobalt alloy is successfully synthesized by ALD from nickelocene, cobaltocene and ozone. The results demonstrate the validity of utilizing porous alumina as a template system for the creation of 3D-nanoobjects modulated in diameter like the prior shown iron III oxide nanotubes.

## Kurzfassung

In dieser Arbeit werden verschiedene magnetische Materialsysteme, zum einen als Nanostäbchen und zum anderen als Nanoröhrchen, vorgestellt und deren magnetische Eigenschaften untersucht. Diese Nanostrukturen können als Modellsysteme für Anwendungen neuartiger Speichermedien verwendet werden, welche mit Hilfe der kontrollierten Domänenwandbewegung arbeiten. Anodische Aluminium-

oxidmembranen werden als Templat verwendet, wobei harte und milde Anodisierung kombiniert wird, um so Durchmessermodulationen im Porendurchmesser zu erhalten. Diese Durchmessermodulationen sollen als Nukleationspunkte für das kontrollierte Pinnen und Depinnen von Domänenwänden dienen. Nickel Nanostäbchen werden durch Elektrodeposition und Eisenoxid, Nickel und Nickel/ Cobalt Nanoröhrchen werden durch Atomlagenabscheidung(ALD) hergestellt. Die magnetischen Eigenschaften dieser Nanostrukturen hängen von der Existenz der Modulationen ab, ob nun als Ensemble vermessen, aber auch in Einzel-messungen läßt sich dies bestätigen. Theoretische Modelle unterstreichen die große Bedeutung der magnetostatischen Wechselwirkungen zwischen benachbarten Stäbchen und Röhrchen. Das Präparationskonzept läßt sich ohne weiteres auf andere Systeme übertragen. Zunächst werden Nickel Nanostäbchen vorgestellt. Einzel-objekt Messungen weisen auf, dass in manchen Fällen ein Domänenwandpinnen auftritt. Ein direktes Pinnen an der Modulation kann noch nicht gezeigt werden. Es erweist sich auch, dass das Pinnen, der hier gezeigten Nanostäbchen, nicht systematisch ist. Wahrscheinlich ist der Unterschied der Energiedifferenz der Domänenwände zwischen dicken und dünnen Segmenten der Stäbchen zu klein im Gegensatz zum Einfluss der magnetotokristallinen Anisotropie und zum Einfluss von thermischen Fluktationen. Solche Faktoren führen eine stochastische Komponente im Pinningprozess ein. Ferner zeigen die Ensemble Messungen auch den Einfluss der Durchmessermodulationen. In einem einfachen theoretischen Modell ist es möglich die Unterschiede zwischen den verschiedenen modulierten Proben zu berücksichtigen und deren Wechselwirkungen zu berechnen. Das Modell kann mehrfach modulierte Proben nicht ausreichend beschreiben, es wird als Anzeichen gedeutet, dass die Durchmessermodulationen die Entstehung und Ausbreitung von Domänenwänden beeinflussen.

Als zweites werden Eisenoxid Nanoröhrchen präsentiert. Auch hier wird der Einfluss der Probenmodulationen auf das magnetische Verhalten gezeigt, genau wie bei den Nanostäbchen. Zuletzt werden Nickel und Nickel/ Cobalt Nanoröhrchen vorgestellt. Ausgehend vom Nickel, wird hier ist das erste Mal die erfolgreiche Synthetisierung von Nickel/ Cobalt als Legierung durch ALD von Nickelocene, Cobaltocene und Ozon gezeigt.

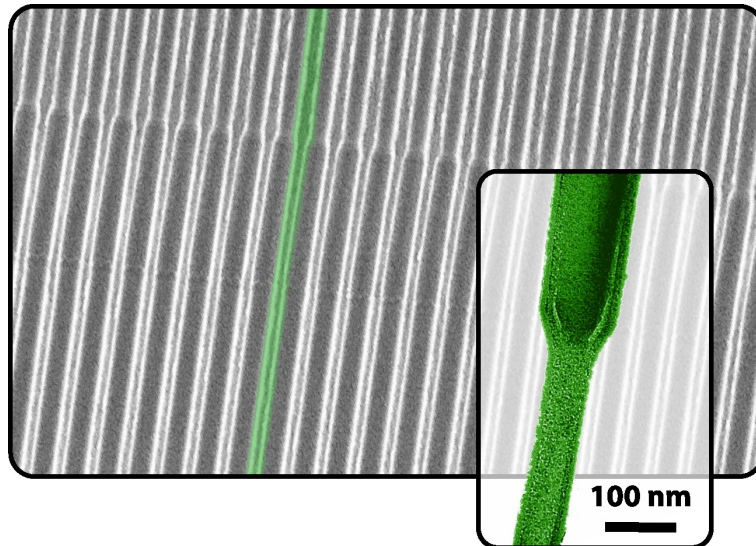
Die Ergebnisse unterstreichen die erfolgreiche Verwendung von anodischen Aluminiumoxid Membranen als Templatsystem zur Herstellung von 3D-Nanoobjekten mit kontrollierten Durchmessermodulationen, genauso wie bei den zuvor gezeigten Eisenoxid Röhrchen.

# Contents

<b>1. Introduction</b>	<b>7</b>
<b>2. Theory</b>	<b>9</b>
2.1. Ferromagnetism . . . . .	9
2.2. Magnetic domains . . . . .	15
2.3. Simulations . . . . .	22
2.4. Magnetic configuration and reversal in nanowires and nanotubes . . .	24
2.5. Superparamagnetism . . . . .	31
<b>3. Preparation</b>	<b>34</b>
3.1. Template . . . . .	34
3.1.1. Self-ordered anodic alumina membranes . . . . .	40
3.1.2. Perfectly ordered anodic alumina membranes . . . . .	42
3.2. Filling of the template . . . . .	45
3.2.1. Nanowires by electrodeposition . . . . .	46
3.2.2. Nanotubes by Atomic Layer Deposition . . . . .	48
3.3. Overview of the prepared samples . . . . .	55
<b>4. Structural and magnetic characterization methods</b>	<b>57</b>
4.1. Structural characterization . . . . .	57
4.2. Magnetic characterization . . . . .	59
4.2.1. Magnetometry of ensemble nanowires and nanotubes . . . . .	59
4.2.2. Magnetometry of single nanowires . . . . .	65
<b>5. Ni nanowires</b>	<b>69</b>
5.1. Introduction . . . . .	69
5.2. Magnetic measurements . . . . .	71
5.2.1. Properties of isolated nickel nanowires . . . . .	71
5.2.2. Influence of dipolar interactions in nickel wire ensembles . . . .	74
<b>6. Fe<sub>3</sub>O<sub>4</sub> nanotubes</b>	<b>80</b>
6.1. Introduction . . . . .	80
6.2. Magnetic measurements and theoretical treatment . . . . .	83
<b>7. Ni and NiCo nanotubes</b>	<b>94</b>
7.1. Ni nanotubes . . . . .	94
7.1.1. Introduction . . . . .	94
7.1.2. Magnetic measurements . . . . .	95
7.2. NiCo nanotubes . . . . .	98

7.2.1. Introduction . . . . .	98
7.2.2. Magnetic measurements . . . . .	99
<b>8. Summary</b>	<b>108</b>
<b>Bibliography</b>	<b>110</b>
<b>A. Appendix</b>	<b>127</b>
A.1. ALD process parameters . . . . .	127
<b>B. Appendix</b>	<b>129</b>
B.1. Figures . . . . .	129
B.1.1. Ni tubes hysteresis loops . . . . .	129
B.1.2. Nickel/ cobalt tubes hysteresis loops . . . . .	131
B.2. Simulation figures of Ni nanowires . . . . .	132
<b>C. Appendix</b>	<b>134</b>
C.1. Publications . . . . .	134
C.2. Presentations . . . . .	134

# 1. Introduction



The controlled motions of magnetic domain walls would allow the implementation of a novel data storage platform, that is, more robust and less energy-intensive than current hard disk drives, which base on the internal magnetization of Weiss domains[PHT08]. The physical basis for this type of storage for the controlled manipulation of a large number of domain boundaries, however, has not been completely laid down to date. The most widespread experimental approach amounts in the definition of elongated sub-micron structures with geometrical features defined so as to either nucleate the formation of a domain wall or block (pin) its propagation at well-defined positions. Electron beam lithography has been the most widely used preparative method to this goal, as it enables one to arbitrarily define notches or wire diameter changes as pinning centers[ORZ<sup>+</sup>09, HTM<sup>+</sup>08]. However, e-beam lithography is a serial technique and limited to the definition of one nanostructure at a time. Additionally, because it bases on structuring of a thin film, it is limited to generating wires of quadrangular cross-section. Here, in this thesis a general preparative strategy towards large numbers ( $> 10^8$ ) of confined 3D-cylindrical metal nanowires and nanotubes arranged in arrays is investigated and in which diameter modulations can be introduced at arbitrarily defined positions.

Chapter 2 provides a theoretical basis for the comprehension of the physical phenomena discussed in this thesis.

In this thesis, on the one hand, (i) the utilization of a nanoimprinted, perfectly ordered anodic alumina membrane as a porous template defining length and diameter of the wires and tubes as well as their hexagonal order, and on the other

hand (ii) the conformal filling of the cylindrical pores with magnetic substances by electrodeposition and Atomic Layer Deposition furnishes large numbers of objects in a simple procedure, is shown. The synthesis methods are presented in the chapter 3. In chapter 4 the reader is provided an insight into the available measurement setups for the structural and magnetic characterization of the nanowires and nanotubes. On the one hand, the inductive magnetometry is used to analyze the magnetic properties of nanowires and nanotubes by the superconducting quantum interference device (SQUID)- and the vibrating (VSM) magnetometer in ensembles and on the other hand, single-object measurements were done with the magneto-optical Kerr effect (MOKE). In this thesis different material systems and structures were analyzed: Nanowires made out of nickel, nanotubes comprising iron III oxide, nickel and nickel/ cobalt alloy. This thesis reports on their magnetic properties (chapter 5 to 7).

In the magnetism realm, diameter modulations should provide a handle over the motion of magnetic domain walls, a phenomenon proposed as it was already said before a future data storage platform. In this thesis different materials were synthesized such as the classical material nickel by electrodeposition for nanowires and also nickeloxide as well as the magnetite iron III oxide and last a new implemented procedure of the material nickel/ cobalt by ALD for nanotubes. The switching behavior of such nanostructures was analyzed, especially with different possibilities to influence the magnetization reversal by domain wall pinning. There are questions concerning the created diameter modulation which should serve as nucleation points for the pinning and depinning of domain walls. Which reversal processes are possible in such nanowires and nanotubes? Is it possible to block and observe a domain wall?



## 2. Theory

This chapter provides a theoretical basis for the comprehension of the physical phenomena discussed in this thesis. After a brief introduction into ferromagnetism[Aha96], the focus is laid on the magnetic behavior of 2D-nanostructures, thereafter extended to 3D-nanostructures: nanowires and nanotubes which are the topics of this thesis. Features of and influence on superparamagnetism will follow.

### 2.1. Ferromagnetism

In absence of an external magnetic field, ferromagnetic materials show a spontaneous magnetization  $M_S$  below a critical temperature, the Curie temperature  $T_C$ .

This is characteristic of ferromagnetic materials, in contrast to paramagnetic materials. Paramagnetic moments are not aligned parallel as in ferromagnetic materials, they are oriented randomly in a zero magnetic field. The magnetic moments in ferromagnetic materials are aligned along a defined direction in volume with a certain size called magnetic domains. The atomic spins in ferromagnetic materials interact, each trying to align with the others. In paramagnetism, the atoms interact only with the external magnetic field. In this case no domains exist. Even if in a ferromagnet, collective magnetism and an alignment of the spins is prevailed, accordingly a sample with properly aligned domains can have an outwardly disappearing magnetic moment.

A magnetized sample can be described by a sum of real and auxiliary fields, which characterize its energetic state. There are delineated energy contributions which can be used for calculating the final magnetization configurations.

Two magnetic dipoles  $\mu_1$  and  $\mu_2$  with a distance  $r$  have the energy:

$$E_{\text{dipol}} = \frac{\mu_0}{4\pi r^3} \left[ \mu_1 \cdot \mu_2 - \frac{3}{r^2} (\mu_1 \cdot \mathbf{r}) (\mu_2 \cdot \mathbf{r}) \right]. \quad (2.1)$$

This energy contribution is proportional to  $\frac{1}{r^3}$  and equates a temperature of 1 K[Blu01] for two neighboring atoms, therefore this dipol-dipol-interaction can not be accountable for the alignment of the magnetic moments in a ferromagnet at high  $T_C$ . This interaction plays a role in the consideration of the demagnetization energy and will be discussed in the following paragraph. So, to understand which magnetic configuration is formed in a sample, the total energy of the system has to be considered. If temperature dependent effects are neglected, an energy which is only dependent on the variation of the vector field  $\vec{M}$  relative to the applied field

and sample geometry can be obtained.

$$E_{\text{tot}} = E_{Z_e} + E_E + E_A + E_{D_e} \quad (2.2)$$

Local and non-local energies are distinguished by the fact, whether the whole sample or only the immediate neighborings of a macro-spin are considered. These energies are now described and distinguished.

The first energy which is going to be introduced is the **Zeeman energy**.

The existence of an applied magnetic field influences the magnetization. It results from long-range dipole-dipole interaction.

$$E_{Z_e} = -\mu_0 \int \vec{H}_{\text{ext}} \vec{M} \quad (2.3)$$

Equation 2.3 describes the interaction of the magnetization  $\vec{M}$  of a sample with an external magnetic field  $\vec{H}_{\text{ext}}$ . It is minimal if  $\vec{M}$  is parallel to the external field  $\vec{H}_{\text{ext}}$ . In a homogeneous external field only the average magnetization of the sample contributes this energy.

The **exchange energy** is the next mentioned energy term in the equation (2.2). It comes from interaction with its neighbors in the lattice without accounting for the sample geometry.

$$E_E = -2 \sum_{i \neq j} J_{ij} \vec{s}_i \vec{s}_j \quad (2.4)$$

The Heisenberg model describes the exchange energy between two lattice atoms with spins  $s_i$  and  $s_j$ . Each spin  $\vec{s}$  generates a magnetic moment  $\vec{\mu} = -g\mu_B\vec{s}$ , where  $g$  is the  $g$ -factor and  $\mu_B$  the Bohr magneton. The exchange integral  $J_{ij}$  is purely from quantummechanical origin and is connected to the overlap of charge distribution of atoms  $i$  and  $j$ . If  $J_{ij}$  is positive, the energy is minimized for parallel aligned spins, the angle between the neighboring moments is small and the material behaves ferromagnetic. In the opposite case, the spins are aligned antiparallel and the behavior of the sample is antiferromagnetic. For this model only the distance between the considered spins  $s_i$  and  $s_j$  is important; there is no anisotropy. The exchange energy is a short range, local energy. Areas with ordered magnetic moments are called Weiss domains. Anisotropic behavior can not be described by the Heisenberg Model, so other energy terms have to be added to complete a magnetic description.

The **crystalline anisotropic energy** is a non-isotropic energy and includes the dependence of the magnetic properties in a preferred direction, in bulk materials the crystalline anisotropy is most crucial. The magnetization always shows one direction which is considered the 'easy' axis and is most preferred or the 'hard' axis. The reason for this preference is the crystal structure. In the 'easy' axis direction the saturation magnetization (the state in which all spins are aligned in one direction at certain field), is reached at minimum applied field in comparison to the 'hard' axis where higher fields have to be applied to saturate the sample. Moreover, in the 'easy' axis the coercive field, the field which is needed to zero the magnetization, is even higher than in the case of the 'hard' axis. The anisotropy energy is the energy needed to change the direction of the magnetization from the

easy axis to the hard axis without modifying the relative orientation of the spins. However, on the one hand, a rotation of the magnetization relative to the crystal axis changes the electrostatic interactions with two neighboring charge distributions and on the other hand the exchange energy.

The cause of the magnetic crystalline anisotropy is the spin-orbit interaction of electrons. The electron sheath of a lattice atom overlaps with its neighbors differently. Both states are characterized by the amount of overlap of the atomic orbitals. The easy axis has a larger overlap. This asymmetry comes from the interaction of the crystal structure in combination with the deviation of the charge distribution from the spherical geometry. In Fig. 2.1 the anisotropy energy surface for a cubic fcc nickel crystal is shown. The difference between hard and easy axis is illustrated, one easy axis is representatively illustrated. The figure shows the dimension of the anisotropy energy dependent on the crystal axis. The energy

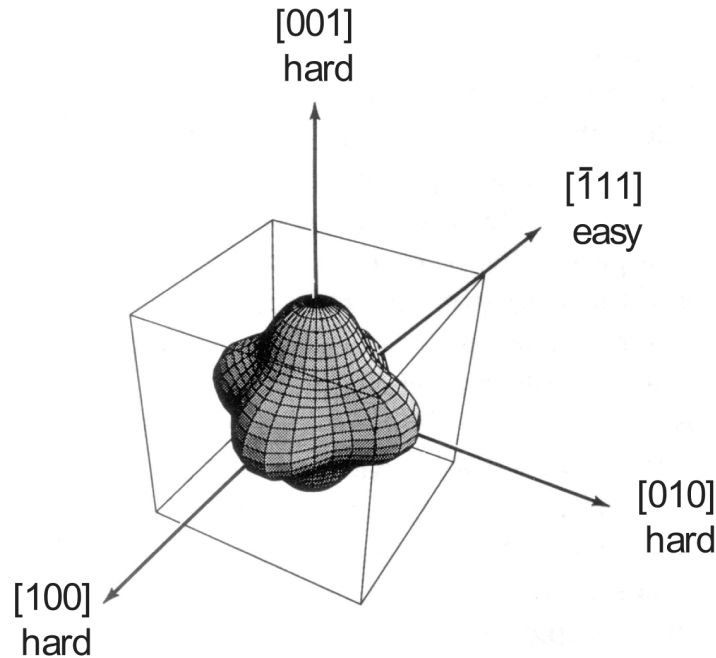


**Figure 2.1.:** The figure illustrates the anisotropy energy surface for a cubic crystal fcc Ni[[Pri94](#)].

density is specified, if  $\phi$  is the angle towards magnetization and magnetocrystalline graphical favored direction[[Nie02](#)]. The algebraic sign of the anisotropy constants defines the direction of the angle towards magnetization and magnetocrystalline graphical favored direction, and if there is a minimum or a maximum of energy density. The easy axis can be along the crystal axis or diagonal.

$$E_A = K_1 \sin^2 \phi + K_2 \sin^4 \phi + O(6) \quad (2.5)$$

$K_1$  and  $K_2$  are the anisotropy constants. The magnetocrystalline anisotropy at room temperature for nickel is

$$K_1 = -4,5 \cdot 10^3 \frac{\text{J}}{\text{m}^3} \text{ and for cobalt is } K_1 = +4,1 \cdot 10^5 \frac{\text{J}}{\text{m}^3} [\text{Kit99}].$$

Magnetic anisotropies can also originate from other symmetry breakings e.g. nearby interfaces.

The **border and surface anisotropy** is formed through the symmetry breaking at the interface. At both sides of the interface there are neighbors or rather on the surface there are only few neighbors to interact with each other. The interface of thin films are the boundaries to air on the one hand, and to the substrate on the other hand. For wires there is only one surface, the boundary to air, which gains in importance. For tubes the surface is accordingly larger. So, the interface anisotropy is not negligible and plays a big role in the full anisotropy for a small volume relative to its surface. An anisotropic behavior is developed. In this thesis the diameter of the nanostructures is  $> 40$  nm and so this anisotropy is negligible[Bö9].

Finally, the **shape anisotropy energy** will be mentioned as a non-local energy-contribution.

It is considered that a magnetic volume consists of single dipoles which are interacting with each other. So, to evaluate the resulting energy contribution of an auxiliary field, the so-called demagnetization field is introduced. At a certain point, one has to consider the generated dipol-field from every other spin. From the Maxwell-equations one can obtain:

$$\vec{\nabla} \vec{H}_{dem} = -\vec{\nabla} \vec{M} \quad (2.6)$$

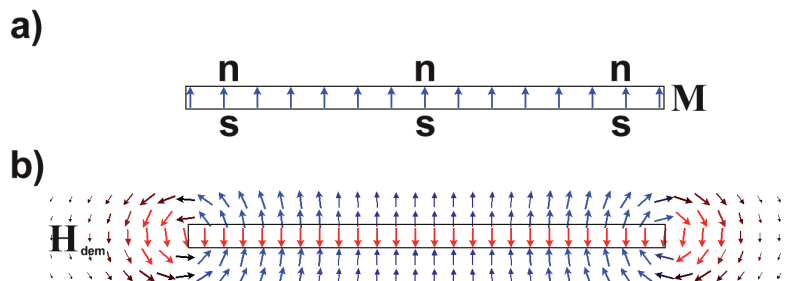


**Figure 2.2.:** In (a) shows the out-of-plane magnetization of a long rectangular sample, inside the sample there is the self-demagnetization field  $\vec{H}_{dem}$ . The energy term is responsible for the shape anisotropy. (b) Illustrates the resulting demagnetization field, the strayfield ( $\vec{H}_{stray}$ ) outside the sample. It is a dipolar-field, there are no magnetic monopoles[Mar10].

So, the gradient of  $\vec{M}$  results an additional field in equation 2.2: The so-called demagnetization field. This can be separated into the external stray field and the internal demagnetization field (see figure 2.2). By solving equation 2.6 (Poisson, Helmholtz) the calculation of  $\vec{H}_{dem}$  is possible. In part (a) of figure 2.2 the out-of-plane magnetization of a long rectangular sample is illustrated. (b) shows both fields,  $\vec{H}_{dem}$  and  $\vec{H}_{stray}$ , respectively, which are responsible for the shape anisotropy. This can be simulated e.g. with the program OOMMF (object oriented micromagnetic framework)[DP99]. More details can be found in the section simulations (2.3). The self-demagnetization field inside the sample can be easily specified for ellipsoids because it is constant inside the magnetic volume.

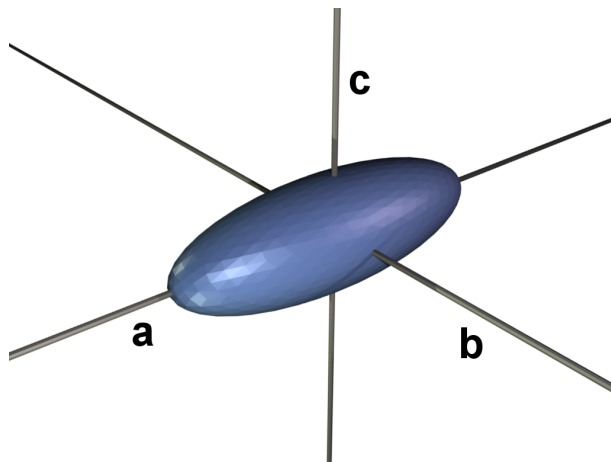


**Figure 2.3.:** The illustration of an ellipsoid and its principal axes[Mar10].

Therefore, it can be described with the tensor  $\hat{N}$ .

$$\vec{H}_{dem} = -\hat{N}\vec{M} \quad (2.7)$$

The self-demagnetizing tensor  $\hat{N}$  depends only on the length and orientation of the principal axes relative to  $\vec{M}$ . Along the principal axes, which are shown in figure 2.3, it can be simplified to:

$$\vec{H}_{dem} = - \begin{pmatrix} N_x & M_x \\ N_y & M_y \\ N_z & M_z \end{pmatrix} \quad (2.8)$$

In general, there is no uniform internal field. But a shape approximation is possible, e.g. for a plane or cylinder. Figure 2.4 shows a sphere and an infinite cylinder. For an infinite cylinder which is magnetized parallel to its axis, the demagnetization field is zero. The samples fabricated in this thesis are of cylindrical shape. The cylinders are finite in their length, so that the demagnetization field is not zero at their ends because here the magnetization is perpendicular to the cylinder surface. This results in a stray field of a dipole from far away. This is illustrated in figure 2.5 which was simulated with the program nmag[Mar10, FFBF07]. For the samples used in this thesis a demagnetization factor for small partial volumes is assumed (s. chapter 5). Due to the large aspect

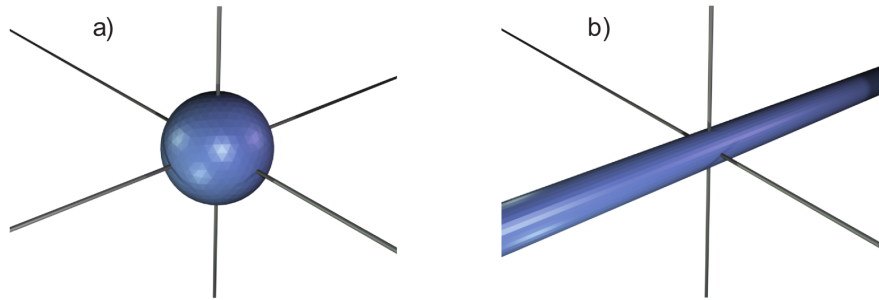


**Figure 2.4.:** (a) For a sphere the demagnetization tensor  $\hat{N}$  is  $\frac{1}{3}$  for the x, y, z components. The stray field is similar to that of a point-dipole observed from far away. (b) Shows an infinite cylinder.  $N_x = 0$  and  $N_y = N_z = 0.5$ . The magnetization  $\vec{M}$  is parallel to  $n_x$ . The demagnetization field is zero ( $\vec{H}_{dem} = 0$ )[\[Mar10\]](#)

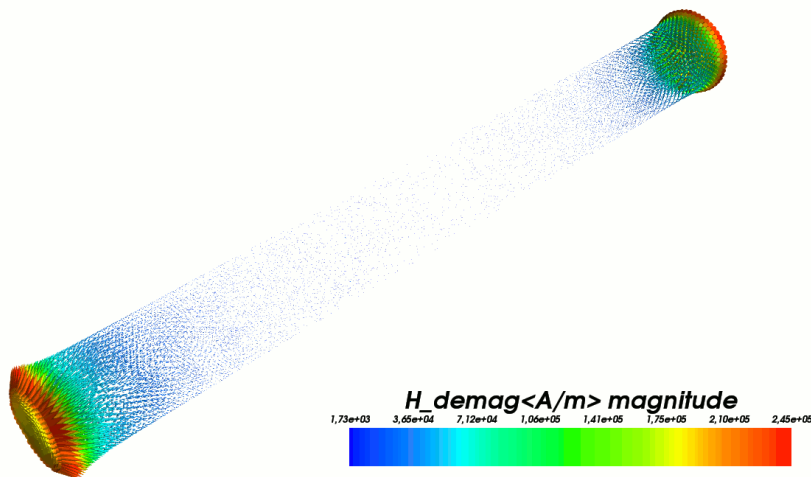


**Figure 2.5.:** The saturated or remanent state of a finite cylinder is shown. The cylinder has a finite length. For this reason the  $H_{dem} \neq 0$  at the ends of the cylinder. A stray field has to be calculated. The configuration illustrated here is energetically favored, because the self-demagnetization field is vertical at the ends of the wire[\[Mar10\]](#)

ratio the easy axis is along the wire axis. In other words, in most parts of the surface the magnetization is parallel to the wire axis, apart from the end faces there are no stray fields.

So, the configuration illustrated in figure 2.5 is energetically favored, because the magnetization is parallel to the cylindrical shell, so that there are no stray field sources existing.

According to that, because of the high shape anisotropy in the cylindrical wires and tubes with high aspect ratio, there will be different reversal fields dependent on the orientation of the applied field. Because of this, the demagnetization factor for the long and thin structures is important. If the structure is perpendicular to  $H_{\text{ext}}$  and  $M$  is aligned into this direction the strayfield is high, if  $H_{\text{ext}}$  parallel to the structure is only at the end of the sample.

## 2.2. Magnetic domains

The existence of domains is the consequence of energy minimization[LL35]. This section provides the reader with a small insight to the magnetic configuration in different nanostructures. It starts with the bulk system and thin films, and comes from 2D-nanostructures to the subject treated here: The 3D-nanowires and -nanotubes.

Magnetic domains are small regions in ferromagnetic materials, characterized by a parallel alignment of the magnetic moments. So, here the magnetization is uniform[Jil91]. This is characteristic for ferromagnetic materials (see section 1), which shows this spontaneous magnetization  $M_S$  below the Curie temperature  $T_C$ . A spontaneous magnetization in a ferromagnet does not generally mean that all magnetic moments of the sample are aligned parallel[Kit99]. Energetically it is mostly favorable if the spontaneous magnetization is divided into single parts with different directions. This results in an overall smaller magnetization value of the structure. Consequently, there is a domain structure. The magnetization intends to split into domains because the principle is always to avoid stray fields. The domain structure is influenced by the shape of the sample. Figure 2.6 (a) illustrates a multi-domain state. It is the so-called Landau pattern. There is almost no stray field and the demagnetization energy is minimized. This pattern is the energetically favorable configuration in zero applied field. The regions of homogeneous magnetization are separated by a domain wall. A domain wall is the barrier in which the magnetization turns from the magnetization in the first domain to the direction of the magnetization in the second. Figure 2.6 (b) shows a one-domain state. The exchange energy is minimal all spins are aligned parallel. Now, the demagnetization energy is high; there is a large stray field.

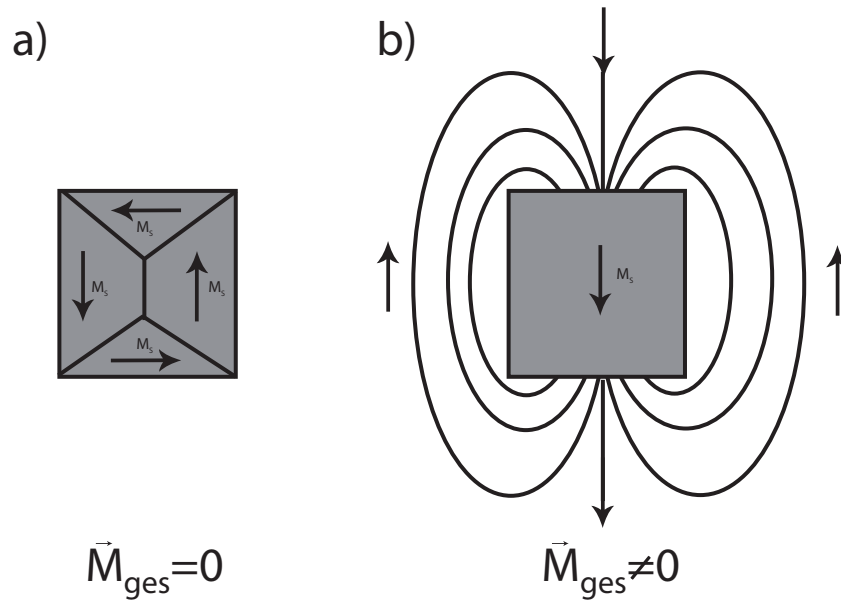


**Figure 2.6.:** Different magnetic domains illustrated with the spontaneous magnetization  $\vec{M}_S$ . (a) shows a multi-domain state the so-called Landau-pattern and (b) shows a one-domain state. The ferromagnet in the left part has four closed connected domains. The vectorsum of the magnetization is zero. The one-domain magnetization of a ferromagnet generates an increase of the inside magnetic field (which is not shown) and of the stray field [Nie02].

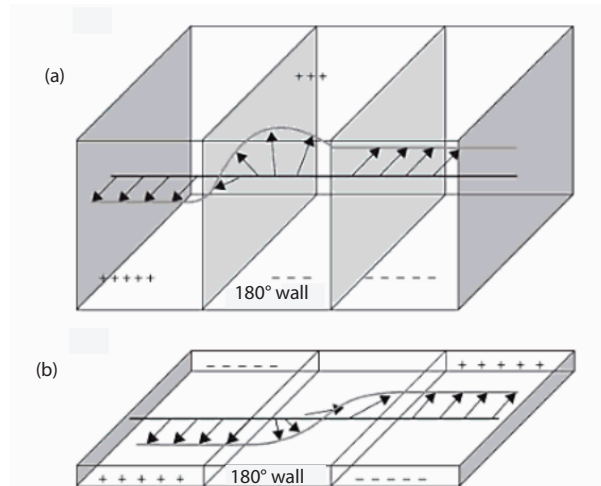


**Figure 2.7.:** The figure illustrates two different domain wall types. In a thick film (a) the Block wall appears, the magnetic moments rotate out-of-plane (plane described by  $\vec{M}$  about an angle of  $180^\circ$  perpendicular to the connection axis between the domains). In the figure (b) Néel wall is shown, it characterizes the magnetic domains in thin films. The spins rotate here in the plane of the magnetic film. Equal to [TL10].



In bulk systems the Bloch wall (s. figure 2.7) mainly appears. The magnetization rotates about an angle of  $180^\circ$  perpendicular to the connecting line between the domains. For thin films the magnetic moments rotate in the plane of the film, this is the so-called Néel wall. The characteristic width of domain walls is connected to the exchange energy. The exchange length  $l_{ex}$  is defined by the exchange constant  $A$  and saturated magnetization  $M_{sat}$ .

$$l_{ex} = \sqrt{2A/\mu_0 M_{sat}^2} \quad (2.9)$$

For iron III oxide, nickel and cobalt the exchange length is about 3 to  $9 \times 10^{-9}$  m [Lin02] according to the chosen values for the exchange constant and saturation magnetization at a certain temperature. This will be discussed further on in section 4. For a detailed description of the presence of magnetic domains the reader is referred to [Jil91].

## Hysteresis

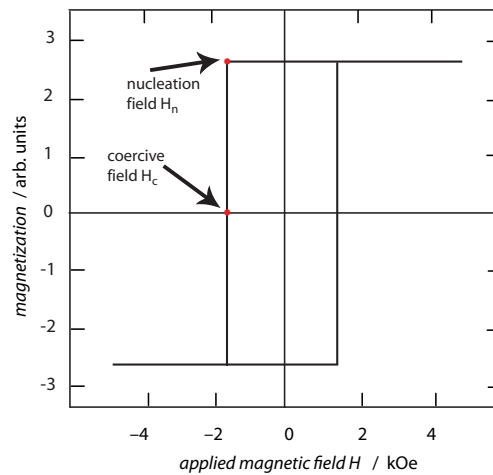


**Figure 2.8.:** Schematic illustration of a hysteresis loop. The magnetization is obtained parallel to the applied field. The ferromagnet's spins all switch coherently, so the nucleation field, switching field and coercive field has the same value.

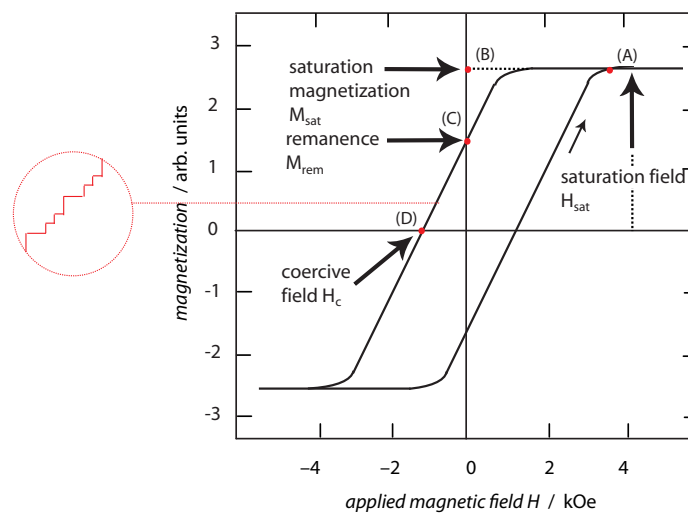


**Figure 2.9.:** Schematic illustration of a hysteresis loop. The magnetization is obtained parallel to the applied field. The magnetization  $M$  is assigned to the ordinate and the applied field  $H$  to the abscissa. The intersection of the magnetization curve with the ordinate is called remnance  $M_{\text{rem}}$ , the intersection with the abscissa is defined as the coercive field  $H_c$  [Nie02]. In a small inset the so-called Barkhausen jumps are illustrated. These discontinuous changes of the magnetization can be found in ferromagnetic samples while changing the applied field. More details can be found in the literature [Kne62].

Based on the nucleation of domains in nanostructures the magnetization has a typical hysteretic behavior in ferromagnetic nanostructures which is schematically shown in figure 2.8 for single nanowires or nanotubes.

Figure 2.8 illustrates a hysteresis curve of a sample where the nucleation and switching field (magnetization is changing the first time from saturation magnetization) and the coercive field (magnetization is zero) are the same. All spins in this ferromagnet switch coherently.

If the magnetization of a ferromagnetic ensemble sample is measured in a field-dependent measurement, the sample will be first saturated (small arrow in figure 2.9). At 4 kOe the saturation field (A) is found in the illustration. In (B) the saturated magnetization can be determined. The field is then decreased, the nucleation field is the field defined at the point where the magnetization is changing the first time from the saturation magnetization (see figure 2.9).

The squareness is also a parameter which can be investigated from these observables. It is defined as the fraction of the magnetization between the  $M_{sat}$  and the remanent state  $M_{rem}$ .

In a small inset the so-called Barkhausen jumps are illustrated, these discontinuous changes of the magnetization can be found in ferromagnetic samples while changing the applied field. The magnetization is not changing in a continuous way, but rather in small differences. These are called the Barkhausen jumps which were demonstrated at first by Heinrich Barkhausen in an acoustic way[Bar30]. More details can be found in the literature[Kne62]. Subsequently, if the field is then decreasing to zero there is still a remanent magnetization which is shown in (C). The field which is needed to zero the magnetization is the coercive field (D). After this first part of the hysteresis loop, where the field comes from high positive fields to high negative fields, the magnetization is measured again from negative to positive fields, so that the hysteresis loop is closed (there is an axis symmetry).

### Cylindrical confined 2D-nanostructures

The magnetic domains of 2D-nanostructures have been analyzed for a long period of time[HB94, Fas98, Cho97, Joh98, FB68]. More complex structures can be fabricated by structuring films with e-beam lithography[HOB<sup>+</sup>96, SMV<sup>+</sup>98, WFA<sup>v</sup>M98, MKG<sup>+</sup>98, CKA<sup>+</sup>99] and characterized.

This subsection encloses a small view into confined cylindrical 2D-nanostructures leading to the topic of 3D-nanowires and nanotubes which is considered in this thesis. Confined cylindrical 2D-nanostructures and cylindrical 3D-nanowires and -nanotubes show new magnetic effects that do not appear in planar films.

For these structures the lateral size and thickness of the magnetic layer are the most important parameters[SW48]. Plane circular structures prefer two different magnetic configurations after a high saturation, in remanence the single-domain state and the vortex configuration.

The two configurations are dependent on the geometric parameters of the sample. If the sample has a thicker layer and a large size the vortex mode is the state found most prominently[CKA<sup>+</sup>99].

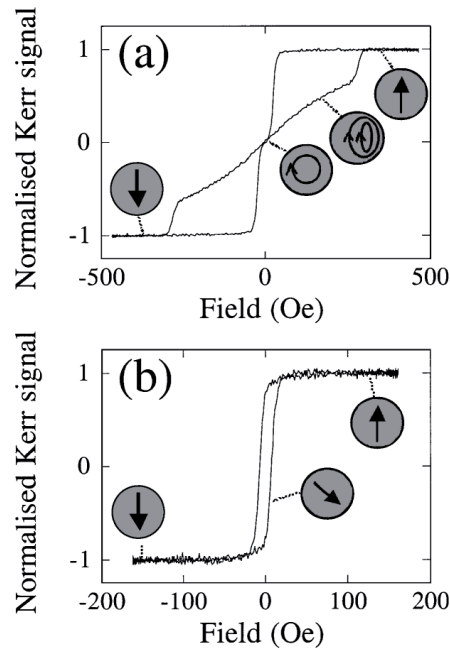


**Figure 2.10.:** Hysteresis loops measured from nanomagnets of diameter ( $d$ ) and thickness ( $t$ ): (a)  $d=300$  nm,  $t=10$  nm; (b)  $d=100$  nm,  $t=10$  nm. The schematic annotation shows the magnetization within a circular nanomagnet, assuming a field oriented up the page[CKA<sup>+</sup>99].

In this state the magnetization is oriented inside the sample in a circular alignment. The external flux of the magnetization is vanished (see figure 2.10 (a)). If the structures are small and thin, another single-domain state is favored (see figure 2.10 (b)), but  $\vec{M}$  points in one fixed direction.

Submicron rings exhibit additional magnetic effects. Here, the ring width is also one of the characteristic parameters to find different magnetostatic configurations during a hysteresis loop. The magnetization can adopt the so-called onion state with a rotating magnetization  $\vec{M}$  (in opposite to the single domain state with  $\vec{M}$  pointing in one direction) and two domain walls (in opposite to the vortex state without any domain) and the opposite state of the onion-like state, the so-called reversed onion state.

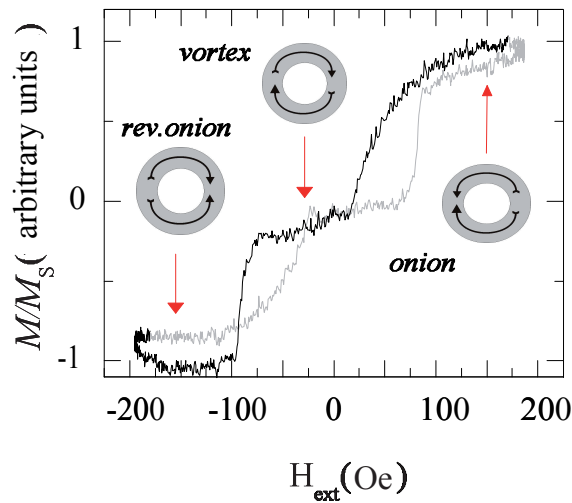


**Figure 2.11.:** Illustration of a MOKE measurement of a monolayered ringstructure. The MOKE signal is normalized to +1 and -1 and is proportional to  $\frac{M_x}{M_s}$  [Rec07].

Figure 2.11 shows a MOKE-measurement of an ensemble of 50 monolayered rings (ring width of 600 nm), evaporated with a 26 nm thick permalloy layer [Rec07]. Permalloy is an alloy consisting of 80 % nickel and 20 % iron. It is a soft magnetic material with a small magnetocrystalline anisotropy, so that the shape anisotropy plays the biggest role and can be analyzed. The MOKE signal is normalized to  $M_s$  and is proportional to  $M_x$ . The field is applied sinusoidal with a frequency of 3 Hz and is varied between  $-180$  Oe and  $+180$  Oe. The loop is symmetric, the vortex is there where it is expected at  $H_{\text{ext}} = 0$ , and is jumping out at 90 Oe on both sides. Schematic illustrations are also shown in the figure 2.11. Through the irreversible jumps in the loop single states can be identified which will be explained later in the paragraph. There are two hysteresis branches, which are differentiated in gray and black color. The first half of the hysteresis (black) starts at high positive fields and ends at negative fields, the gray branch is the opposite taken from negative to positive field values. With the help of MOKE-measurements and simulations the magnetostatic states of monolayered cobaltrings were analyzed in 2001 [RKLD<sup>+</sup>01]. Saturation at high fields allow the ringstructures to obtain the onion state. This state is reached during the increasing of the applied field. There the flux of the magnetization is closed in every half of the ring by nucleating two domain walls. These domain walls are called head-to-head and tail-to-tail domain wall (figure 2.11). Simulations yield a direct transition from the onion-state to the the reversed onion for symmetric rings. Domain walls start to move in the same direction and when they reach the opposite side the reversed-onion state is achieved. Every asymmetry effects the domain walls and let them move forward differently. The vortex configuration is nucleated if the domain walls meet and annihilate. This state is formed at small applied fields which is shown in figure 2.11. The next switching field, which identifies the transition between vortex and reversed onion,

appears at small negative fields. This configuration results from the nucleation of a opposite domain wall in the half of the ring with an antiparallel aligned magnetization to the applied field. There are two domain walls nucleated to form the reversed onion state[LDRKB01].

## 2.3. Simulations

After the introduction of cylindrical confined 2D-nanostructures and before the 3D-nanostructures will be presented, micromagnetic simulations micromagnetic simulations and Monte Carlo simulations are shortly introduced. In past it has been shown that analytical models have their limitations, so simulations are also important to understand the reversal process in 3D- nanostructures. Micromagnetic simulations and Monte Carlo simulations can be used to calculate the reversal modes for nanostructures. The differences between both methods are described and contrasted. In the end of the section the chosen calculation method for some example used here<sup>1</sup>, is demonstrated.

### Micromagnetic simulations and Monte Carlo simulations

Micromagnetic and Monte Carlo simulations are two methods which are used to solve magnetic problems. Micromagnetic simulations are based on an equation of motion called the Landau-Lifshitz-Gilbert-Equation. The Monte Carlo Simulations are based on statical physics. Micromagnetic simulation programs are free available using different approaches to solve differential equations.

On the one hand, there is the finite element method (FEM) that is realized in the programs nmag[FBBF07] and magpar[SFS+03]. On the other hand, stands the finite difference method (FDM), which is used in OOMMF[DP99].

In section 2.1 the consideration of the total energy is introduced. It deals with the interactions between magnetic moments. To understand which magnetic configuration is formed in a sample, the total energy has to be considered which consists of several energy terms.

In contrast to the statics in this description, now time-dependent micromagnetic problems have to be solved, therefore, an equation of motion is needed.

In this equation the time-dependent magnetization is described dependent on a so-called effective field which consists of the several energy contributions (see equation 2.2) and damping.

1935 the Landau-Lifshitz equation was introduced by Landau and Lifshitz[LL35].

The LLG is an ordinary differential equation. This equation was formed to describe the precessional motion of the magnetization in a solid with the incorporating effective field.

$$\frac{d\mathbf{M}}{dt} = \gamma (\mathbf{M} \times \mathbf{H}_{\text{eff}}) - \frac{\lambda}{M_S^2} \mathbf{M} \times (\mathbf{M} \times \mathbf{H}_{\text{eff}}) , \quad (2.10)$$

---

<sup>1</sup>done by Juan Escrig

$\gamma$  is the Landau-Lifshitz-damping parameter which contains the inverse relaxation time  $\tau$  and consequently is a frequency. Later, the equation was modified by Gilbert to the Landau-Lifshitz-Gilbert-equation (LLG)[LL35, Gil55].

$$\frac{d\mathbf{M}}{dt} = \underbrace{\gamma (\mathbf{M} \times \mathbf{H}_{\text{eff}})}_{\text{precession term}} - \underbrace{\frac{\alpha}{M_S} \left( \mathbf{M} \times \frac{d\mathbf{M}}{dt} \right)}_{\text{damping term}}, \quad (2.11)$$

Here, the movement of a velocity dependent (viscous) damping is described, the  $\alpha$  is the dimensionless Gilbert-damping parameter. Both equations (2.10 and 2.11) are equal for small dampings. Furthermore, in equation extra terms for current-driven measurements could be added if necessary. Both methods start in comparable ways (see figure 2.12): First, parameters are purported such as the magnetization, the external field, the material constant and the damping factor. The numerical approach includes the discretization of the total energy, the magnetization and the magnetostatic (the calculation of the fields) done by solving the differential equation. To accomplish this, the so-called mesh is generated. With the calculated fields ( $H_{\text{tot}}$ ), the right hand side of the LLG can be calculated. It can be solved and therefore applied to reach the new time step:

$$\frac{\partial M}{\partial t} = f(t, \vec{M}, \vec{H}) \quad (2.12)$$

That means, values are put on the right hand side of the LLG-equation. Both methods have advantages and disadvantages and can be adopted to the individual case.

The FEM needs surface elements to calculate the demagnetization fields. This method calculates the stray field between bodies, but there is no idea how big it is in between them. Respectively, the space outside the nanostructure is not taken into account. This is a main difference to the FDM. With the FDM the space is discretized with cuboids in the whole volume. To consider these stray field dipol-dipol-interaction between these cuboids, a demagnetization tensor is needed which describes the stray field of a body at every certain point. The calculation of the stray field is solved with the convolution of  $M_i$  with the demagnetization-tensors  $N_i$ .

With the FDM method the stray fields can be considered, this is important for comparing the ensemble measurements of nanowires and nanotubes with the theory. The dipole-dipole-interactions between the wires and tubes in an array are so taken into account and displayed. This method is used for the simulation of the reversal modes of nanowires analyzed here in this thesis (see figure B.4, figure B.5, figure B.6, figure B.7 and figure 5.3), but the coercive fields discussed in this thesis, were calculated analytically (see section 2.4).

With the LLG-equation which is used in both methods, it is not possible to solve thermic problems. There is no additional term which accounts the thermodynamic problems. An approach with temperatures like random movement (perturbation) do not result in realistic solutions. With Monte Carlo simulations, thermal problems can be solved. As said before in this thesis, the basis of Monte Carlo simulations is

statistical physics. The MCS consists of the calculation of the energy difference between initial and final states and the consideration of the related probability at the transition. During one Monte Carlo step a state of the system is dived by chance. The energy difference of the single spin before and afterwards the spin-flip is calculated within the Metropolis algorithm[MRR<sup>+</sup>53]. To calculate the initial and final energy , all relevant energy-terms from equation 2.2 have been considered. Because the MSC uses single crystal lattice elements, the Hamiltonian comprises a simple dip-dip-interaction-expression in contrast to the complicated calculation of the demagnetization field in FDM/ FEM. The related spin-flip-probability is proportional to the Boltzmann factor. Due to simulations on the atomic scale, a scaling method was developed to extend this method to  $\mu\text{m}$  range structures.

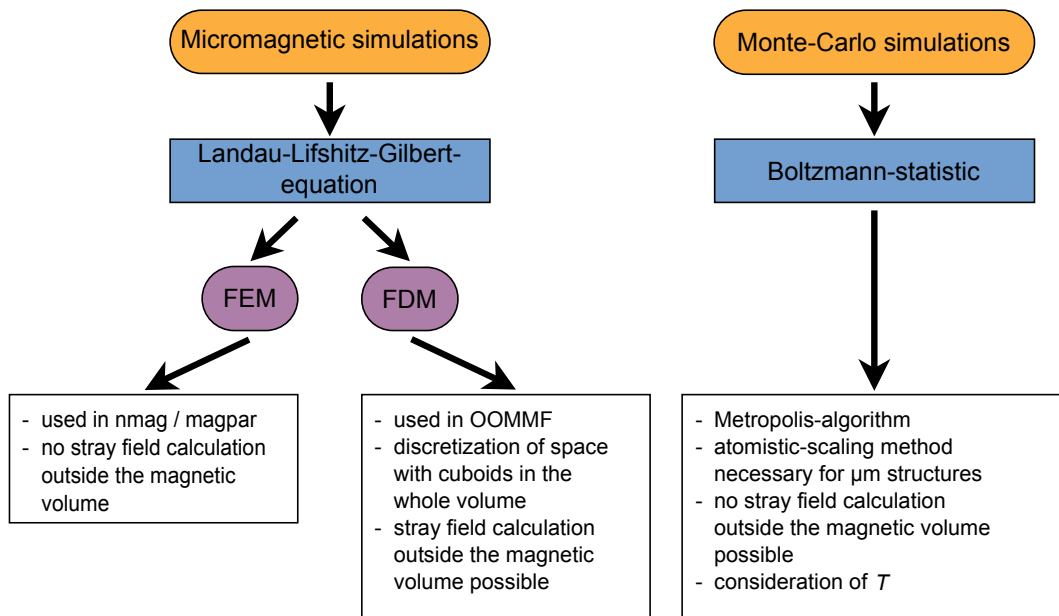


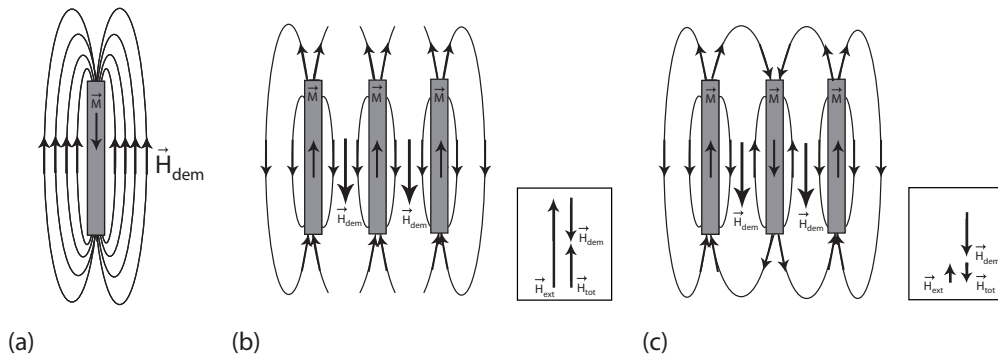
**Figure 2.12.:** In the scheme theoretical methods used for nanostructures are contrasted. Results of calculations made by FDM-method were used in this thesis, stray field calculations can be considered.

In figure 2.12 both theoretical methods are compared. As mentioned, the FDM method is the best method to calculate the reversal modes for the here treated nanostructures.

## 2.4. Magnetic configuration and reversal in nanowires and nanotubes

After introducing nanostructures such as unstructured and structured films e.g. circular plane and submicron nanostructures (2-dimensional) and the theoretical simulations, 3-dimensional nanostructures the topic of this work will be presented. First, nanowires are introduced, their magnetostatic configurations and reversal process. After this the magnetic reversal of nanotubes is shown.



**Nanowires**


**Figure 2.13.:** Different magnetization configurations of a single wire, illustrated in (a) and in (b) and (c) of an array of wires. In (a) the single wire is saturated along the wire axis. (b) Shows also the saturated state of the three wires, in (c) the middle wire has already been switched. The small insets give the reader information about the external field, demagnetization field and the total field for the illustrated states of the three wires.

The shape anisotropy is the reason ferromagnetic nanowires prefer to align their magnetization along the wire axis. Figure 2.13 (a) shows a single nanowire magnetized along the wire axis, figure 2.13 (b) and (c) illustrates the case for an array of three wires. This configuration in (a) can be explained by shape anisotropy or demagnetization energy minimization. The shape anisotropy is here of the uniaxial type[ELR+03]. In this configuration the demagnetization energy is minimized in opposite to an antiparallel alignment along the wire axis. The strayfields of three magnetic wires are shown in figure 2.13 (b) and (c). Figure 2.13 (b) consists of an array of three wires in an applied magnetic field. The magnetic moments of the wires are all aligned in the same direction, the magnetization is saturated. The inset shows vector addition of the different fields, in case (b) the external field is twice as large as the demagnetization field and the total field. Here, all fields are still positive. In figure (c) the magnetic moments of the outside wires are still in the same direction, the middle wire has already switched. Because of the stray field interaction between the neighbors, single nanowires are switching in the opposite direction. By this influence, the switching field is not only smaller in total, single nanowires are also already switching at this time. A hysteresis of wire array consists of single hysteresis loops, that's why the switching is occurring in a bigger range than in a single nanowire measurement(see figure 2.8). In single wire hysteresis loop a switching would not taken place at positive fields. This dipole-dipole interaction between the wires has to be taken into account also in theoretical calculations, so the calculated values have to be decreased. This will be also further discussed later in chapter 5. Wires are suitable to compare theory and experiment because of the simple possible models to describe the effect of critical parameters. The reversal process

in cylinders was analyzed for a long time[MDA09, ABDH97, JGK+00]. The reversal process of wires depends on the geometry. The parameters length and radius are the significant values[EAJ+07]. These parameters define the reversal mechanism in the wire. Three different reversal processes are possible in nanowires-

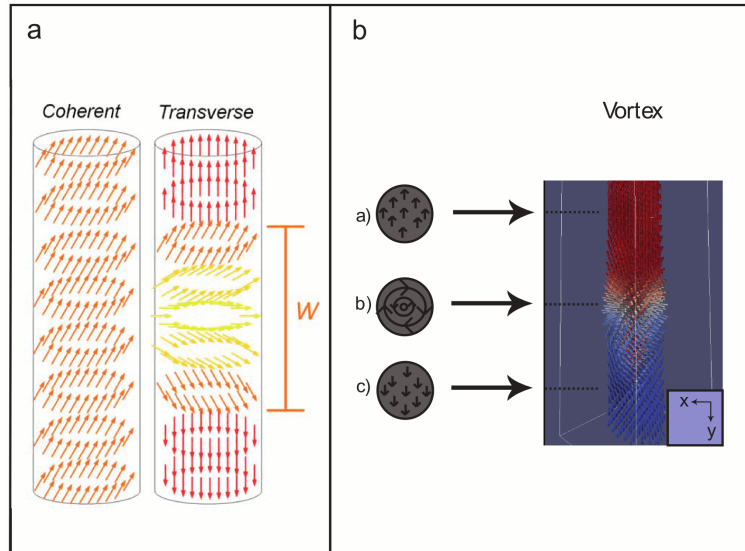


**Figure 2.14.:** Magnetization reversal modes in nanowires by coherent rotation mode and transverse reversal mode in part a of the figure[LDE+09]. The right part b shows a numerical simulation by OOMMF of a wire with schemes of the different reversal states during a vortex reversal process[Esc10].

the coherent rotation (i: the C Mode), the transverse mode (ii: the T Mode) and the vortex wall reversal (iii: the V Mode). (i) The coherent rotation which is illustrated in figure 2.14 a is a reversal process where all spins (local moments) rotate at the same time. The rotation is described by the Stoner-Wohlfahrt-model [SW48]. This model was originally used for single domain reversals which are realized in particles. At a certain size a domain wall is built in particles below this size there is the single domain state which can also be found in small volumina. There the coherent reversal can be found. For the wires used in this thesis the coherent rotation does not occur. The structures are too big, so that this is not the favorable reversal. The coercive field can be calculated analytically with the following equation [SW48]:

$$\frac{H_c^C}{M_0} = -\frac{2K_a}{\mu_0 M_0^2} + \frac{2K(l)}{\mu_0 M_0^2} \quad (2.13)$$

Here,  $K_a$  is the anisotropy constant,  $K(l) = \frac{1}{4} \mu_0 M_0^2 (1 - 3N_z(l))$  the shape anisotropy and  $N_z(l)$  corresponds to the demagnetization factor along  $z$  [EBJ+08]. (ii) Transverse and the (iii) vortex mechanisms are possible. The transverse mode the wires are not switching simultaneously. During a transverse reversal a transverse domain wall is nucleated, this is illustrated in figure 2.14 a. For the T mode, the coercive field has been approximated by an adapted Stoner-Wohlfarth model, [EBJ+08, SW48] in which the length  $l$  of the coherent rotation is replaced by the width of the domain boundary,  $w_T$  [LAE+07].

$$\frac{H_c^T}{M_0} = \frac{2K_a}{\mu_0 M_0^2} + \frac{2K(w_T)}{\mu_0 M_0^2} \quad (2.14)$$

(iii) Lastly, there is the vortex domain wall reversal. The spins rotate by progressive stages via a nucleation of a vortex wall. Figure 2.14 b shows a simulation picture of a wire which includes one domain wall. This simulation was done by OOMMF from Escrig and co-workers [Esc10]. Here, the use of the FDM method (which was discussed in the section, simulations) can be seen. This figure shows one part of a simulation, more can be found in the appendix in figure B.4, B.5, B.6, B.7 and 5.3 in which more complex structures are simulated. In such a wire not only one domain wall can be nucleated, this can be dependent on the not exact alignment of the samples in the applied magnetic field. But, in the simplest case which is shown here, one domain wall is nucleated. The magnetization changes its direction parallel to the wire axis. In between there is a vortex domain wall. The vortex mechanism was already introduced in section 2.6. In cylindrical confined 2D-nanostructures the vortex mode is introduced the first time, here the nanostructure is elongated and it is a 3D-nanowire, but their reversal mechanism have similarities and can be compared. Following the approach equation 2.15 for the V reversal mode the exchange length and outer radius is now considered [CLY94a]. The magnetization is assumed to reverse completely at the nucleation field which is illustrated for single wires in figure 2.8

$$\frac{H_c^V}{M_0} = \frac{2K_a}{\mu_0 M_0^2} + \frac{112 l_{ex}^2}{33 R^2}, \quad (2.15)$$

with the exchange length  $l_{\text{ex}} = \sqrt{2A/\mu_0 M_0^2}$ [STRS63]. The exchange length for nickel is here  $l_{\text{ex}} = 8.226 \times 10^{-9}$  m[O'H00]. The quotient  $\frac{112}{33}$  or rather  $1.08\pi$  is described in the reference[STRS63]. From equation 2.13 one can clearly see that the vortex mode is dependent on the exchange length  $l_{\text{ex}}$  and the radius.

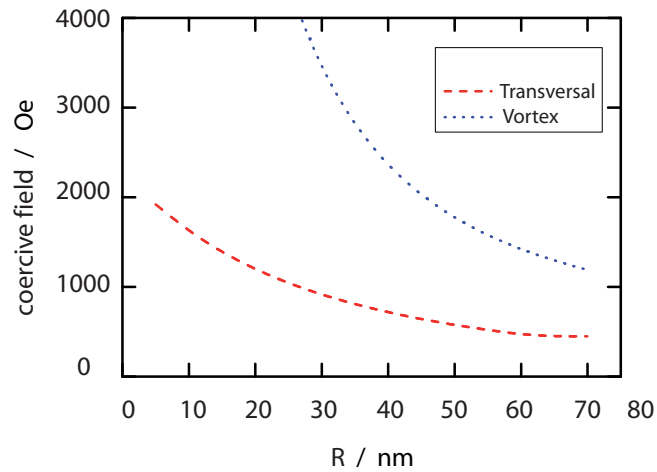


**Figure 2.15.:** The figure illustrates the coercive field calculated with equations 2.14 and 2.15 dependent on the radius for an isolated nickel wire with a fixed length of  $10 \mu\text{m}$ .

The figure 2.15 illustrates the calculated coercive fields dependent on the radii. Here, the length is fixed. For the calculations the radius  $R$  of an isolated wire is varying from 15 to 80 nm. The length is fixed to 10  $\mu\text{m}$  and  $M_0 = 4.85 \times 10^5 \text{ A/m}$ ,  $A = 10^{-11} \text{ J/m}$  and  $K = -11 \times 10^3 \text{ J/m}^3$  [O'H00]. Escrig and co-workers showed that the system will reverse its magnetization by whichever mode opens an energetically accessible route first, that is, by the mode that offers the lowest coercivity [EBJ+08]. Details and comparisons to the experimental data are presented in chapter 5. On the one hand, geometrical parameters have a mutual influence on the coercivity. So, at first the coercivity in the array is dependent on its length and radius [EAJ+07], but also on the other hand, the wires in the array are influencing themselves. Furthermore the magnetostatic interactions in the nanowire array are important for the reversal process. The template is perfectly ordered (see chapter 3.1.2), so that the environment of each wire in the ensemble is the same. The wires in the ensemble are comparable and differences in geometry (radius) can be analyzed. Also, the filling of the pores is mostly the same, so that the lengths are comparable.

To conclude, there are on the one hand material parameters such as the saturation magnetization  $M_{\text{sat}}$  and the exchange length  $l_{\text{ex}}$  which influence the magnetic properties of the wires. On the other hand the contribution of the shape anisotropy, geometrical parameters e.g. the radius. More details will be given in chapter 5.

### Nanotubes

In general the same reversal modes are possible for tubes as well as for wires: the coherent rotation (i: the C Mode), the transverse mode (ii: the T Mode) and the vortex wall reversal (iii: the V Mode) [BZC+08]. Which mode actually occurs depends not only on the previously mentioned parameters, here is one additional parameter: the wall thickness  $w_{\text{T}}$ .

The vortex and transverse reversals are illustrated in figure 2.16, the spins switch from one end of the tube and to the other end by nucleating a domain wall. In the middle of the particular tube the vortex and transverse domain wall regime is shown.

The magnetic switching of the ferromagnetic nanotubes is investigated as a function of their geometry [AAN09]. A change in the geometry e.g. radius and length will lead to different physical results. The shape of the tubes also allows to make easy models and approximate analytical equations. (i) The coherent rotation was only present in very short tubes, when  $l \approx \omega_{\tau}$  or less [LAE+07]. Here, the coercive field is obtained from the Stoner-Wohlfarth model [SW48]:

$$\frac{H_c^C}{M_0} = \frac{2(K(l) - K_a)}{\mu_0 M_0^2}, \quad (2.16)$$

where  $K_a$  is the anisotropy constant,  $K(l) = \frac{1}{4} \mu_0 M_0^2 (1 - 3N_z(l))$  and  $N_z(l)$  corresponds to the demagnetization factor along  $z$  [EBJ+08].

Here, one is mainly interested in long tubes, so that the focus will lie on the transverse and vortex wall reversal [LAE+07, EBJ+08].

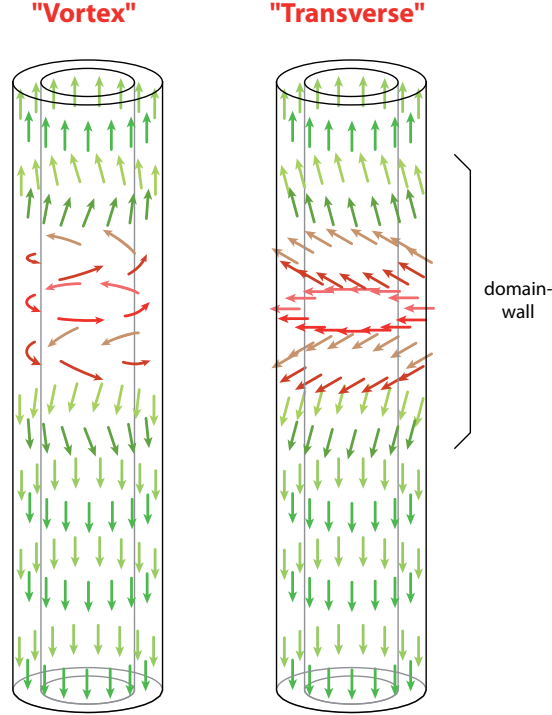


**Figure 2.16.:** Scheme of different magnetization reversal modes in magnetic nanotubes. The orientations of the local magnetic moments are assigned by arrows.(left) vortex wall (right) transverse wall with wall thickness  $w_V$  or  $w_T$ .

(ii) For the T mode, the coercive field has been approximated by an adapted Stoner-Wohlfarth model,[EBJ<sup>+</sup>08, SW48] in which the length of the coherent rotation is replaced by the width of the domain boundary (like for solid wires),  $w_T$ [LAE<sup>+</sup>07]:

$$\frac{H_c^T}{M_0} = \frac{2K(w_T) - K_a}{\mu_0 M_0^2}. \quad (2.17)$$

Finally, for the V reversal mode(iii) the nucleation field of an infinite nanotube[CLY94b] has been considered. Thus, the magnetization is assumed to reverse completely at the nucleation field:

$$\frac{H_c^V}{M_0} = \frac{2K_a}{\mu_0 M_0^2} + \alpha(\beta) \frac{l_{ex}^2}{R^2}, \quad (2.18)$$

with the exchange length  $l_{ex} = \sqrt{2A/\mu_0 M_0^2}$ .  $\alpha(\beta) = q^2$ [EBJ<sup>+</sup>08] where  $q$  satisfies the condition:

$$\frac{q J_0(q) - J_1(q)}{q Y_0(q) - Y_1(q)} = \frac{\beta q J_0(\beta q) - J_1(\beta q)}{\beta q Y_0(\beta q) - Y_1(\beta q)} \quad (2.19)$$

Here,  $J_p(z)$  and  $Y_p(z)$  are Bessel functions of the first and second kinds, respectively. Equation 2.19 has an infinite number of solutions, and the physically

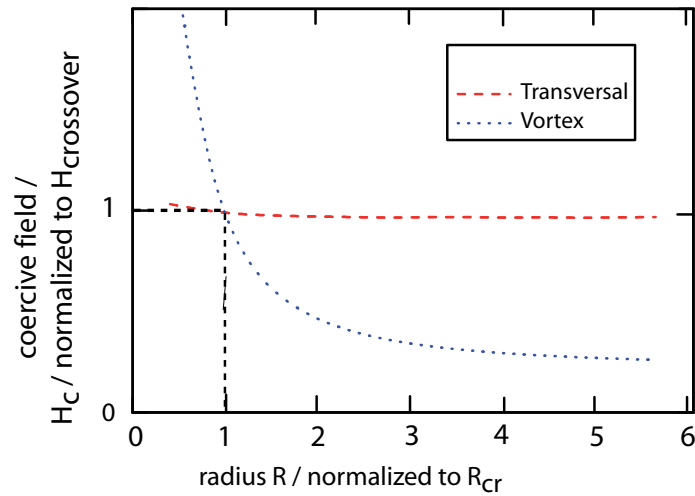


**Figure 2.17.:** The figure illustrates the normalized coercive field dependent on the normalized radius. The parameters are normalized to a crossover radius at a specific coercive field. There is a crossing of the dashed red and pointed blue curves at  $R_{cr} = 22$  nm approximately, corresponding to a magnetization reversal for which both T and V mechanisms are possible at the same coercive field.

correct solution is the smallest one[EBJ+08]. Figure 2.17 illustrates the coercive fields of an isolated tube with varying radius. There is a crossing of the red dashed and blue pointed curves at  $R_{cr} = 22$  nm approximately, corresponding to a magnetization reversal for which both T and V mechanisms are possible at the same coercive field. The vortex curve converges asymptotically to a constant value, this behavior is described by the added  $\frac{1}{R^2}$  of the equation 2.18. The values for the transverse reversal are all nearly constant.

In this range the coercive fields for the T mode are nearly independent of the radius.

For long tubes the transverse and vortex switching is dependent on the internal and external radius of the tube. If the tubes have a small wall thickness, the vortex mode will be the most occurred one.

If the wall is thicker, then mostly the transverse wall occurs.

Also, the magnetostatic interactions of the tubes in the array are responsible for a decrease in the coercive field[EBJ+08].

## 2.5. Superparamagnetism

For the reversal analysis of the prepared nanotubes it is an assumption that the tubes consist of homogeneous magnetic volumina and do not have magnetic granular structures. With the present experimental methods, the superparamagnetism can be measured. This is characteristic for small ferromagnetic particles where the ferromagnetic particles are within aligned

ferromagnetically. The alignment to each other is arbitrarily like a paramagnetic material. Ferromagnetic particles show a paramagnetic behavior to each other at high temperatures. At low temperatures coercive fields can be measured. They are ferromagnetic and interacting with each other. There is a long-range ferromagnetic alignment. To check if the synthesis was successful, the results from these measurement act as sufficient indicator for this kind of magnetic behavior. The superparamagnetism[BK09] is identified by the blocking temperature  $T_B$ . The figure 2.18 illustrates the magnetic moments of particles below and above the blocking temperature  $T_B$ . In part a of the figure 2.18 particles with their spins are

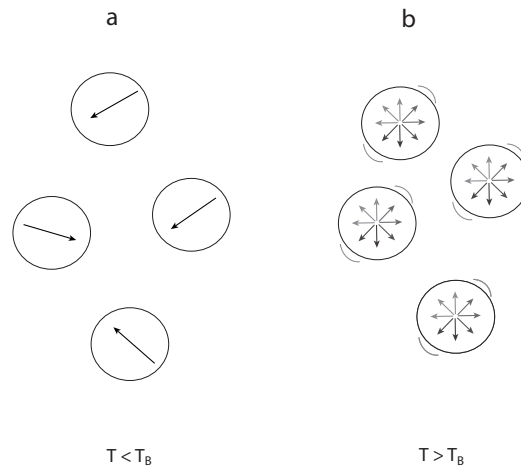


**Figure 2.18.:** In the scheme superparamagnetic particles with their magnetic moments are shown. In part a the spins are frozen below the blocking temperature  $T_B$ . They are unordered without an applied field. In part b the regime above  $T_B$  is shown. The spins can rotate freely. The figure is equal to[PCJD03]

shown below the  $T_B$ . It is a so-called blocked state, the spins are frozen. Here, the spins are unordered when they are frozen in zero field. In part B of the figure 2.18 the thermal fluctuation is high enough that the spins can rotate freely. The energy barrier is the barrier which constitutes the energy regimes in which the particles on the one hand are in the blocked state or on the other hand can rotate freely. It is due to various reasons e.g. magnetocrystalline anisotropy.

The energy is defined as:

$$E = KV\sin^2\theta \quad (2.20)$$

The energy barrier for a particle can be described by:

$$\Delta E = KV \quad (2.21)$$

The two energy minima at  $\theta = 0$  and  $\theta = \pi$  correspond to the magnetization parallel or antiparallel to the easy axis shown in figure 2.19[BK09]. If the  $k_b T \gg KV$  the particles can be considered as freely rotating ( $k_b$  is the



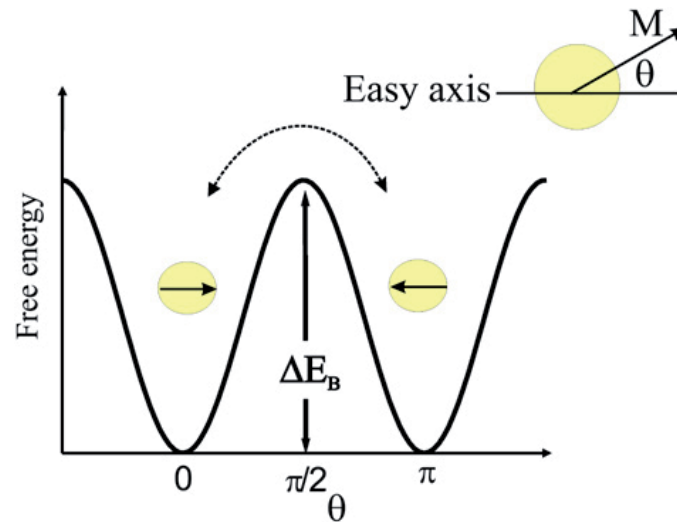


**Figure 2.19.:** Schematic picture of the free energy of a single-domain particle with uniaxial anisotropy as a function of magnetization direction. EB is the energy barrier hindering the free rotation of the magnetization and  $\theta$  is the angle between the magnetization  $M$  and the easy axis[BK09].

Boltzmann's constant). If  $KV$  is in the range of the thermal energy, there is a crossover into superparamagnetism. At last if  $k_bT \ll KV$  the particles are blocked. The diameter of the particles plays a big role for the energy barrier. If the particles are bigger, the energy barrier becomes higher, so that the blocking temperature is shifted to higher temperatures. Thus, the blocking temperature is dependent on the grain size and can so be shifted to lower or higher temperatures[BK09].

More details can be found in chapter 4.2.1.

## 3. Preparation

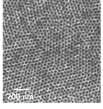
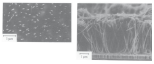
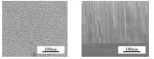
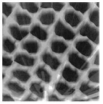
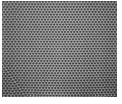
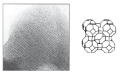
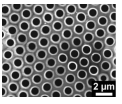
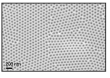
In this thesis material and geometry of nanowires and nanotubes are analyzed. The magnetic configuration and magnetization changes in these structures help to find out which type of structure is the most interesting for the analyzing of the pinning and depinning of domain walls as well as which material is suitable for later technological use. The samples are made out of porous anodic alumina membranes and are used as template filled with magnetic material. To achieve the two different structures mentioned above, the deposition technique, the electrochemical deposition method (electrodeposition: ED) is used in growing the nanowires and atomic layer deposition (ALD) for the nanotubes.

### 3.1. Template

In general, there are several methods to prepare nanowires and nanotubes. There are preparation techniques which include templates or not e.g. 'bottom-up' approaches[CGGH05], top-down and lithography or self-assembly approaches such as via step-edge decoration[PHJ98], aqueous growth using electrical fields and vapor-liquid-solid-technique[ML98]. For the fabrication of the wires and tubes analyzed in this thesis only nanoporous template preparation was considered. The following table introduces some prominent templates 3.1. On the one hand, templates can be made out of diblock copolymers[XKD+01] which is shown in the table 3.1 as a first example. A scanning microscope picture (SEM) of a self-organized, close-packed hexagonal array is shown with a pore diameter  $\approx 40$  nm. On the other hand, the phase-separated Al-Si alloy from which the Al has been etched[FTMD04] can also functionalize as a template. This is also illustrated in the table 3.1 in which a SEM picture is shown, left the top and right the section is shown. In general, one puts two major types of templates in contrast with each other: the 'track-etch' polymeric membranes and the porous membranes. The 'track-etch' polymeric membranes are sold commercially, different pore sizes are available (e.g. 30 , 60 and 100 nm), these membranes are prepared from polycarbonate and polyester[Mar94]. The second position in the table shows a track-etch membrane which is disordered. This is also illustrated in table 3.1. An array of 60-nm diameter nickel nanowires embedded in the polycarbonate matrix shown left in a top SEM picture and right in cross-section[WJSC93]. Porous membranes can be prepared by different processes, membranes made of nanoporous solid for example which is shown in the table 3.1. A typical example of nanoporous solid[THGRB09] is shown in position 4. The average diameters are  $\approx 3$  nm. The table introduces also nanochannel array glass as a template, shown in a small illustration. 450-nm-diameter hollow channels arranged in a hexagonal close

packing array configuration contained within the matrix glass are illustrated in a SEM micrograph. It is shown in 26  $\mu\text{m}$  in width section [TJCF92]. Zeolite can also be used as a template, which is shown on the one hand schematically [DL92] and on the other hand, in a transmission electron microscope (TEM) picture [BVR<sup>+</sup>92]. The pore opening is  $\approx 1$  nm. Another ordered template which is also displayed in a SEM micrograph: macroporous Si containing Er : LiNbO<sub>3</sub> microtubes. In the end, the anodic alumina membranes (AAM) [MM11] are given, illustrated in a top SEM micrograph. The membrane is self-organized in a close-packed hexagonal array with a pore diameter  $\approx 40$  nm and at last a perfectly-ordered AAM template [MM12]. The preparation of anodic alumina templates [MTB90, MF95] is a good technique for creating templates for wires and tubes which was used here. The high temperature resistance is also very important to survive the later following deposition and reducing process (temperatures  $\approx 300^\circ\text{C}$ ). With AAMs, it is possible to have a perfect order and strictly parallel configuration with the substrate in order to obtain high aspect ratios (10-100). There is also a high density of pores and a wide arrangement of pore diameters.

**Table 3.1.:** The table shows some examples of membrane templates.

Figures	Template	Details	References
	<b>Diblock copolymers</b>	<ul style="list-style-type: none"> <li>– self-organized</li> <li>– close-packed hexagonal array</li> <li>– diameters <math>\approx 20 - 100</math> nm</li> <li>– heat resistant</li> </ul>	<a href="#">[BGM<sup>+</sup>01]</a> <a href="#">[XKD<sup>+</sup>01]</a>
	<b>Track-etch membranes</b>	<ul style="list-style-type: none"> <li>– disordered</li> <li>– diameters <math>\approx 10</math> nm - <math>1 \mu\text{m}</math></li> <li>– <math>10^9</math> pores <math>\text{cm}^2</math></li> </ul>	<a href="#">[FBPW75]</a> <a href="#">[WJSC93]</a> <a href="#">[KNS02]</a>
	<b>Etched silicide</b>	<ul style="list-style-type: none"> <li>– nanoporous films</li> <li>– diameters <math>\approx 5 - 13</math> nm</li> <li>– <math>10^{16}</math> pores/<math>\text{cm}^2</math></li> </ul>	<a href="#">[FTMD04]</a>
	<b>Misoporous solids</b>	<ul style="list-style-type: none"> <li>– closed-packed hexagonal array</li> <li>– mesoporous</li> <li>– average diameters <math>\approx 3</math> nm</li> </ul>	<a href="#">[Ozi92]</a>
	<b>Glass-nano channel arrays</b>	<ul style="list-style-type: none"> <li>– highly-ordered</li> <li>– closed-packed hexagonal array</li> <li>– diameters <math>\approx 450</math> nm</li> <li>– <math>3 \times 10^{10}</math> pores/<math>\text{cm}^2</math></li> <li>– heat resistant</li> </ul>	<a href="#">[TJCF92]</a>
	<b>Zeolites</b>	<ul style="list-style-type: none"> <li>– randomly distributed</li> <li>– large areas closed-packed hexagonal array</li> <li>– pore opening <math>\approx 1</math> nm</li> </ul>	<a href="#">[DL92]</a> <a href="#">[BVR<sup>+</sup>92]</a>
	<b>Macroporous silica</b>	<ul style="list-style-type: none"> <li>– ordered</li> <li>– closed-packed hexagonal array</li> <li>– diameters <math>\approx 500</math> nm - <math>10 \mu\text{m}</math></li> <li>– heat resistant</li> </ul>	<a href="#">[ZLZ<sup>+</sup>06]</a>
	<b>Anodic alumina membranes</b>	<ul style="list-style-type: none"> <li>– self-organized/perfectly ordered</li> <li>– closed-packed hexagonal array</li> <li>– diameters <math>\approx 10 - 450</math> nm</li> <li>– <math>\approx 10^{11}</math> pores/<math>\text{cm}^2</math></li> <li>– heat resistant</li> </ul>	<a href="#">[DP89]</a> <a href="#">[MTB90]</a> <a href="#">[MM11]</a>

Anodic Alumina Membranes are synthesized by electrochemical oxidation. The surface of aluminum consists naturally of a compact oxide film, which is homogeneously and a few nm thick. The oxide layer due to the formation of pores can be elongated by anodization, allowing to keep the compact oxide layer thickness constant. The major part of the potential drop is across the oxide layer. The ions can drift through the oxide because of the high electrical field (9 MV/cm[Cso64]) in the oxide layer and this implements the electrochemical oxidation of the aluminum:

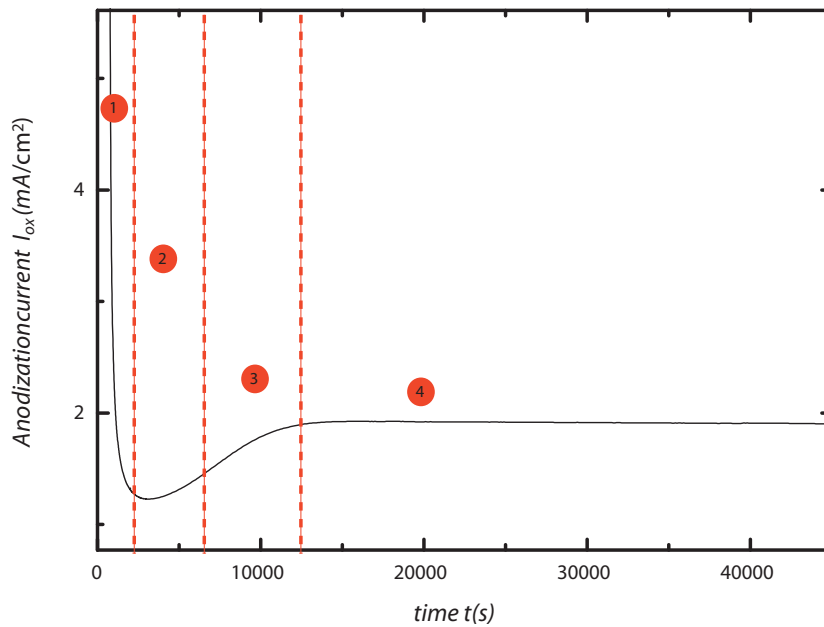
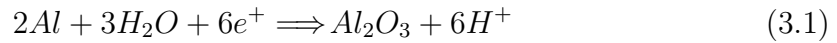


**Figure 3.1.:** Transient curve of the anodization in phosphoric acid. The different regimes (1-4) during the pore growth are also defined in the graph.

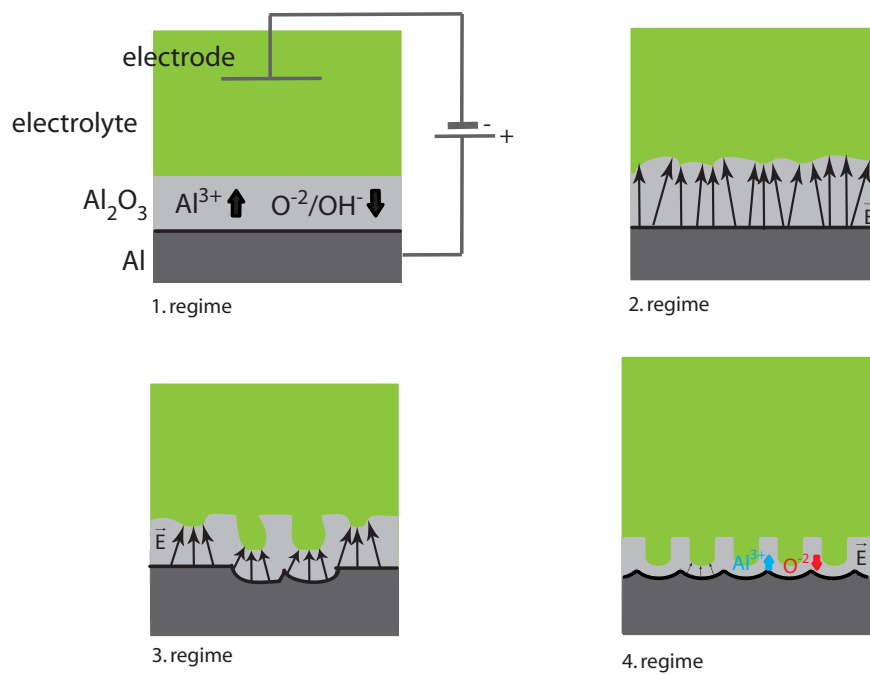


**Figure 3.2.:** The different regimes (1-4) during the pore growth are illustrated. Equal to [PS92]

Al is oxidized into  $\text{Al}^{3+}$ . A splitting of water molecules is happening at the interface oxide/ electrolyte. The resulting  $\text{O}^{-2}$  and  $\text{OH}^{-}$ -ions react directly with the  $\text{Al}^{3+}$  ions or drift through the oxide layer to the metal because of the field reaction. For the realization of the porous  $\text{Al}_2\text{O}_3$  three main electrolytes are used: (1) sulphuric acid ( $\text{H}_2\text{SO}_4$ ), (2) oxalic acid  $\text{H}_2\text{C}_2\text{O}_4$  and (3) phosphoric acid  $\text{H}_3\text{PO}_4$ . Figure 3.1 represents the current profile for the pore growth in phosphoric acid. There are various regimes which describe the kinetics of the pore growth which is also illustrated in figure 3.2. It starts with the building of a homogeneous planar barrier oxide (1) until the oxide formation equals oxide dissolution. The current exponentially decreases. In regime (2) figure 3.1 and figure 3.2 the current is rising. Inherent roughness of the surface let the electric field lines focus and the field increased dissolution of the oxide is the occurrence. Thinner points in the barrier layer are built and serve as nucleation points. The focusing of the streamlines of the field amplifies the ion drifting through the barrier oxide in the thinner points, a higher oxide growth at the nucleation points is initiated and the current further increases and saturates when the surface is homogeneously covered with pores (3) in figures 3.1 and 3.2. Thus, the pore growth begins randomly at the  $\text{Al}_2\text{O}_3$  surface. With a growing pore density the current  $I_{\text{Ox}}$  rises until the surface is completely covered with pores. The mechanical interactions between the pores causes them to adjust their interdistance to each other until a stable structure is obtained. The  $I_{\text{Ox}}$  increases more slowly (end of (3) figure 3.1, figure 3.2) and then slightly sinks (4) in figure 3.1 and figure 3.2 until there is a stable interpore distance  $D_{\text{INT}}$ . This process takes several minutes to hours and differs in respect to acid electrolytes used. The anodization of the aluminum is realized in an electrochemical cell[Jes97]. This cell consists of a PVC<sup>1</sup> cup held tightly to a copper plate at the bottom with the aid of screws. The aluminum chip is contacted by the copper plate. PVC is used as a non-conducting jar. Another Teflon part aligned with a platinum wire is inserted into the open top of the PVC cup. The copper plate and the platinum wire are applied as electrodes. The acid solution is continuously stirred and also cooled by cooling plates which are put on a refrigerated water cycle. The whole anodization cell is insulated by polystyrene to reach important constant  $T$  or to reach lower  $T$  in the chillers. During the anodization the aluminum chip serves as the anode and the platinum wire is the cathode. Figure 3.1 part (1) describes a schematical draw of the anodization cell and its parameters[Nie02].

---

<sup>1</sup>PVC

### 3.1.1. Self-ordered anodic alumina membranes

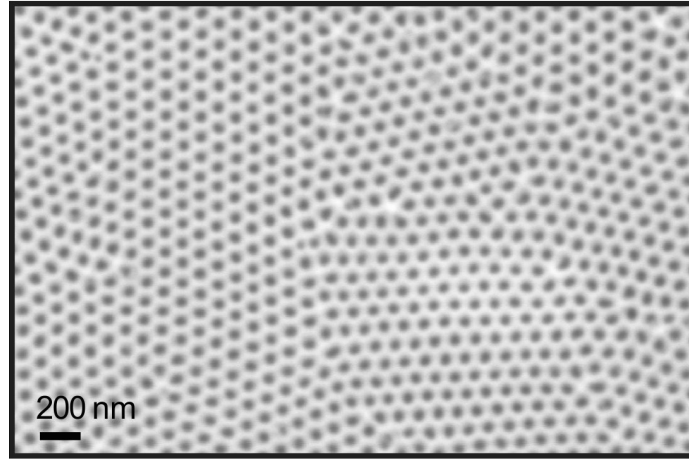


**Figure 3.3.:** The figure shows an example of self-ordered anodic alumina membrane, anodized in oxalic acid viewed from the top[MM11].

Anodic aluminum membranes prepared by electrochemical oxidation of aluminum have been investigated for more than 100 years[KHR53, HF54, TW81, Loh93, DDG69, WO70] and were used as protective layers. 1995 Masuda and Fukuda[MF95] have developed two-step anodization under self-ordered regime of alumina

membranes[LMT<sup>+</sup>02]. The two step anodization process realizes the use of the AAMs as templates. The self-ordered regimes have continuous pores in a hexagonal polydomain arrangement with pore diameter  $D_p$  which is associated a low polydispersity (about 10 %).

In general the fabrication of self-ordered ( $\text{Al}_2\text{O}_3$ ) pore arrays is realized with the so-called 'mild anodization'(MA) conditions.

The typical MA process parameters for the three well-known growth regimes are:

(1) sulphuric acid ( $\text{H}_2\text{SO}_4$ ) at 25 V for an interpore distance

$D_{\text{int}} = 63 \text{ nm}$ [MHO97, LMB<sup>+</sup>98], (2) oxalic acid  $\text{H}_2\text{C}_2\text{O}_4$  at 40 V for

$D_{\text{int}} = 100 \text{ nm}$ [MF95, LMB<sup>+</sup>98, MYO98](see figure 3.3), and (3) phosphoric acid  $\text{H}_3\text{PO}_4$  at 195 V for

$D_{\text{int}} = 500 \text{ nm}$ [MYO98, NWB<sup>+</sup>02]. The correlation of the pore distance and potential is 2.5 nm/ V. The porosity is in all cases 10 %. The MA takes some days for optimum results and the template is ordered but in a order polydomain configuration. The slow fabrication is one of the practical limitations. The so-called 'hard anodization' (HA) by Woo Lee renewed the interest in the field[LJGN06]. In fact, the HA was first introduced in the early 1960s[CH61, CS62, LBD60, Cso64]. Albeit without any order. The HA is done in sulphuric acid relatively at low temperatures and high current densities and has been realized in various industrial applications, such as automobile engineering, surface furnishing of aluminum cookware, textile machinery and so on, by the



high-speed oxide growth ( $50\text{-}100\mu\text{ m h}^{-1}$ )[Olb88, RPS+05, JBS84, Hec88]. The HA anodization was not sought-after in the academic research because of the difficulties in controlling the pore size, interpore distance and aspect ratio of the nanopores of the template. Scientists have tried different other approaches like working with acid mixtures[SMST04, OSIA04, OSA04] or high potentials and current densities[CWI+05, CH61, CS62, Cso64, ACM86, WSYB86].

In this thesis stabilization of HA conditions is achieved by growing an initial thin oxide layer under suitable MA conditions and then switching to HA conditions according to Lee's process[LJGN06]. The next step was the combination of a pre-patterning of the aluminum surface with lithography method and a subsequent MA[MJTD01, MAW+01, FBKR+04, ANN+01, LJR+06]. This has the advantage in fabricating highly perfectly ordered membranes in comparison to self-ordered membranes. This provides the opportunity to make perfectly ordered membranes in contrast to the self-ordered membranes.

The high electric field at voids enables a nucleation at pits caused by the pre-patterning. Woo Lee has investigated a method to utilize AAMs with different pore diameter through a combination of HA and MA after a prestructuring of the surface by nanoimprinting[LJGN06, LSS+08].

### 3.1.2. Perfectly ordered anodic alumina membranes

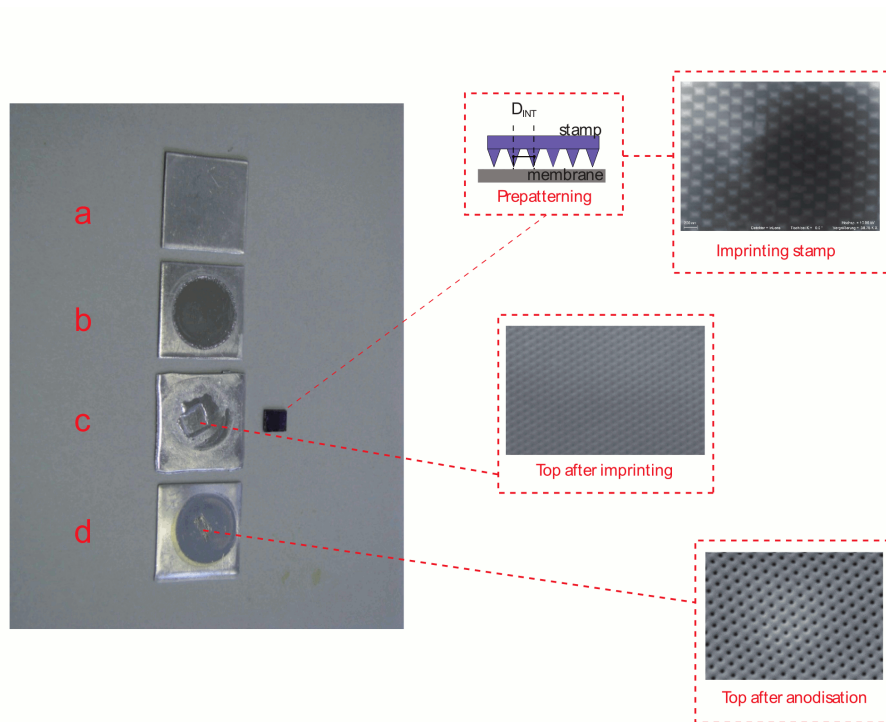


**Figure 3.4.:** The fabrication of perfectly ordered anodic alumina membranes is shown. In (a) the alumina chip and in (b) the electropolished chip is illustrated. In (c) the imprinted chip and in (d) the anodized sample is shown. The insets on the right show pictures of the nanoimprinting and a picture of the stamps surface and the last two insets illustrate sample surface: the top side after nanoimprinting and the top side after anodization

In this thesis the method of nanoimprinting is adapted and optimized for the conditions used here [LJGN06, LSS<sup>+</sup>08]. Nanoimprinting of aluminum is the first step of the procedure. This pretexturing defines the subsequent nucleation points of the pores during the first anodization. A nanoimprinting stamp consisting of hexagonally arranged SiN pyramids with a period of 235 nm was used (see figure 3.4 inset of the stamp's surface). An electropolished aluminum chip (see figure 3.4 (b)) was stamped with it under  $\approx 9$  tons/mm<sup>2</sup> (see figure 3.4 part (c)). For the subsequent anodization, the applied voltages  $U$  were adapted to match the period  $D_{\text{INT}} = 235$  nm [LJGN06, LSS<sup>+</sup>08]. The optimal voltages which were worked out through experiment are  $U_{\text{mild}} = 72$  V in phosphoric acid (0.40 M) and  $U_{\text{hard}} = 93$  V in oxalic acid (0.15 M) for the mild and hard conditions, respectively (see figure 3.4 part (d)). The former value deviates from the commonly accepted slope of the  $D_{\text{INT}}$  vs.  $U_{\text{mild}}$  curve (2.5 nm/V) for self-ordered regime. This deviation is attributed to the comparatively very low voltage used here (72 V) — far from the self-ordered range of mild phosphoric acid anodization (160 to 196 V). However, for short anodizing times, ordered is retained (to thickness of  $< 1 \mu\text{m}$ ). Conversely, hard anodization is carried out at a drastically higher voltage (93 V) than usually done for the mild anodization in oxalic acid (40 V). In this case, stabilization of the unusually high electric field is achieved by combining two approaches: 1) formation of a thin oxide layer by a preliminary mild anodization and 2) use of a water/ ethanol mixture for hard anodization at  $-5^\circ\text{C}$ . This allows for the lithographically defined 235-nm order to be maintained throughout the anodization. HA is then used to thicken the layer while ordering is kept.

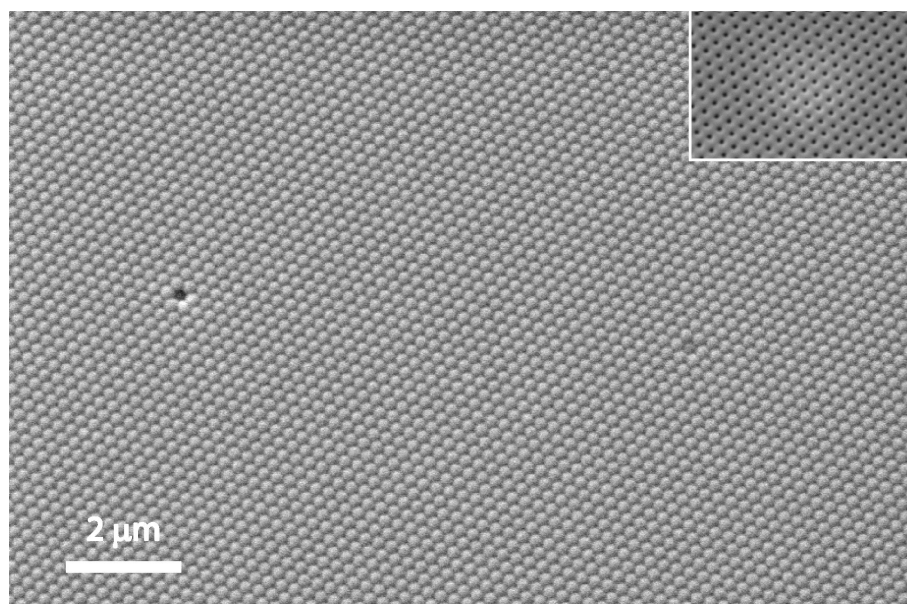


**Figure 3.5.:** Scanning electron micrographs of a nanoimprinted and anodized membrane of approximately  $20\ \mu\text{m}$  thickness. The main panel shows the bottom side of it, to be compared with the top (imprinted) side, in the inset. The prestructuring is maintained throughout the anodization.

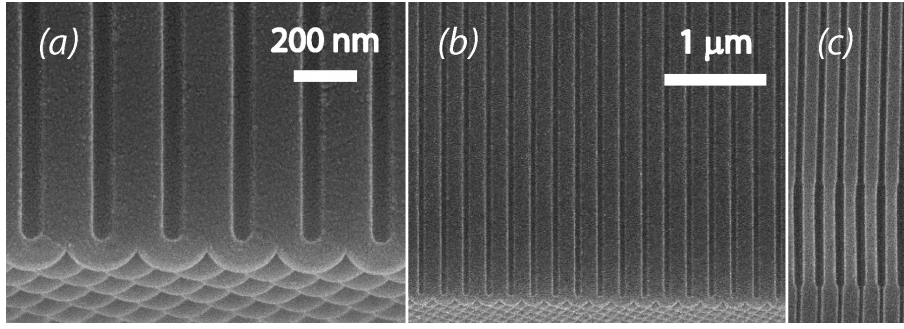


**Figure 3.6.:** Scanning electron micrographs of the porous anodic alumina template. The membrane is displayed in cross sections, pores are broken in halves along their  $z$  axis. (a) End of the pores with hemispherical barrier layer. (b) The last  $4 \mu\text{m}$  of a perfectly ordered 'hard' segment: the pore diameter is absolutely constant and homogeneous. (c) A section of membrane displaying two changes in diameter, from 'hard' anodization (narrow pores) to 'mild' (thicker pores) and back to 'hard': the interfaces between the different segments are sharply defined. The scale bar is common for (b) and (c).

Figure 3.5 compares the top and bottom sides of a  $20\text{-}\mu\text{m}$  thick porous alumina membrane prepared under those conditions: the pores of  $70 \text{ nm}$  diameter and aspect ratio 300 have addicted their large-scale perfectly periodic arrangement. Mild and hard anodizations yield different porosities (approximately 20 % and 6 %, respectively). The porosity is calculated with:

$$p = \frac{\pi}{2\sqrt{3}} \left( \frac{d_p}{D_{\text{INT}}} \right)^2 \cdot 100 \quad (3.2)$$

$d_p$  is the pore diameter. Accordingly, they deliver distinct values of the pore diameter, namely,  $150 \text{ nm}$  and  $70 \text{ nm}$ . Therefore, several switches between the mild and hard conditions over the course of the anodization result in as many diameter modulations of the pores, as evident in Figure 3.6. The length  $L$  of each segment is controlled by the integrated current density  $Q$  passed through the system, with growth rates of  $\frac{L_{\text{mild}}}{Q} \approx 0.3 \frac{\mu\text{m}}{\text{C}/\text{cm}^2}$  and  $\frac{L_{\text{hard}}}{Q} \approx 0.6 \frac{\mu\text{m}}{\text{C}/\text{cm}^2}$  (for  $Q \leq 20 \frac{\text{C}}{\text{cm}^2}$ ).

## 3.2. Filling of the template

In this work, different materials and geometries are investigated. First electrodeposition of nickel (Ni) is presented, after this the ALD process is introduced. Processes for iron III oxide ( $\text{Fe}_3\text{O}_4$ ), nickel (Ni) and nickel/cobalt (NiCo) are shortly introduced. Nickel is a transition metal and ferromagnetic. The iron III oxide type magnetite  $\text{Fe}_3\text{O}_4$  is ferrimagnetic, as opposes to the non-magnetic  $\text{Fe}_2\text{O}_3$  hematite. Cobalt is also a transition metal and here nickel/cobalt is an alloy comprising nickel and cobalt.

### 3.2.1. Nanowires by electrodeposition

Metallic nanowires are made by electrodeposition [NWB<sup>+</sup>01]. For about 100 years the deposition of metals has been in the focus of interest by electrochemical processes [Fra07]. 1949 Blum and Hogaboom published some principles of material science [BH49] even though it was not so named at that time - electrodeposits and data on properties [Din93]. Industrial applications of electrochemical processes have come to the fore in the last past [Lan94] e.g. for surface treatment, but also in recent for the implementation of a novel data storage platform.

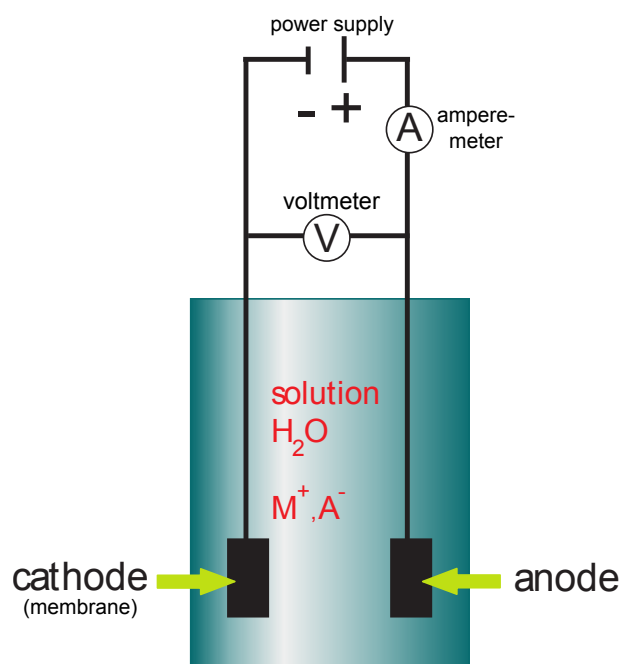


**Figure 3.7.:** A shematical illustration of the electrodeposition setup. A jar is filled with the electrolytic solution, the power supply and the cathode and anode (membrane) is shown.

The table 3.2 summarizes some of the important reviews of electrodeposition in the literature. The work is based on the large body of literature dealing with the electrodeposition of magnetic wires in porous templates such as anodic alumina (more details can be found section 3.2) [XYS<sup>+</sup>03, LGY04, YZL05, HCD<sup>+</sup>08, AG02, BTH<sup>+</sup>04, CSRC05, HCY<sup>+</sup>05, FP99, PLK<sup>+</sup>01, KBG<sup>+</sup>02]. For the conformal filling of the pores, two methods have been developed. In the first method an alternating current is used to deposit the material [NMLG00]. This was first realized by Caboni [Cab36]. In the second method a direct current is used for the deposition of the material [MYO98, Jes97]. In this work the electrodeposition was realized by a direct current deposition. This can be realized by a potentiostatic or galvanostatic deposition method where the potential of the electrode or on the other hand, the current density is kept constant. Here, the galvanostatic deposition was used. To prepare the template for electrodeposition, first the remaining aluminum is removed ( $CuCl_2 + HCl$ ) in order to get a free-standing membrane. Afterwards the so-called barrier layer of aluminum oxide closing the bottom of the pores is first

title	author	references
Electrochemical and materials science aspects of alloy deposition	D. Landolt	[Lan94]
Fundamental aspects and applications of electrochemical microfabrication	M. Datta D. Landolt	[DL00]
Recent developments in the electrodeposition of nickel and some nickel-based alloys	R. Oriňáková et al.	[OTK <sup>+</sup> 06]
A review of nanostructural aspects of metal electrodeposition	L. Peraldo Bicelli et al.	[PBBMD08]
Electrodeposition of nanostructured coatings and their characterization- a review	I. Gurrappa and L. Binder	[GB08]

**Table 3.2.:** The table notes some of the important reviews of electrodeposition in the literature.

removed by reactive ion etching in a  $\text{CF}_4 / \text{Ar}$  plasma (Sentech SI220, 400 W, 30 min). A thin layer of gold ( $\approx 20$  nm) is then sputtered onto the etched backside of the membrane. The Au film is finally used as an electrode for the galvanostatic deposition of Ni from a Watts bath (300g/lNiSO<sub>4</sub> · 6H<sub>2</sub>O, 45 g/L NiCl<sub>2</sub> · 6H<sub>2</sub>O and 45 g/L H<sub>3</sub>BO<sub>3</sub>) with the current density of about 10 mA/cm<sup>2</sup>. From the salts of the metals (*here*: nickel sulfate, nickel chloride with boric acid and water) a electrolytic solution is composed which upon application forms a polycrystalline metal layer on the sample. The anode and cathode placed in the electrodeposition cell are both connected to an external supply of direct current(see figure 3.7 anode and cathode (working electrode). When the power supply is turned on, the water is oxidized at the anode. At the cathode the cations are reduced to deposit the metal. From the choice of the composition of the watts bath and from the current density the grain size of the polycrystalline metallic deposition can be influenced. Moreover, saccharin is added into the solution to obtain more homogeneous grains[ESE95]. The Ni wires grow from the gold electrode up the modulated pores at a typical rate of approximately 1  $\mu\text{m}$  per minute.

### 3.2.2. Nanotubes by Atomic Layer Deposition

#### Nanotubes by ALD: principles

It was shown before that electrodeposition is suitable for growing wires, tubes can also be realized by electrodeposition[XYS+03, CAS+11, HSS+09]. The literature shows however that electrodeposition is not as general as ALD for making tubes. The process can not be easily controlled as with ALD, e.g. the wall thickness is not so simply to tune. The minimum of the wall thickness is over 10 nanometer, so the diameters are usually a view hundred nanometer. With ALD conformal coating and growing over large areas is assured. So, now the fabrication of tubes would be introduced. Other techniques such as evaporation or sputtering cannot be used to create tubes in the template. The shadowing effect hinders this. To realize long, homogeneous tubes in the template, ALD is a very suitable technique. Atomic Layer Deposition is a self-limited process to deposit adequate surfaces without any shadowing. The following small table(3.3) presents some of the important ALD reviews found in the literature.



title	author	references
ALD precursor chemistry: Evolution and future challenges	M. Leskelä and M. Ritala	[LR99]
Atomic layer deposition (ALD): from precursors to thin film structures	M. Leskelä and M. Ritala	[LR02]
Atomic Layer Deposition Chemistry: Recent Developments and Future Challenges	M. Leskelä and M. Ritala	[LR03]
Advanced electronic and optoelectronic materials by Atomic Layer Deposition: An overview with special emphasis on recent progress in processing of high-k dielectrics and other oxide materials	Niinistö et al.	[NNP <sup>+</sup> 04]
Surface chemistry of atomic layer deposition: A case study for the trimethylaluminum/ water process	R. L. Puurunen	[Puu05]
Synthesis and Surface Engineering of Complex Nanostructures by Atomic Layer Deposition	M. Knez, K. Nielsch and L. Niinistö	[KNN07]
Template-Directed Synthesis of Oxide Nanotubes: Fabrication, Characterization, and Applications	C. Bae et al.	[BYK <sup>+</sup> 08]
Atomic Layer Deposition: An Overview	Steven M. George	[Geo10]

**Table 3.3.:** The table gives a small overview of important reviews of atomic layer deposition in the literature.

As a new method to prepare thin films ALD was introduced in the late seventies. It was used to create thin films for ac thin-film electroluminescent (TFEL-)displays and later to prepare insulating layers.

Today ALD is commonly utilized to fabricate high-performance materials and form new types of nanostructures. It is used to prepare nanomaterials either in templates or to functionalize surfaces. ALD enables to fabricate noble metallic, semiconducting, insulating and magnetic materials.

The next table(3.4) gives a small overview into the possibilities of ALD materials. It will be differentiated between noble metals used e.g. for electronic parts, high-k-oxides which are e.g. used for gate oxides, insulating materials needed in (TFEL-)displays or magnetic materials used to analyze the magnetic properties for applications, also inorganic oxides and thermoelectric materials are exemplified. This thesis will focus on the magnetic material deposited by ALD. Since 2003 ferromagnetic material is deposited either on surfaces, on particles or in templates.

material	application	temperature	precursors	references
$\text{Al}_2\text{O}_3$	insulator	177°C	TMA deionized water	[ <a href="#">ERMG03</a> ] [ <a href="#">EG03</a> ] [ <a href="#">HVNV+11</a> ]
$\text{SiO}_2$	insulator	RT	$\text{SiCl}_4$ $\text{H}_2\text{O}$ $\text{NH}_3$	[ <a href="#">KG00</a> ] [ <a href="#">BZC+08</a> ] [ <a href="#">DDB+08</a> ]
$\text{HfO}_2$	high-k-oxide	300°C	$\text{HfCl}_4\text{O}$ $\text{H}_2\text{O}$	[ <a href="#">FKC+06</a> ]
$\text{ZnO}$	semiconductor	RT	DEZn $\text{H}_2\text{O}$	[ <a href="#">MSP+11</a> ]
$\text{Fe}_2\text{O}_3$	magnetic material	140°C	$\text{Fe}_2(\text{O}^t\text{Bu})_6$	[ <a href="#">BJK+07</a> ]*
Pt	noble metall	300°C	$\text{MeCpPtMe}_3$ $\text{O}_2$	[ <a href="#">ARS+03</a> ]
Ru	transition metall	300°C	$\text{Ru}(\text{EtCp})_2$ $\text{O}_2$	[ <a href="#">YLK+08</a> ] [ <a href="#">UEK11</a> ]
$\text{MgO}$	inorganic oxide	200°C	$\text{MgCp}_2$ $\text{H}_2\text{O}$	[ <a href="#">ZBMM+11</a> ]
$\text{Sb}_2\text{Te}_3$	thermoelectric material	60-70°C	$(\text{Me}_3\text{Si})_2\text{Te}/$ $\text{SbCl}_3$	[ <a href="#">GNB+11</a> ]

**Table 3.4.:** The table shows some examples of ALD materials and their applications, other materials can be found in the literature summed up in [[Puu05](#)]. References marked with a star \* include a reduction process to the specific metal. (TMA means trimethylaluminum and DEZn diethylzinc)

Some prominent publications in the field are listed in the table [3.5](#).

2003 Lim et al. fabricated transition metals by ALD on Si substrates. These metals were deposited with metal acetamidinate precursors[LRG03]. Another way to fabricate metals is to deposit complex oxides compounds which become magnetic after a reduction process in Ar/H<sub>2</sub>. Here, the hazardous use of hydrogen can be circumvented. Nilsen et al. have made Fe<sub>2</sub>O<sub>3</sub> from the iron precursor Fe(thd)<sub>3</sub> and ozone as a oxygen source on soda-lime-glass substrates[NLF+04] etc. In AAMs Fe<sub>2</sub>O<sub>3</sub> was deposited 2007 from Bachmann et al. with water and iron(III) tert-butoxide complex, Fe<sub>2</sub>(O<sup>t</sup>Bu)<sub>6</sub>[Puu05]. This fabrication of nanotubes by ALD ensued the same results as with ferrocene and ozone[BJK+07] which was also done by Rooth et al. 2008[RJK+08]. Moreover, a lot of experimentalists have deposited Fe<sub>2</sub>O<sub>3</sub> with ferrocene and ozone, either in AAMs, on sculptured thin films[EBJ+08, PMME+09, AZP+10, ZWB+11] or on carbon nanotubes[MIB+11]. Thin films of iron cobalt oxides with spinel-type structure are made by the atomic layer deposition (ALD) technique using Fe(thd)<sub>3</sub> (Hthd = 2,2,6,6-tetramethylheptane-3,5-dione), Co(thd)<sub>2</sub> and ozone as precursors were done by Lie et al. 2008[LBKN+08] on amorphous soda-lime glass, single-crystalline substrates of Si(100) and on MgO(100). More complex oxides were deposited from Zolotaryov et al. 2011, ZnCo<sub>2</sub>O<sub>3</sub>, CoFe<sub>2</sub>O<sub>3</sub> and ZnFe<sub>2</sub>O<sub>3</sub> were fabricated on substrates. Ternary ferrites (CoFe<sub>2</sub>O<sub>3</sub>,NiFe<sub>2</sub>O<sub>3</sub>) were deposited 2011 by Chong et al. The cyclopentadienyl complexes of Fe(II), Co(II), and Ni(II) (metallocenes, Cp<sub>2</sub>M) are combined with ozone for the ferrite ALD reactions[CYY+11]. Ni oxide and Co oxide was deposited 2007 by Daub et al. in AAMs[DKGN07] using nickel- and cobaltocene and ozone as precursors. (Zn,Co)O was fabricated 2008 by Lukasiewicz either on substrates [LWGG+08]or on sapphire, GaAs and Si[LWG+10]. (Zn,Co)O films were grown at low temperature (T<sub>s</sub> = 160°C) with a new zinc precursor (dimethylzinc-DMZn) and with cobalt(II) acetylacetonate (Co(acac)<sub>2</sub>) as a cobalt precursor and deionized water as an oxygen precursor[LWGG+08]. Also, Godlewski deposited (Zn,Co)O on substrates 2011[GGL+11]. All studied (Zn,Co)O films were grown by the ALD on silicon substrates using Zn, Zn(acac)<sub>2</sub>, H<sub>2</sub>O and Cobalt(II) acetylacetonate as Zn, O and Co precursors, respectively[GGL+11]. TiO<sub>2</sub>/Fe<sub>2</sub>O<sub>3</sub> was fabricated 2009 in AAMs[SRL+09]. Double- and triple-walled TiO<sub>2</sub>/iron III oxide nanotubes with well defined interfaces have been produced in nanoporous alumina templates using atomic layer deposition[SRL+09]. TiO<sub>2</sub>/Co was deposited 2011 by Pore. TiO<sub>2</sub> thin films doped or mixed with cobalt oxide were grown by atomic layer deposition using titanium tetramethoxide and cobalt(III)acetylacetonate as metal precursors. The films could be deposited using both O<sub>3</sub> and H<sub>2</sub>O as oxygen precursors[PKD+11]. At last position in the table MnCo<sub>2</sub>O<sub>3</sub> was fabricated on Si (100) by Uusi-Esko in 2010. Spinel-structured (Mn,Co)<sub>3</sub>O<sub>4</sub> thin films were reproducibly fabricated by atomic layer deposition (ALD) using Mn(thd)<sub>3</sub>, Co(thd)<sub>2</sub>, and ozone as precursors[UERL+10]. The table 3.4 shows also that for most of the processes magnetic properties have been analyzed.

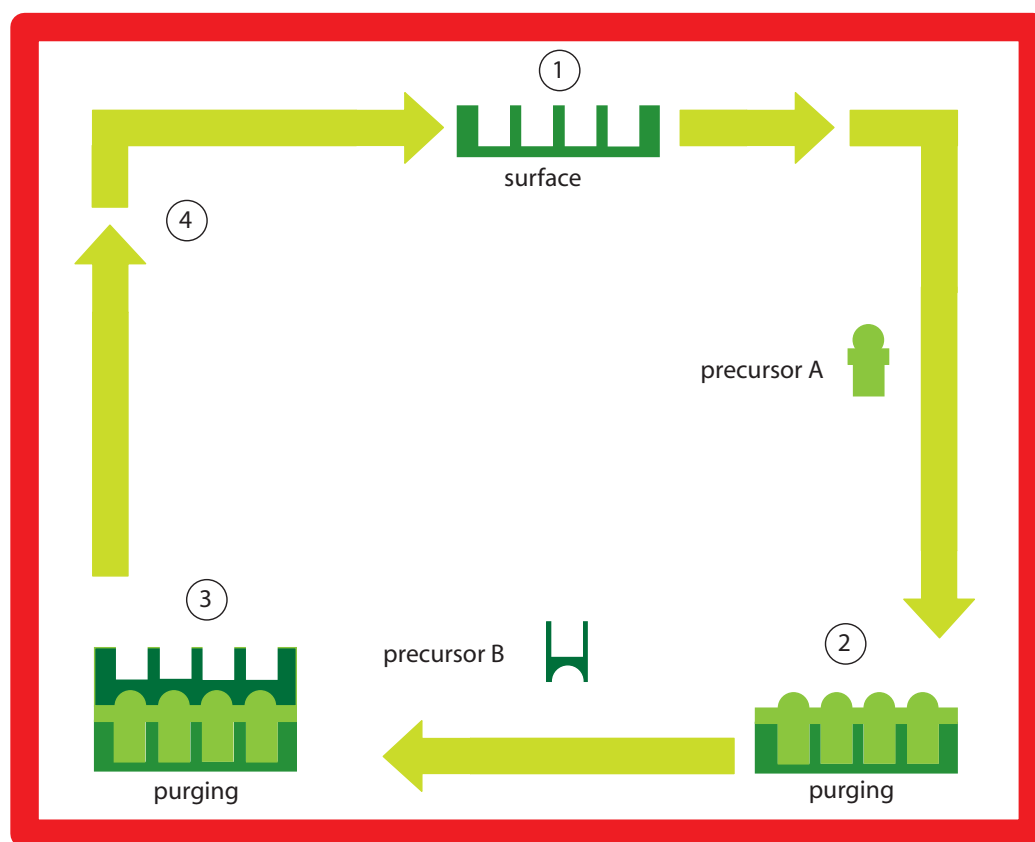


**Figure 3.8.:** The ALD process is divided into two stages which consist of a view steps. This is illustrated in the scheme. The process starts with (1) and ends with (4). Afterwards it can be repeated as desired. The thickness of the layer grows proportional to the number of cycles.

### Nanotubes by ALD: method

The Atomic Layer Deposition is a process which is technically realized in a vacuum chamber. The base pressure is about one pascal. Materials are deposited in the chamber with varying the deposition temperature between 20 to 250°C. In the first step the surface is exposed to reactive molecules in the gas phase (number 2 in figure 3.8). As these molecules after reacting with the surface are not forming the final layer, but an intermediate layer, they are called precursor molecules or precursors. To get them into the gas phase and to react with the surface, the molecules in the precursor should have the significant vapor pressure. This vapor pressure, controlled by the temperature in the chamber and precursor bottles, should be so high to ensure an effective material transport.

The reacting materials are molecules which are available as gases, fluids or solids. The last ones have to be heated to get an adequate vapor pressure. If the

precursors have bond with the whole surface, the surface is covered with a monolayer of intermediate product consisting of the precursor molecule and the origin material. Now, the first step of the growth process is finished, and the chamber is purged of the first precursor. Now the second precursor is pulsed into the chamber and reacts with the intermediate layer(number 3 in figure 3.8). At the same time the required deposition remains on the surface. When the next reaction has taken place, no more precursor molecules can bond onto the chemically saturated surface. This defines the self-controlled aspect of ALD and is the hallmark. After the second precursor has been removed, a full ALD cycle has been completed. Such a cycle takes a few seconds, in which a layer of thickness between 0,01 and 0,3 Å is deposited. Afterwards the process can be alternatively repeated, to increase the coating layer thickness of the sample. The thickness is mainly proportional to the number of cycles[Pit09].

All detailed information to the different ALD processes are given in the experimental chapters and in the appendix (see table A.1, A.2, A.3 and A.4). The ALD of Fe<sub>2</sub>O<sub>3</sub> and SiO<sub>2</sub> is performed in a Savannah 100 Reactor by Cambridge Nanotech according to the published procedures from ferrocene and ozone[EBJ<sup>+</sup>08], and from 3-aminopropyltriethoxysilane, water and ozone[BZC<sup>+</sup>08], respectively(see table A.1 and A.2).

The ALD of NiO and nickel/ cobalt oxide is also performed in the same reactor according to the published procedures from nickelocene and ozone[DKGN07], and from nickelocene and cobaltocene and ozone (see table A.3 and A.4).

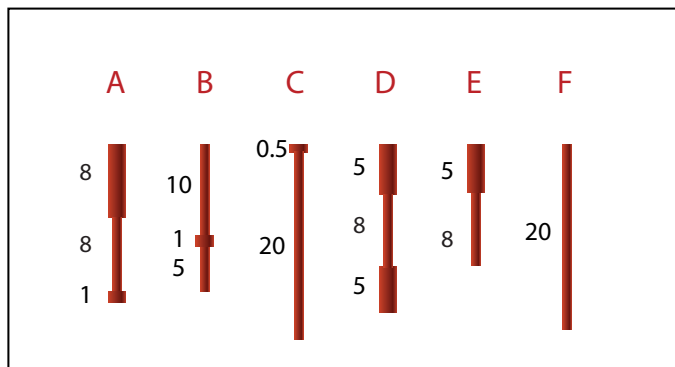
layer	substrate	temperature	precursors	growth- <sup>2</sup> rate	references
Ni/Co/Fe	SiO <sub>2</sub> substrate	260-350°C	metal-acemidinate/ hydrogen gas		[LRG03]
Fe <sub>2</sub> O <sub>3</sub>	AAM	200°C	Fe(Cp) <sub>2</sub> O <sub>2</sub> / O <sub>3</sub>	0.02 $\frac{\text{nm}}{\text{cycle}}$	[BJK+07]* **
Fe <sub>2</sub> O <sub>3</sub>	AAM	140°C	Fe(O <sup>t</sup> Bu) H <sub>2</sub> O/	0.025 $\frac{\text{nm}}{\text{cycle}}$	[BJK+07]* **
Fe <sub>2</sub> O <sub>3</sub>	AAM	200°C	Fe(Cp) <sub>2</sub>		[EBJ+08]* **
Fe <sub>2</sub> O <sub>3</sub>	carbon nanotubes	350°C	Fe(Cp) <sub>2</sub> - powder O <sub>2</sub>		[MIB+11] **
CoO/FeO	amorphous soda-lime glass and single- crystalline substrate of Si(100), MgO(100)and $\alpha$ - Al <sub>2</sub> O <sub>3</sub> (001) substrate	185-310°C	Fe(thd) <sub>3</sub> / Co(thd) <sub>2</sub> / O <sub>3</sub>		[LBKN+08]* **
CoFe <sub>2</sub> O <sub>3</sub>	substrate	250°C	Co(II), Fe(II)- metallocenes O <sub>3</sub>	0.04 $\frac{\text{nm}}{\text{cycle}}$	[CYY+11]* **
NiFe <sub>2</sub> O <sub>3</sub>	substrate	200°C	Ni(II), Fe(II)- metallocenes O <sub>3</sub>	0.03 $\frac{\text{nm}}{\text{cycle}}$	[CYY+11]* **
NiO	AAM	330°C	nickelocene O <sub>3</sub>		[DKGN07]* **
CoO	AAM	330°C	cobaltocene O <sub>3</sub>		[DKGN07]* **
ZnCoO	substrate	160°C	DMZn <sup>3</sup> DEZn <sup>4</sup> cobalt(II) chloride- hydrate deionized water		[LWGG+08]* **
MnCo <sub>2</sub> O <sub>3</sub>	Si (100)	140-160°C	Mn(thd) <sub>3</sub> Co(thd) <sub>2</sub> O <sub>3</sub>	0.02 $\frac{\text{nm}}{\text{cycle}}$	[UERL+10]

**Table 3.5.:** The table shows some examples of magnetic material ALD processes and which templates have been used for the deposition. References marked with one star \* include magnetic characterization and with two stars \*\* include a reduction process of the specific metal.

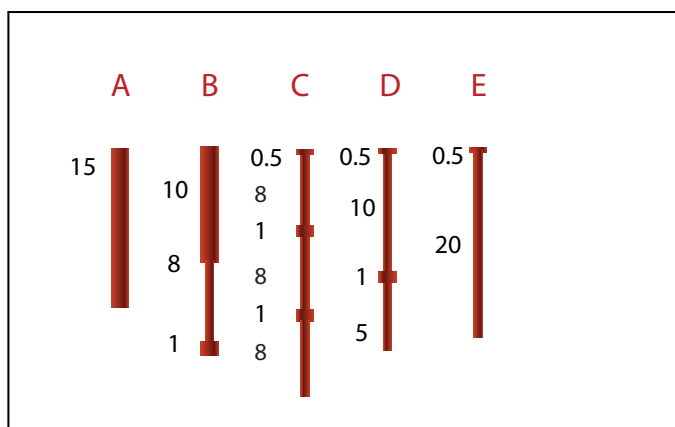
### 3.3. Overview of the prepared samples

The following figure 3.9 gives an overview of the prepared samples in this thesis. The reader will always be referred to this figure in the experimental chapters. In this thesis series of samples were prepared, one consisting of nickel nanowires with different diameter variations, also nanotubes fabricated with ALD consisting of  $\text{Fe}_3\text{O}_4$ , Ni and nickel/cobalt oxide. The nickel/ cobalt oxide process is presented here the first time, so this was the beginning of synthesizing a run of nickel/cobalt tubes.

(a) Nickel wires by electrodeposition



(b) Fe<sub>3</sub>O<sub>4</sub> nanotubes by ALD



(c) Ni/ NiCo nanotubes by ALD

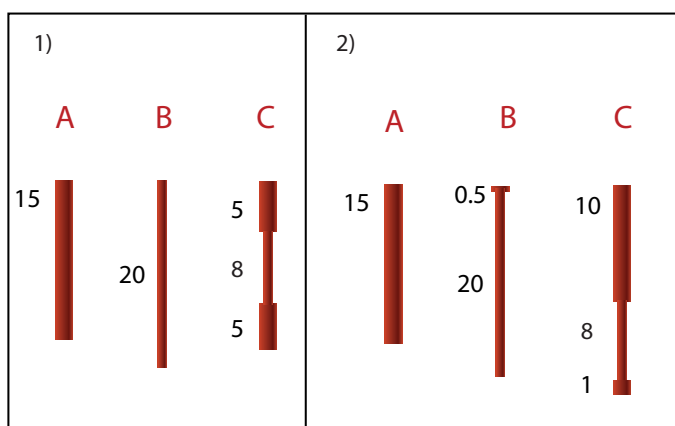


**Figure 3.9.:** The figure gives an overview of the prepared samples in this thesis. Nanowires by electrodeposition and nanotubes by ALD were prepared. The length of the different diameter segments were illustrated and defined in  $\mu\text{m}$ .



## 4. Structural and magnetic characterization methods

In this chapter the reader is provided with an insight into the structural and magnetic characterization methods. First, different structural and morphological characterization methods e.g. scanning electron microscopy (SEM) and transmission electron microscopy (TEM) are shortly introduced. Subsequently, the experimental setups for the magnetic characterization such as the superconducting quantum interference device (SQUID), the vibrating magnetometer (VSM), the magneto-optical Kerr effect (MOKE) magnetometer used to characterize the magnetic properties of prepared samples in this thesis are presented.

### 4.1. Structural characterization

To investigate the geometric parameters of the prepared samples a scanning electron microscope (SEM) is one of the most convenient characterization methods. In a SEM, the electron beam scans the surface of the sample in a raster pattern. The interaction of the electron beam and the surface give information regarding surface morphology, composition of the sample etc.

The beam electrons which came out of electron source, here a hot cathode consisting of wolfram wire, produce so-called secondary electrons via ionization of the surface atoms. Depending on the material, different amounts of electrons reach the surface and are detected by an electron detector. The shadowing and edging effects give topographical information on the sample. The energy of the secondary electrons is low ( $< 50$  eV), so they result from the near sample surface (about 10 nm depth).

If the x-rays (the high-energy beam of electrons) are generated deep into the sample's surface, they can be used for the EDX (energy dispersive x-ray spectroscopy) technique. The characteristic emission lines of the electrons give information of the particular material. This delivers a compositional information of the sample[Gol03]. The micrographs are taken on a Supra55 or an Evo50 by Zeiss under an acceleration voltage of 10 kV. In figure 4.1 the scanning electron micrographs of the perfectly ordered porous anodic alumina template is shown. The membrane is displayed in section, pores are broken in halves along their  $z$  axis. By checking the lattice parameters, the best working synthesis can be chosen (out of the array of parameter variations).

To complement SEM, where only the surface topology can be investigated, TEM is used to get more insight of the samples and has a higher magnification than SEM. In general the magnification of a SEM has a wide range from 10 to

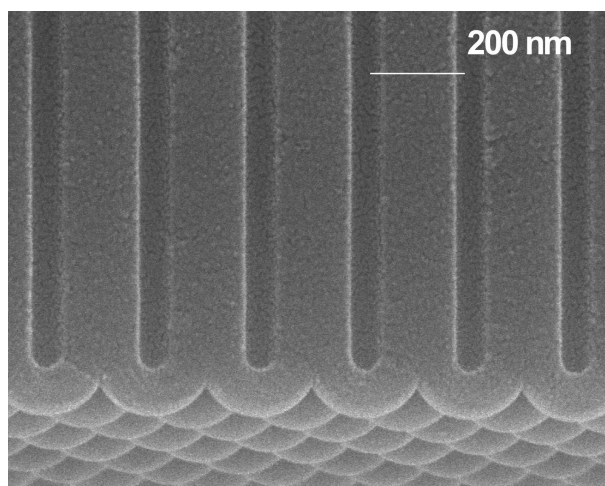


**Figure 4.1.:** Scanning electron micrographs of the porous anodic alumina template. The membrane is displayed in section, pores are broken in halves along their  $z$  axis.

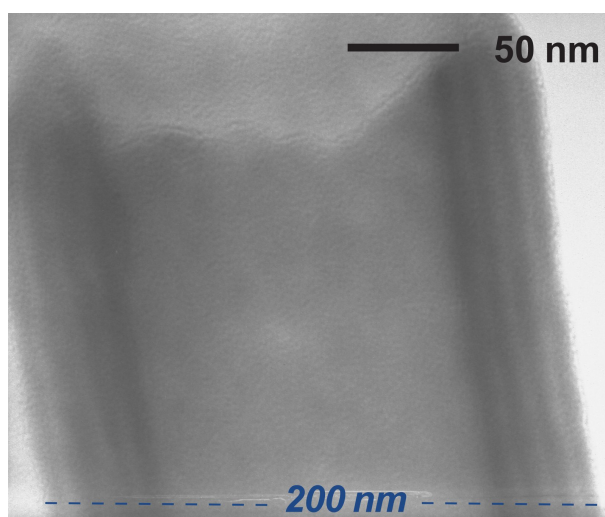


**Figure 4.2.:** Transmission electron micrograph of an isolated multilayered  $\text{Fe}_3\text{O}_4$  and  $\text{ZnO}_2$  tube (layer thicknesses: 10 nm and 5 nm), the diameter of the pore is about 200 nm, the length of the tubes is 10  $\mu\text{m}$ .

500 000 times, but TEM has even a wider range up to 50 000 000 times. Here, the absorption/ scattering of the primary electrons is analyzed; which delivers an image of the morphology: the e-beam diffraction helps to analyze the crystal structure and the x-ray analysis to get information of chemical composition of the sample[WC09]. Transmission microscopy was performed on a Jeol JEM1010 operating at 100 kV or on a Philips TEM 400 T operating at max. 120 kV. TEM samples are prepared by dissolving the alumina matrix in 0.33 mol/L Cr(VI) with 0.6 mol/L concentrated phosphoric ( $\text{H}_3\text{PO}_4$ ) acid for 40 h at  $45^\circ\text{C}$ , diluting the resulting suspension, and letting a drop of it evaporate on a holey carbon/ Cu grid. In figure 4.2 multilayered  $\text{Fe}_3\text{O}_4$  and  $\text{ZnO}_2$  tube (layer thicknesses: 10 nm and 5

nm) tube is shown, the different layers can clearly be seen and the diameter is about 200 nm.

## 4.2. Magnetic characterization

In this work magnetometry is used for the characterization of different magnetic nanowires and nanotubes. Here, on the one hand inductive magnetometers were available such as the SQUID magnetometer (MPMS-2/MPMS-XL, QuantumDesign) and the vibrating magnetometer (VSM, Versalab QuantumDesign) and on the other hand a NanoMOKE called NanoMOKE2 which is made by Durham Magneto Optics Ltd.

Magnetometry in general is used to get information about the magnetization of the magnetic sample. The inductive magnetometers detect the magnetic properties over whole sample volume, the absolute magnetization can be measured. In opposite to this technique it is not possible to detect the absolute magnetization with a NanoMOKE magnetometer. The magneto-optical Kerr-effect is used with this technique and differs in the surface sensitivity in contrast to the inductive magnetometry.

### 4.2.1. Magnetometry of ensemble nanowires and nanotubes

The measuring principle of inductive magnetometry is the following: a sample is moved through pickup coils in an applied magnetic field, so that the magnetic flux is changed. A voltage is induced in the pickup coils which enclose the sample volume. This voltage is then proportional to the magnetization of the sample. The main difference between SQUID and VSM is the measuring process. In a SQUID the sample is moved once through the pickup coils, so a high sensitive detection is needed. This is realized by a SQUID device. In a VSM the sample is vibrated, so the induced voltage at the pickup coils can be detected by a lock-in technique.

#### SQUID magnetometer

Generally in a SQUID setup the magnetic flux of a sample is detected with a high sensitivity. With a SQUID smallest magnetic moments ( $10^{-7}$  emu) can be measured precisely. The main part of the SQUID is the superconducting quantum interference device. In figure 4.3 a general setup is illustrated. There are superconducting coils which generate a constant magnetic field ( $\pm 5$  Tesla for the MPMS-XL and  $\pm 1$  Tesla for the MPMS-2). The magnetic field operates along the symmetry axis of the sample. There is a sample handling system which can move the sample, so a calibration at a certain position is possible. This is implemented by a microstep controller. During a measurement the sample is moved at low frequency through two pickup coils (see figure 4.3) and the magnetic coil. This system of pickup coils is made of a superconducting niobium wire and is wound as a gradiometer of second order. This gradiometer not only compensates the constant stray fields but also external field gradients. The system is superconducting, so only four single conductor loops can be used instead of a

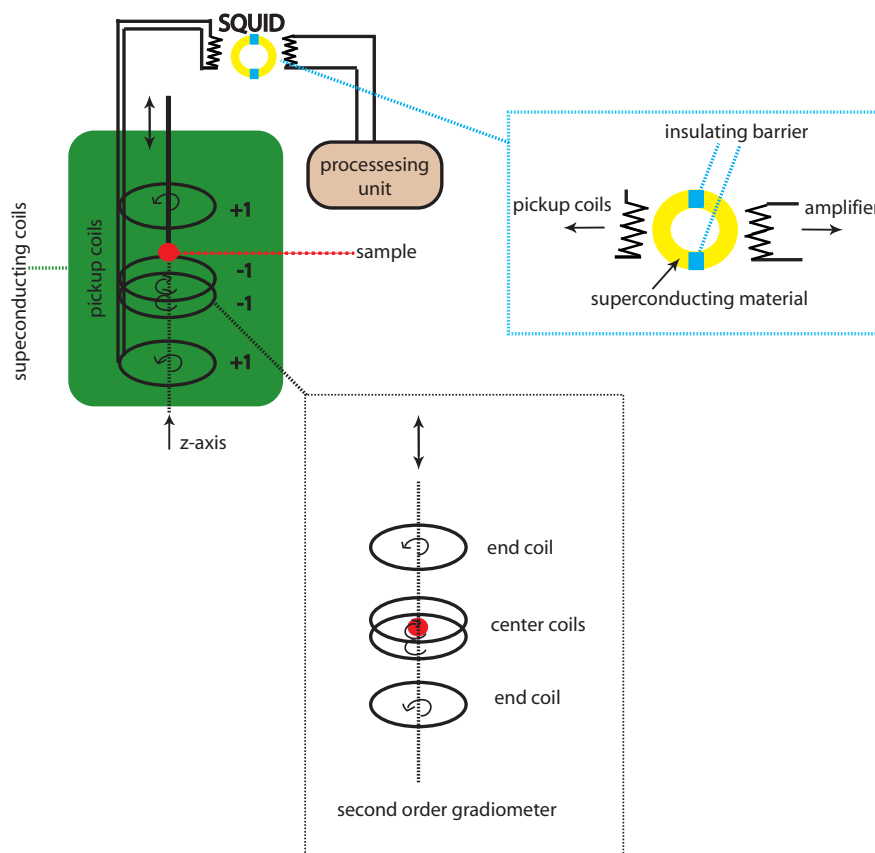


**Figure 4.3.:** The pickup coils are wound as a gradiometer of second order. Because of the coil design the environmental noise is reduced. The sample is moved through the experiment by a stepper motor. There is a magnetic flux inside the coils. This SQUID has two insulating barriers inside the ring. It realizes the digitization of the flux-change recorded by the pickup coils. Similar to [Nie02] and [Alb10].

whole coils. The oscillating stray field of the sample induces a change in the coil current in the gradiometer. Because of Faraday's law the voltage induced at the pickup coils is proportional to the time dependent change of the stray field and proportional to the magnetic moment of the sample. This field change in the sample space results in an electric signal which passes from the pickup coils to the actual SQUID device by superconducting contacts. Extremely weak magnetic fields ( $10^{-9}$  Oe) can be measured over a complex electric read-out unit by the SQUID device [Nie02]. The principle of this sensitive measurement is the Josephson-effect [TK80]. The SQUID device consists of a superconducting current circuit with two Josephson contacts (discontinuations). These contacts are made of

an insulating material(see figure 4.3).

A detailed description of the system used is given in [Alb06]. The superconducting components of the SQUID setup (see figure 4.4) can only operate in a liquid- $^4\text{He}$ -cryostat. The temperatures of the sample during the measurement can be varied from about 2 to 400 K for the MPMS-XL and from about 2 to 350 K for the MPMS-2 (see figure 4.4).

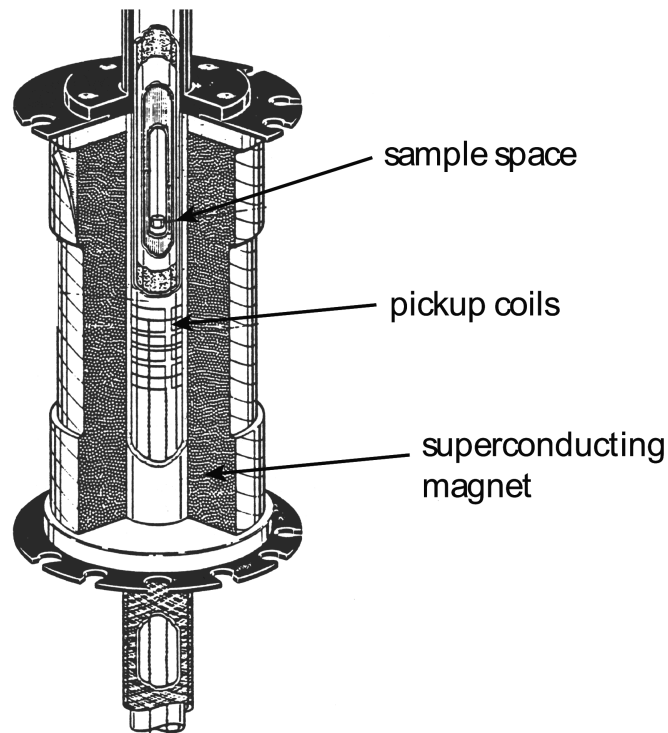


**Figure 4.4.:** The drawing illustrates the sample space, the pickup coils and the magnetic field coils[Des90].

**Field-dependent magnetization.** In a field-dependent measurement at a constant temperature the magnetization isotherms of a ferromagnetic sample are investigated. Figure 4.5 displays the typical magnetization isotherms of a ferromagnetic sample. This was already mentioned in chapter 2, section 2. The hysteresis has a clear shape. The values are measured in discrete field steps. These field intervals can be reduced around the important parameters ( $H_C$  and  $M_{rem}$ ) to measure them more precisely. So, the measurement can become imprecise if the field steps are too big.

Three values can be read out from the hysteresis. (a) The point where no further increase of the magnetic moment can be observed is the saturated magnetic moment, this is shown in figure 4.5. All magnetic moments are aligned parallel at a strong applied field. (b) The remanent magnetic moment is defined at zero magnetic field. (c) The coercive field is the field needed to demagnetize the sample, the magnetic moment is zero. For wires and nanotubes the field which is necessary to destabilize the aligned state and to induce magnetic reversal is called nucleation

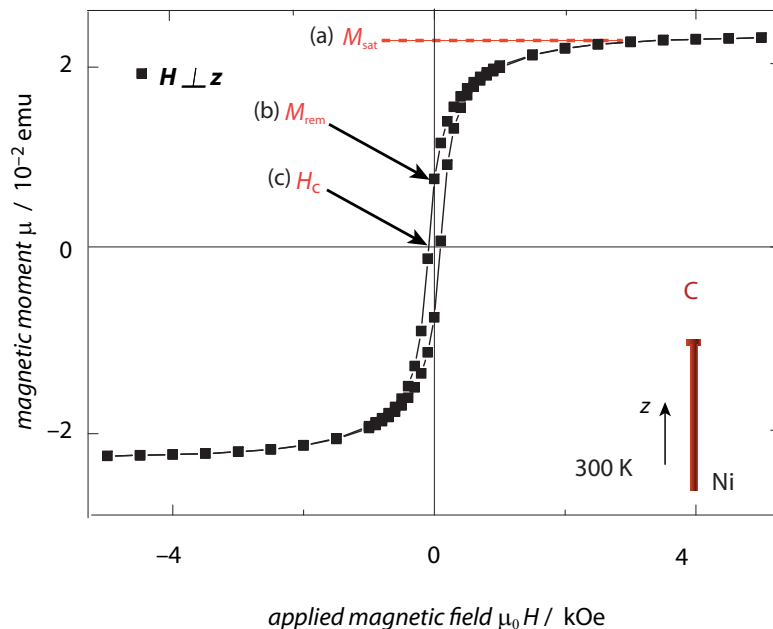


**Figure 4.5.:** A hysteresis curve of a nickel wire array with one modulation is shown (thick  $0.5 \mu\text{m}$ , thin  $20 \mu\text{m}$ ). Typical magnetization isotherms are displayed in (a) the saturated magnetic moment. The point where no further increase of the magnetic moment can be observed is the saturated magnetic moment, this is shown in figure 4.5. All magnetic moments are aligned parallel at a strong applied field. (b) the remanent magnetic moment which is defined at zero magnetic field. (c) the coercive field is the field needed to demagnetize the sample, the magnetic moment is zero.

field. The reason for this is the nucleating domain wall at the end of the structure. After saturation in high fields, the magnetization configurations starts to change.

**Temperature-dependent magnetization.** With the SQUID both field- and temperature-dependent measurements are possible. There are three main procedures for the determination of the temperature-dependent magnetization  $M(T)$ : the Zero Field Cooling (ZFC), the Field Cooling (FC) and Remanence (REM)-method. The previous history is the most important: which leads to different magnetizations at low temperatures. Figure 4.6 shows the ZFC and the FC method in a curve of iron III oxide tubes (first charge of tubes with not optimized fabrication steps) with a diameter of  $150 \text{ nm}$  and a length of  $20 \mu\text{m}$ . The sample is cooled at a zero magnetic field, then during the zero field cooling measurement the sample is heated up at a small applied magnetic field. The

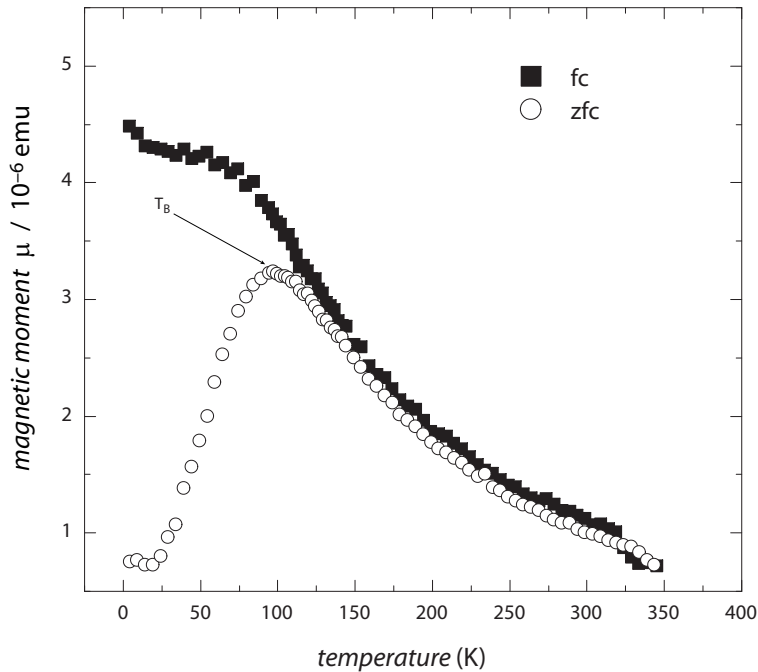


**Figure 4.6.:** The curve illustrates the two procedures of measuring the temperature-dependent magnetization: zero field cooling and field cooling. Shown is a sample of iron III oxide nanotubes which behave superparamagnetic, defined by the characteristic  $T_B$ , the zfc and fc curve. The measurement was done at an applied field of 100 Oe.

induced magnetization is measured versus temperature. In the beginning of the zfc curve, the particles are in the state a of figure 2.18. The particles are unordered, cooled down in zero magnetic field, the spins are frozen and the magnetization is zero. The ordering of the spins increases with a rising temperature. When the blocking temperature is reached, the magnetization has its highest value (see 2.18 blocking temperature is sketched in). In this example (see figure 4.6) the blocking temperature for the iron III oxide tubes is about 102 K. The thermal fluctuation in this peak is not so big, so the spins can order uniformly. When the temperature gets higher, the thermal fluctuation plays the biggest role and the magnetization decreases. The spins can rotate freely (s. figure 2.18 b) During the fc measurement the sample is cooled down in an applied field and the magnetization is detected (see figure 4.6). Here, the magnetization is saturated. The spins have aligned after another in the field and are frozen.

At last the remanence is explained. The remanence measurement is performed during warm-up in zero field. With the remanence measurement not only the

superparamagnetism can be detected, the REM-method enables the detection of ferromagnetism e.g.. If the ferromagnetic order is lost, the transition between these states can be measured.

**Sample mounting** For sample mounting an uncolored polypropene (PP) straw is used because the material has a low susceptibility, it also has a uniform material distribution to reduce the unwanted background signal from the sample holder. The straw is used as an outer shell. Inside the straw a sample holder of paper is put which is built with a surface parallel or orthogonal to the magnetic field. On this paper holder the sample is glued with cryogenic high vacuum grease<sup>1</sup>. With these two different designs of paper sample holders, it is possible to use the field inplane or out of samples plane. In this manner, anisotropy effects such as the easy and hard axis of samples can be observed. With the magnetometry it is achievable to calculate the volume magnetization when the volume of the sample is known and compare this to literature values. If the measuring signal is very low and in the limit of the detection range, smallest misalignment in the sample mounting (perpendicular and parallel alignment of the sample along the applied field) have big effects on the measured signal, so this can result in different strengths of the signal. In this case the measured values have to be normalized to the saturated magnetization and then they can be compared.

In opposite to the VSM the measurement of a sample by a SQUID is time-consuming, the sample has to be moved slowly through the coils (scans). So, to get a good signal to noise ratio the scans take a lot of time.

## VSM

The commercial setup 'VersaLab free' is a computer controlled measuring setup in modular configuration. Different parameters can be regulated during a measurement: temperature  $T$ , magnetic field  $M$  and atmospheric pressure  $P$ . The instrument consists of two blocks, the bigger one includes the sample space, the cooling units, the magnetic coil and the electronics. The other one is a compressor. The cryostat (two step pulse-tube cryo cooler) works as a cooling machine. An external helium filling is not necessary to reach low temperatures. The reached temperature is lower than the transition temperature of NbTi (comprising the installed solenoid) (11 K), so it can be used in the superconducting state. Magnetic fields of 3 T can be reached at 20 A. The VSM is designed for the measurement of the electrical and thermic properties of samples but also for the application as a vibrating-sample-magnetometer. For this inductive measurement the pickup coils are put down in the sample space. The mechanic excitation of the sample (vibration in  $z$ -axis) is carried out by a handling system of the sample bar on the attached VSM-head. Two added insertion cards incur the controlling of the motor and the synchronic detection of the induced voltage [Mar11]. The sample is placed in the sample holder by a sample rod into an applied magnetic field (see figure 4.7) and then is vibrated sinusoidally. This is realized by a piezoelectric material. During a measurement the magnetic flux is changed which induces a voltage in the pickup coils that encloses the sample volume. This induced voltage is measured.

---

<sup>1</sup>Apiezon N Grease



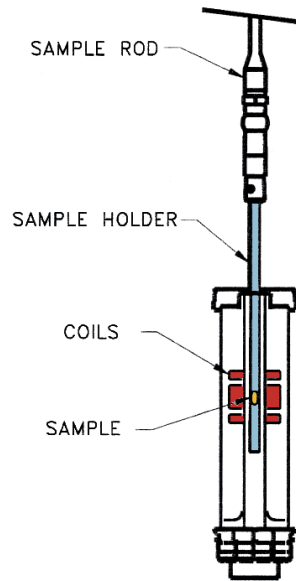


**Figure 4.7.:** Schematic drawing of the VSM setup[Qua08].

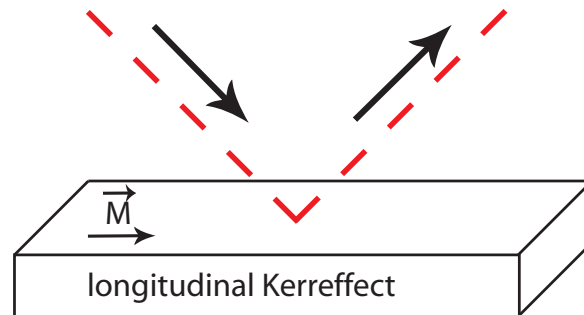


**Figure 4.8.:** Schematic drawing of the used longitudinal Kerreffect. Similar to[Alb10].

The mechanic movement of the sample is realized as a harmonic oscillation and has a frequency about typically 80 hz. The induced voltage is alternating voltage with an amplitude proportional to the frequency, to the magnetization of the sample and to the mechanic amplitude of the deflection. The induced voltage is measured with a lock-in amplifier, the piezoelectric signal is then used as its reference signal. The magnetic moment of the sample is measured in dependence of the applied field, so one can obtain the hysteresis of the measured sample.

### 4.2.2. Magnetometry of single nanowires

#### MOKE magnetometer

The MOKE measurement is based on the principle of the magneto-optical Kerr-effect. It was published 1877 by John Kerr[Ker77]. The change of the

polarization of the reflected light in the used geometry in dependence of the magnetization is defined as the longitudinal, polar and transversal Kerr-effect. Here, only the longitudinal Kerr-effect (LMOKE) is used which is illustrated in figure 4.8. The MOKE setup is schematically illustrated in figure 4.9 (top) and also a picture of the setup is given (bottom). In longitudinal configuration, the sensitive direction for magnetic measurements is oriented parallel to the surface of the sample and parallel to the plane of incidence (see also figure 4.8). The magnetization  $M$  lies in the reflection plane. The surface sensitivity of the MOKE in which the laser spot pervades the surface layers is also a difference to the inductive magnetometry of the SQUID measurements. After reflected from the magnetized surface, the linearly polarized light is transformed into elliptical one with an analyzer detector pair. This change generated a detectable voltage modulation which is proportional to the  $M$ -component mentioned above. Noise reduction is realized by averaging the signal over many single loops. This procedure is done by applying a sinusoidal field with an amplitude of up to 700 Oe and a frequency between 0,3 and 28 Hz. The spotsize can be changed by different lenses. Smaller spot size enable more measurable signal for nanostructures because of the ratio of sample and spotsize, also the ratio background to sample reduces the noise. The angle dependent coercive fields of films and nanostructures can be measured by the sample stage which is rotatable over a range of  $\pm 165^\circ$ . The lateral resolution or rather the spot size facilitate the directed measurement of the desired single nanostructure, in contrast to the SQUID measurement where the magnetic properties are always the average of an ensemble of wires. However, it is not possible to determine the absolute magnetization values, one can only obtain information of the surface. The values are always relative and normalized to the saturated state. More details to this commercial setup can be found in[LTD]. Figure 4.10 shows a hysteresis curve of a single nickel nanowire. The diameter of the wire is about 80 nm and the length 5  $\mu\text{m}$ . In the beginning the external applied field  $H$  is high to saturate the sample, all spins are aligned in the same direction. Reducing the field entirely to zero, the magnetization stays here constant,  $M_{rem} = M_{sat}$  (see Figure 4.10). To get a zero magnetization an opposite field has to be applied with a value of the coercitivity  $H_C$ . The magnetization reversal in such nanowires is working via a nucleating and propagation of a domain wall (see chapter 2.4). In this single wire the nucleation point of the domain wall and the depinning of the wall and so the switching field ( $H_C$ ) where the magnetization is reversed are the same.

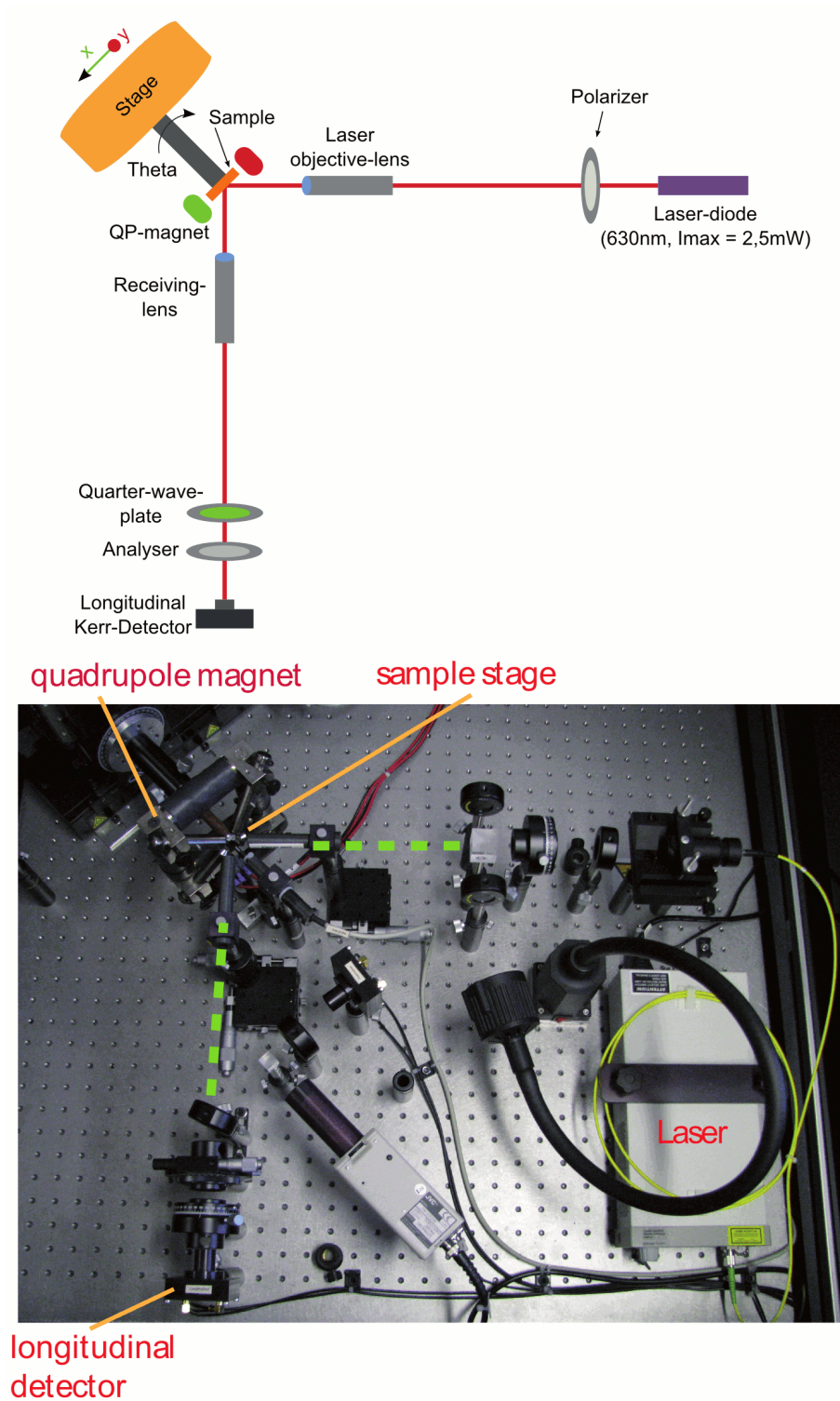


**Figure 4.9.:** Top: schematic drawing of the NanoMoke2™ setup for the determination of the magnetization at room temperature. Bottom: picture of the setup. Equal to [Alb10].

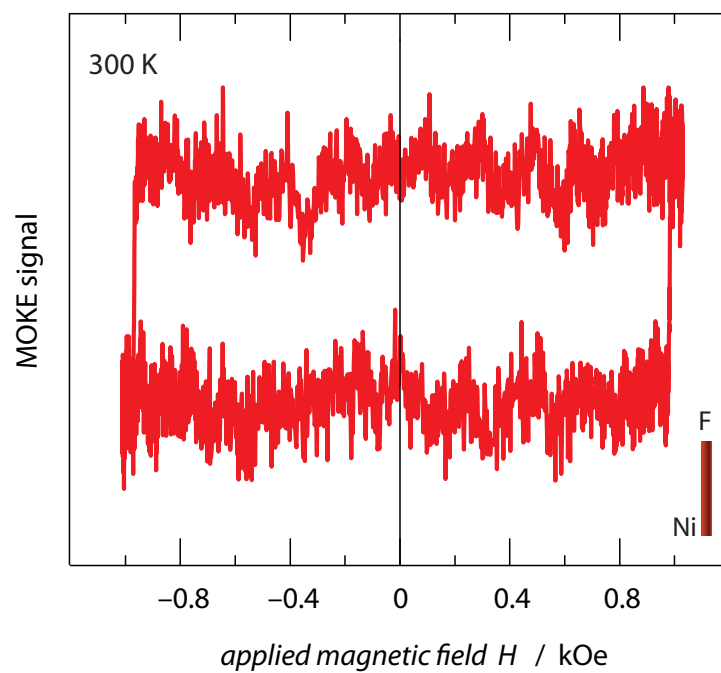


**Figure 4.10.:** Single-wire magneto-optical (MOKE) hysteresis loops of one unmodulated wire.

# 5. Ni nanowires

The nanowire and nanotube samples made of different materials are analyzed by characterization methods and theoretical treatments. This sheds light on the relevant magnetical phenomena in these structures. The relevant reversal processes in wires and tubes are characterized and the pinning/ the depinning of domain walls is preferred to be investigated. First, the nickel system fabricated by electrodeposition are discussed. A figure of all used samples in this chapter can be found in figure 3.9 (a). The relevant samples for each chapter are always introduced and shown in the figures.

## 5.1. Introduction

Here, in this thesis the pinning and depinning of domain walls will be analyzed. These effects were commonly observed on planar structures in the past years. So-called notches were fabricated by E-beam lithography[ORZ<sup>+</sup>09, HTM<sup>+</sup>08]. To investigate the pinning and depinning such notches were needed as nucleation points for the pinning and depinning of domain walls. However, these planar structures allow only the inplane transverse or vortex-walls. More complex ones can be found in cylindrical wires (see chapter 2.4) which can be realized by AAM-templates. Moreover, cylindrical wires were fabricated with different numbers of diameter modulations which should work as nucleation points for the pinning and depinning of domain walls. Here, the analyzing of cylindrical metal nanowires by electrodeposition utilized in perfectly ordered anodic alumina membranes is presented. The fabrication can be found in chapter 3.2.1. The template is perfectly ordered (see chapter 3.1.2), so that the environment of the each wire in the ensemble is the same. The wires in the ensemble are comparable and differences in geometry (radius) can be analyzed. Also, the filling of the pores is mostly the same, so that the lengths are comparable. This will be discussed later in section 5.2.2. The work is based on the large body of literature dealing with the electrodeposition of magnetic wires in porous templates such as anodic alumina (more details can be found in chapter 3.2.1) [XYS<sup>+</sup>03, LGY04, YZL05, HCD<sup>+</sup>08, AG02, BTH<sup>+</sup>04, CSRC05, HCY<sup>+</sup>05, FP99, PLK<sup>+</sup>01, KBG<sup>+</sup>02].

(i) The utilization of a nanoimprinted, perfectly ordered anodic alumina membrane as a porous template defines length and diameter of the wires as well as their hexagonal order, and (ii) the conformal filling of the cylindrical pores with magnetic substances by electrodeposition furnishes large numbers of objects in a simple procedure. In order to investigate the pinning of domain walls, diameter modulations can be introduced in this framework by combining the so-called 'hard' and 'mild' conditions for the electrochemical formation of the template (see more

details chapter 3.1.2)[LSG08, LSS+08]. Electrodeposition is used subsequently for the growth of metallic wires that replicate the diameter modulations defined in the template. At first, individual nanowires are investigated at the single-object level by spatially resolved MOKE magnetometry. Second, the wires are measured in organized arrays by ensemble (SQUID) measurements. At each step, a theoretical treatment sheds light on the relevant physical phenomena. At first, the influence of the diameter modulations, and then, the effect of dipolar interactions with neighboring magnets are discussed. The stray fields causing these interactions are evidenced by magnetic force microscopy.

Figure 3.9 (a) shows the various types of nickel nanowires prepared in this thesis. The labeling A–F will be followed consistently throughout the chapter. Figure 5.1

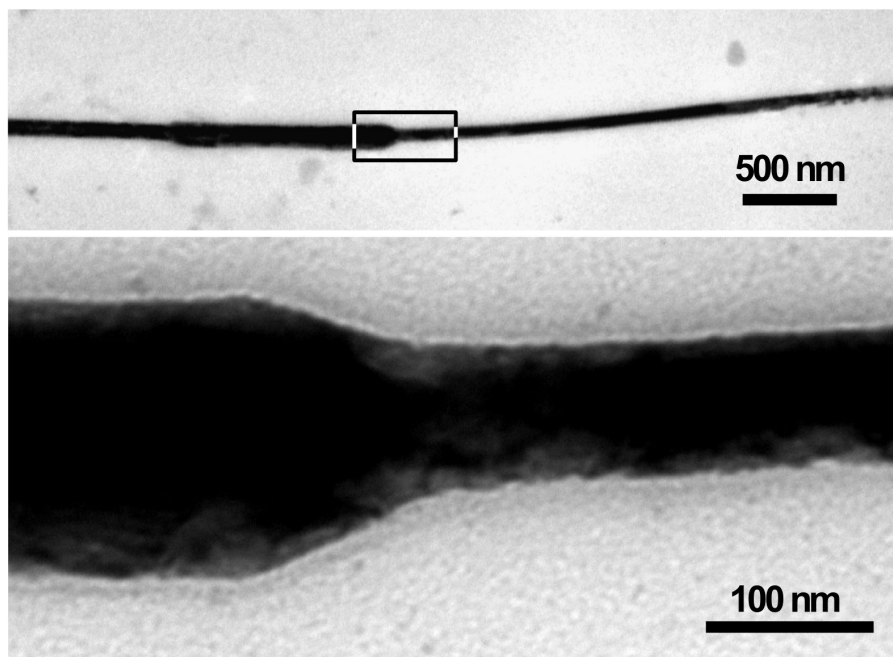


**Figure 5.1.:** Transmission electron micrographs of a single modulated Ni wire. Top, low magnification image showing two diameter changes. The area defined by the rectangle is further magnified in the lower panel.

displays a transmission electron micrograph of a Ni wire obtained after release from the alumina matrix in chromic acid. The diameter modulations of the template between values of approximately 90 nm and 170 nm ( $\pm 10$  nm) are replicated by the magnetic nanoobject with high accuracy. The thick central segment corresponds to the mild anodization. The transition to the thinner section (hard anodization) is 100 nm wide. The samples prepared for magnetic characterization were protected by an extra 5-nm thick  $\text{SiO}_2$  layer deposited onto the alumina pore walls by atomic layer deposition (ALD) [BZC+08] before electrodeposition. This prevents the formation of an antiferromagnetic  $\text{NiO}$  layer at the surface of isolated wires. In fact, no significant difference has been observed between the hystereses from ensembles recorded for samples with and without the silica shell, even though the diameters are reduced by the  $\text{SiO}_2$  to 80 and 160 nm

( $\pm 10$  nm). The following measurements were done with samples including a silica sheath. In the next paragraphs 'hard' always means a diameter of 80 nm and 'mild' means a diameter of 160 nm. The diameters of all samples have always the same values for mild and hard.

## 5.2. Magnetic measurements

### 5.2.1. Properties of isolated nickel nanowires

First, the magnetic properties of an unmodulated and modulated wire as an isolated object are discussed — the interactions with neighbors will be considered in the next paragraph. In principle, a magnetic signature can be gleaned from a small amount of material using the magneto-optical Kerr effect (NanoMOKE<sup>TM2</sup>). To prepare samples for MOKE measurement, the nickel nanowires dissolved from the matrix and suspended in an ethanol solution are dripped onto a Si substrate. The Si substrate carries gold markers fabricated by e-beam lithography, for locating the wires unambiguously. Figure 4.10 shows the hysteresis of a single wire consisting only a hard segment (80 nm diameter): a MOKE signal is measurable when a beam of p-polarized light is collimated down to a diameter of 3  $\mu\text{m}$  on a flat Si substrate carrying individual Ni wires[Mar10]. The hysteresis curves recorded in a field applied parallel to the wire axis are averaged during the measurement (500 to 1000 times), in order to obtain a better signal to noise ratio. Figure 5.2 displays the data collected on a single wire consisting of a mild (160 nm diameter) and a hard segment (80 nm). Here, attention was paid to the fact that the laser spot contained one diameter modulation.

Figure 4.10 shows typical hysteresis of an unmodulated wire[Mar10]. The hysteresis loop is squared in shape, having a squareness close to 100 %. Figure 5.2 displays typical hysteresis recorded on individual Ni wires incorporating a change in diameter. Some of them yield two abrupt magnetization reversals on one branch of the hysteresis curve, highlighted in red color in the figure (sample C), while others give rise to the typically measured on unmodulated wires (sample E) (see figure 4.10). The presence of two distinct reversal events could originate in the pinning of the domain boundary at the diameter change. However, this curve shape may also arise from the addition of purely square individual hysteresis loops with two possible values of the switching field. Additionally, a symmetrical loop with two magnetization changes on both branches is never observed. Those contrasted observations make sense if it is considered that domain walls propagating from one extremity of a wire to the other may be pinned by more than one type of irregularity — not only diameter changes but also crystal defects, roughness, and even magnetic impurities possibly present on the silicon substrate. The diameter modulation from 80 to 160 nm within a width of 100 nm in the present wire may not be sufficient to cause pinning on its own in 100 % of the cases. From the theoretical point of view these one side jumps can come from the different regions covered by the laser spot, but a stochastic behavior of the reversal process is more probable, because the hysteresis loop consist of an average of

multiple single measurements. The height of the jumps ( if the signal intensity is always the same) indicates the probability for the resisting switching fields rather is proportional to the probability of the switching fields. In this example (figure 5.2) it will be clear that the switching fields are equally possible at 747 Oe and 662 Oe. So, a stochastic aspect comes into play, as has been amply documented in the case of wires fabricated by e-beam lithography[BML<sup>+</sup>08, MBE<sup>+</sup>07].

The depinning and pinning of domain walls can be influenced on the one hand, with different diameters of cylindrical nanowires[Her02] or rather diameter modulations as it was shown here. But on the other hand, local fields caused by e-beam lithography fabricated notches in 2D-nanowires e.g. can influence the pinning process[ORZ<sup>+</sup>09, HTM<sup>+</sup>08]. Another way to pin and depin domain walls is to use different material compositions in one nanostructure e.g. the transition between a hard and a soft magnetic material. This was simulated by Forster in 2002[FSS<sup>+</sup>02].

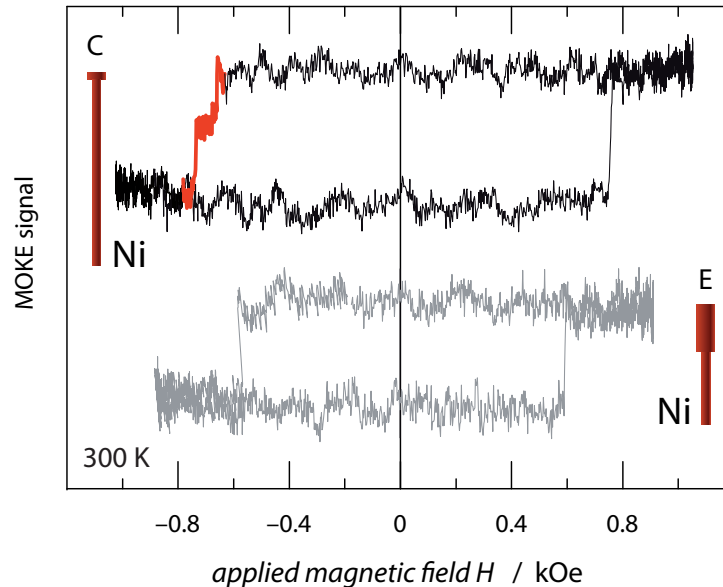


**Figure 5.2.:** Single-wire magneto-optical (MOKE) hysteresis loops of two different modulated wires. One of them display more than one reversal event whereas the second wire (gray) reverses in a single step.



Now, elementary theoretical models are used to calculate the coercive fields of modulated wires without taking domain wall pinning into account. The agreement with the experiment, or the lack thereof, can then be considered as an indication as to whether domain wall pinning plays a significant role or not. Based on the results of a published analytical model[LAE<sup>+</sup>07], it is considered that the magnetization reversal occurs by the propagation of a transverse (**T**) domain wall, in which a net magnetization component appears in the  $(x, y)$  plane (perpendicular to the wire axis). Contrary to the analytical results[LAE<sup>+</sup>07], numerical simulations have reached the conclusion that nickel wires of the diameter relevant here, but much shorter length should switch through a vortex: [WNU04, Her02, HN00]. This is also shown in a OOMMF simulation exemplified here for wire F in which the length is much shorter than experimentally investigated wire. More figures are given in the appendix (see figure B.4, figure B.5, figure B.6 and figure B.7).

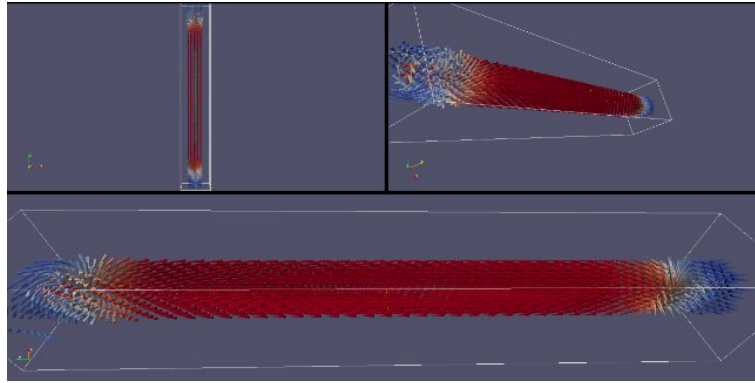


**Figure 5.3.:** Snapshot of the simulated spin configuration of wire F at an applied field done by OOMMF[Esc10].

Nevertheless, the **T** mode is used here given the very large aspect ratios of the experimentally investigated wires. More details can also be found in chapter 2.4. For any given radius  $R$  of the wire, the coercive field  $H_c^T$  can be calculated based on an analytical treatment[EBJ<sup>+</sup>08] in which the classical Stoner-Wohlfarth model[SW48] is adapted considering the width  $w_T$  of the domain wall,

$$\frac{H_c^T}{M_0} = \frac{2(K(l) - K_\alpha)}{\mu_0 M_0^2} \quad (5.1)$$

where  $K_\alpha = -1.6 \cdot 10^4 \text{ J m}^{-3}$  is the anisotropy constant[RFH<sup>+</sup>01, ELR<sup>+</sup>03],  $K(l) = \frac{1}{4} \mu_0 M_0^2 (1 - 3N_z(l))$  (with  $N_z(l)$  the demagnetization factor along  $z$ )[LEA<sup>+</sup>05],  $M_0 = 4.85 \cdot 10^5 \text{ A/m}$ , and  $A = 10^{-11} \text{ J m}^{-1}$ [O'H00]. The effective coercive field could be approximated as the volume weighted average of the two  $H_c$  values calculated with the two radii involved. The comparison of the  $H_c$  values obtained in this manner with the coercive fields determined experimentally (MOKE) shows that the measurement of more than one sample (measured many times) gives a systematic error. Figure 5.4 compares the values calculated in this manner (empty blue circles) with the experimentally determined switching fields (full blue disks). The agreement is acceptable for the wire types labeled E, C, and

F (one diameter change or none), given the complexity of the system and the crudity of the approximations. In contrast to this, the value calculated for sample A, which consists of three segments, is off the one experimental data point by a large difference. At this point, it will be postponed an interpretation of this phenomenon due to the questionable statistical significance of a single experimental measurement. The study of wire ensembles will in this respect yield more positive evidence.

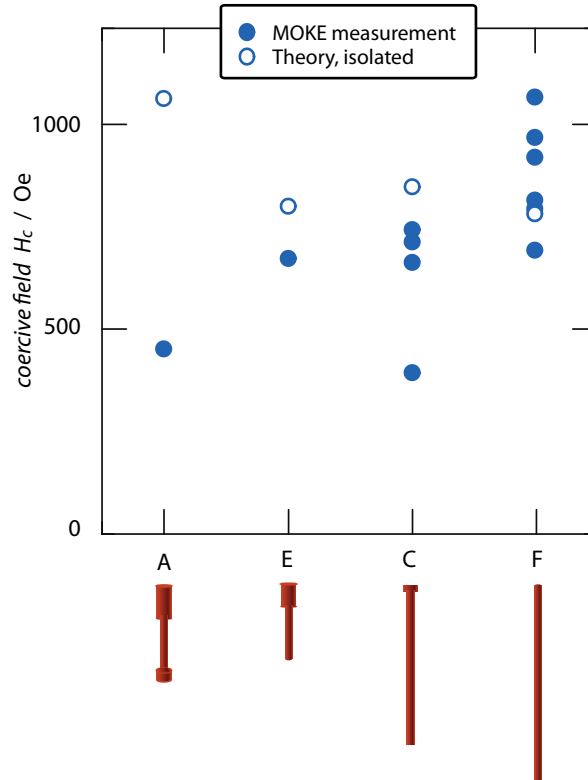


**Figure 5.4.:** Summary of the coercive fields measured (full symbols) and calculated (empty symbols) for various types of modulated wires as single objects (circles). From left to right the geometry is as sketched, anodization conditions (mild: 160 nm diameter, hard: 80 nm diameter): **A**, mild 8  $\mu\text{m}$ , hard 8  $\mu\text{m}$ , mild 1  $\mu\text{m}$ ; **E**, mild 5  $\mu\text{m}$ , hard 8  $\mu\text{m}$ ; **C**, mild 0.5  $\mu\text{m}$ , hard 20  $\mu\text{m}$ ; **F**, hard 20  $\mu\text{m}$ .

### 5.2.2. Influence of dipolar interactions in nickel wire ensembles

When the unmodulated and modulated nanowires are investigated as arrays, interactions with the neighbors come into play [KEC<sup>+</sup>05, KRE<sup>+</sup>05, NHVV<sup>+</sup>07]. Indeed, a hysteresis loop measured at 300 K (with  $\vec{H} \parallel \vec{z}$ ) on an ensemble of wires containing first only a long thin (hard: 80 nm diameter) segment (geometry F, square symbols of Figure 5.5 (a)) and second one short thick (mild: 160 nm diameter) section as well as a long thinner one (geometry E, square symbols of

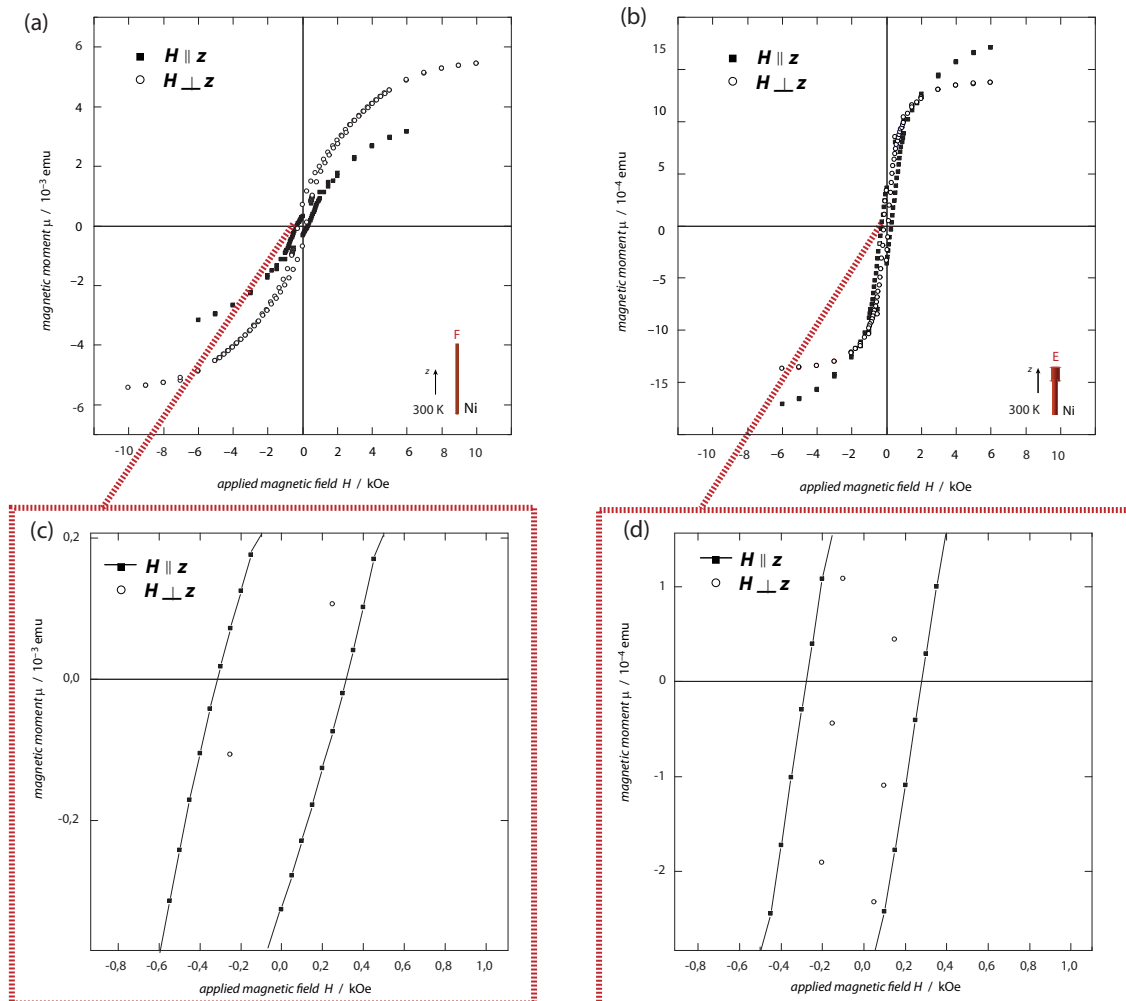


**Figure 5.5.:** (a) Magnetic hysteresis loops of an array of Ni wires (sample F) without any modulations (hard(80 nm diameter)  $20 \mu\text{m}$ ), oriented with the long axis ( $z$ ) parallel to the applied field (squares) and orthogonal to it (circles). (b) Sample E containing one modulation as sketched (mild(160 nm diameter)  $5 \mu\text{m}$ , hard(80 nm diameter)  $8 \mu\text{m}$ ), oriented with the long axis ( $z$ ) parallel to the applied field (squares) and orthogonal to it (circles). (c) and (d) magnification of the area around the coercive field for sample E and F.

Figure 5.5(b) is shown. (c) and (d) shows the magnification of the area around the coercive fields of the samples. The squareness (remnance 40 %) and coercive field (362 Oe) is reduced with respect to the single-object measurement for the same geometry (which yields 100 % squareness and 968 Oe coercive field). The modulated wire also shows a reduced squareness (remnance 45 %) and coercive field (260 Oe) with respect to the single-object measurement for the same geometry (which yields 100 % squareness and 670 Oe coercive field). If the two figures are closely compared the diameter variations have an influence on the coercive fields and the remnance. If one variation is included by putting the variation into consideration one would notice a lightly decrease or perhaps

drop in the values. Future discussions will later show that even more modulations play a vital role in the decrease of the coercive field. Here, it is clearly to see that the signal of sample F is also higher than of sample E, without the modulation there are more wires ordered parallel to each other in a smaller distance than in sample E. The dipolar interactions, however, do not fully obscure the characteristics of the wires, as can be observed when the SQUID measurement is repeated with  $\vec{H} \perp \vec{z}$  (circles). Due to the intrinsic shape anisotropy of the wires, the latter hysteresis yields even lower values of remanence and  $H_c$  (20 % and 82 Oe for the unmodulated wire and 8 % and 60 Oe for the modulated wire, respectively). This fact and the values of  $H_c$  are consistent with previous reports on Ni wires without modulations[NWB<sup>+</sup>01]. Figure 5.6 compares the SQUID

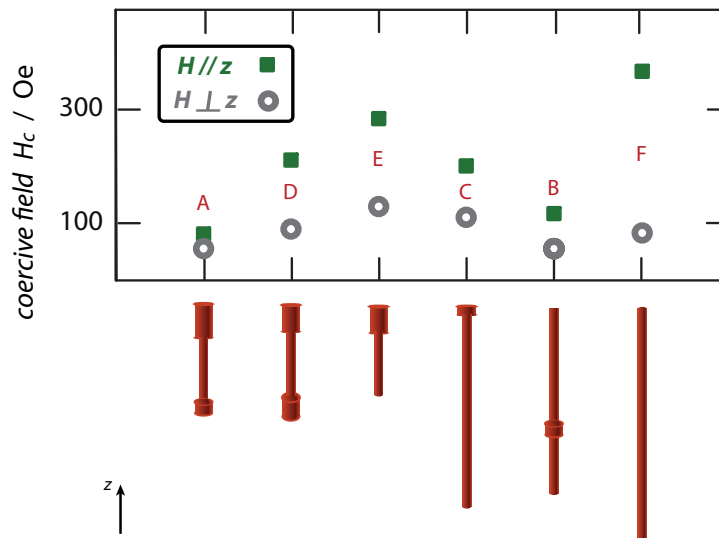


**Figure 5.6.:** Summary of the coercive fields measured (full symbols) and calculated (empty symbols) for various types of modulated wires as ensembles (squares). From left to right the geometry is as sketched, anodization conditions(mild: 160 nm diameter, hard: 80 nm diameter): **A**, mild 8  $\mu\text{m}$ , hard 8  $\mu\text{m}$ , mild 1  $\mu\text{m}$ ; **E**, mild 5  $\mu\text{m}$ , hard 8  $\mu\text{m}$ ; **C**, mild 0.5  $\mu\text{m}$ , hard 20  $\mu\text{m}$ ; **F**, hard 20  $\mu\text{m}$ .

hysteresis loops recorded on six samples of Ni wire arrays (labelled A-F) with different types of diameter modulations. The coercive field stays in the vicinity of 100 Oe for all wire geometries when the field is applied  $\vec{H} \perp \vec{z}$ . In  $\vec{H} \parallel \vec{z}$  orientation, however, differences emerge when the coercive field is considered as a function of the hard / mild ratio. Wires with smaller diameter have much larger values of  $H_c^{\parallel}$  than the wider ones. This is due to the more pronounced geometric anisotropy[[RGGV00](#), [RBZ+02](#), [ZYN+01](#)], as well as alleviated dipolar interactions between neighboring wires. More interestingly, one can observe that the introduction of one or two thick (mild) segments into a long narrow wire divides the coercive field value by a factor two or three. Clearly,  $\vec{H}_c$  is not simply the weighted average of values that could be calculated [[ELP+08](#), [EAJ+07](#)] for wires of 80 nm, on the one hand, and 160 nm, on the other hand. This could be considered

as an indication (albeit an indirect one) that the modulation serves as a nucleation point for the creation of domain walls and thereby facilitates the initiation of magnetization reversal. However, given the results presented in the previous paragraph, it is contended that this effect is controlled by dipolar couplings in the ensemble.

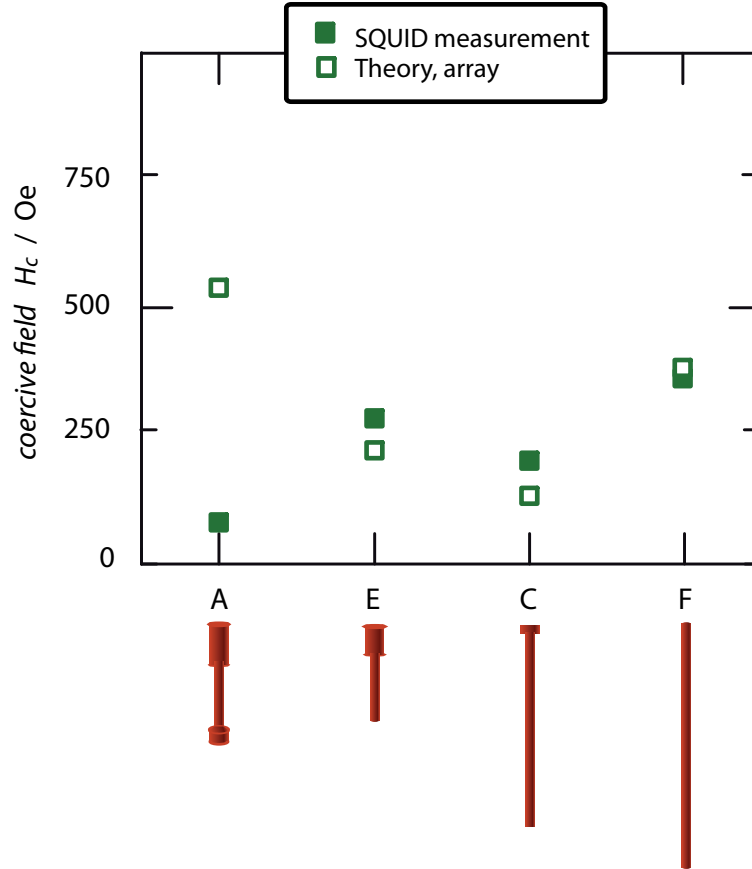
Indeed, the stray field generated by each wire is certainly strongly affected by the presence of modulations.

This aspect can be modeled: For this, the magnetostatic interaction between two modulated wires as the sum of the interactions between their individual segments can be considered, along the lines described more fully for the case of tubes[PMME<sup>+</sup>09]. In essence, the effective coercive field  $H_c$  in the array will be reduced from the value  $H_c^T$  calculated for an isolated object [Her01] by an amount  $H_{int}$  corresponding to the stray field[EAAB08]:

$$H_c = H_c^T - H_{int} \quad (5.2)$$

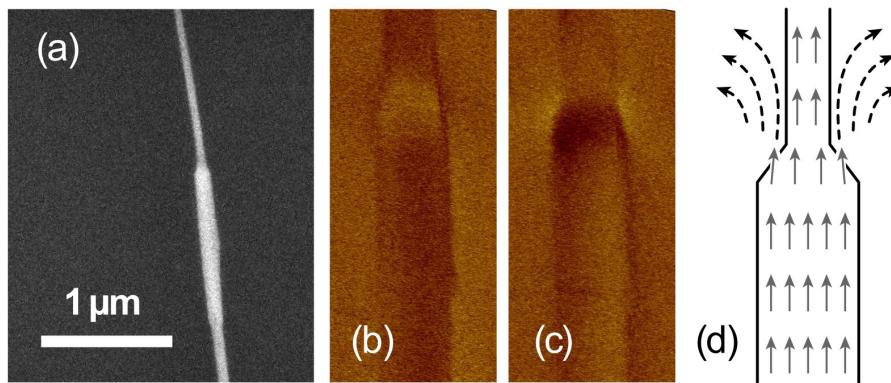
This lowering in  $H_c$  is, qualitatively speaking, due to the spatial inhomogeneity of the stray field in such arrays of quite densely packed magnets[Her01]. In a mean-field approximation, only the remanence and not the coercive field would be affected[FTW03]. Figure 5.7 compares the theoretical values obtained for  $H_c$  in the ensemble according to the approach of Escrig *et al.*[EAAB08] (empty squares) with those calculated for single objects (empty circles) and with the corresponding experimental data — measured with SQUID and MOKE magnetometry for the ensemble (full green squares) and isolated objects (full disks). The dipolar interactions cause a major reduction in  $H_c$  in each sample. This is observed and seen both in the experimental and theoretical sets of data. This observation substantiates the importance of the stray fields generated in the vicinity of each diameter modulation. Experimentally, stray fields can be imaged by magnetic force microscopy (MFM). It is used to obtain information of the magnetization structure of the sample. During a measurement the sample is scanned in a defined pattern with a magnetized sharp tip called cantilever. The interactions between tip and sample are detected and used to reconstruct the magnetic structure of the sample surface[Bon00]. Magnetic force microscopy was performed in a version of the Veeco DI Nanoscope IIIa built in a 1600 Oe magnet and operated with a cobalt-covered magnetic tip.

Figure 5.8 displays the MFM data recorded on one horizontally lying wire under a saturating field applied along  $+\vec{z}$  and  $-\vec{z}$  ((c) and (d)). A strong contrast is observed in the region with varying diameter, which is inverted when the applied field is reversed. Therefore, the contrast is magnetic in origin. However, the symmetry of the picture excludes its interpretation as originating from the presence of a domain boundary. Both a vortex and a transverse domain wall would introduce a difference in the perpendicular component of the stray field between the left and right sides of the wire, which is not observed in the MFM signal resulting in a different contrast[MSM<sup>+</sup>02, GTM02, BMT<sup>+</sup>98]. Thus, the contrast directly evidences the enhanced stray field present in the vicinity of the diameter modulation (sketched in Fig. 5.8 (d))



**Figure 5.7.:** Summary of the coercive fields measured (full symbols) and calculated (empty symbols) for various types of modulated wires as ensembles (squares). From left to right the geometry is as sketched, anodization conditions(mild: 160 nm diameter, hard: 80 nm diameter): **A**, mild 8  $\mu\text{m}$ , hard 8  $\mu\text{m}$ , mild 1  $\mu\text{m}$ ; **E**, mild 5  $\mu\text{m}$ , hard 8  $\mu\text{m}$ ; **C**, mild 0.5  $\mu\text{m}$ , hard 20  $\mu\text{m}$ ; **F**, hard 20  $\mu\text{m}$ .

The comparison of the theoretically calculated coercive fields with the experimentally determined fields in figure 5.4 and figure 5.6 indicates a good agreement for samples E, C, and F (equations 5.1 and 5.2). The experimental distribution of values at the single-object level reflects shape and size irregularities, which are averaged out in the ensemble and lead to an improved fit between theory and experiment. Among the factors that can account for the small differences are thermal fluctuations and the finite length of the wires. To conclude, therefore, the hypotheses on which the analytical model bases are satisfactory. Most significantly, it need not be assumed that domain wall pinning occurs in order to account for the data. The situation is different for sample A, which consists of



**Figure 5.8.:** Magnetic imaging of an isolated Ni wire. (a) Scanning electron microscopy furnishes the structural information. (b,c) Magnetic force micrographs of the central section of the wire taken in saturating positive and negative fields applied along the wire axis. The contrast originates from the magnetic stray fields generated by the ferromagnetic nanowire. Dark and bright areas reflect the presence of a magnetic field gradient perpendicular to the plane of the figure. (d) Sketch of the magnetization (gray arrows) within the wire and of the stray field lines (dashed black arrows) outside of it.

three segments. Here, the theoretical values differ from the measured counterparts by approximately 500 Oe both for an isolated object and the ensemble. The results of a similar investigation on modulated nanotubes are recalled, where structures with more than two thick (mild: 160 nm diameter) segments were not well described by the model, either [PMME<sup>+</sup>09]. This behavior is attributed to a novel phenomenon. In this case, the magnetization reversal might take place via a more complex mechanism in which the modulations play a particular role. Additionally, the shape of the domain boundaries may deviate from the idealized structure in the analytical model (equations 5.1 and 5.2). In thesis different materials and nanostructures were fabricated, so after presenting the results of the Ni wires by ED, nanotubes by ALD are presented. This suffers as a proof of concept and also to find a magnetic material which has promising magnetic properties for the depinning and pinning of domain walls.

## 6. Fe<sub>3</sub>O<sub>4</sub> nanotubes

### 6.1. Introduction

Fe<sub>3</sub>O<sub>4</sub> nanotubes with diameter modulations have been prepared to analyze the influence of these modulations on the pinning and depinning of domain walls. Nanotubes can either be realized by electrodeposition [XYS+03, CAS+11, HSS+09] or by ALD. From the literature it is clearly understood that nanotubes by electrodeposition are not comparably good with nanotubes by ALD. With ALD, conformal coating and material deposition over large areas is realisable. In this regard, Fe<sub>3</sub>O<sub>4</sub> nanotubes were prepared by ALD process. Their respective analysis as well as characterization by various experimental methods and theoretical assumptions give detailed information on the samples.

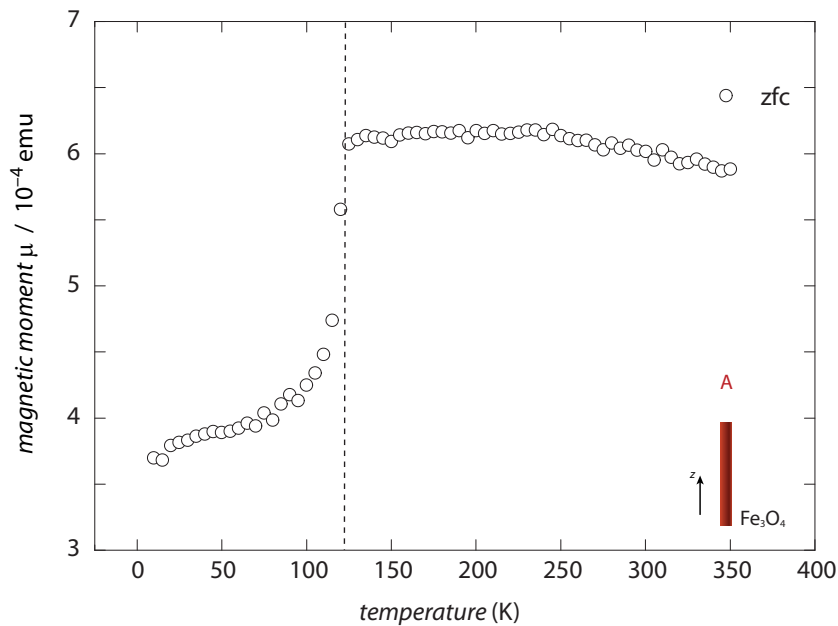


**Figure 6.1.:** The Verwey transition [Ren13] is mentioned at 120 K, here the temperature is fixed at 123 K for the iron III oxide nanotubes. The magnetization increases with the temperature and at its maximum it remains constant. The sample was measured in the zfc-mode (more details to this measuring method can be found in chapter 4.2.1)

There are several iron oxides phases and not all of these are ferromagnetic. These oxides can be measured by XRD to classify the magnetic properties. 1913 the



Verwey transition was measured at 120 K [Ren13], it can be used as an indicator for the ferromagnetic  $\text{Fe}_3\text{O}_4$  phase. The Verwey transition was firstly observed on magnetite crystals. There are still open questions in science: is the Verwey transition measurable in nanoparticles? Can defects in the crystal purity dominate the existence of the transition? In this case here, the Verwey transition seen in the samples let one affirm that the layers consist of  $\text{Fe}_3\text{O}_4$  magnetite. In figure 6.1 the Verwey transition is clearly illustrated. All samples shown here, were fabricated together in the same preparation process. This sample in figure 6.1 was measured in zfc-mode.

The Verwey transition appears at 120 K and here the temperature is fixed at 123 K. The magnetization increases with the temperature and at its maximum, it remains constant and at a certain maximal temperature the saturation is reduced. The samples are utilized from AAMs, and with ALD, a conformal coating of the pore walls is achieved. The porous alumina membranes made from alternating mild and hard anodization, yield modulations in the pore diameter. In the next paragraphs 'hard' always means a diameter of 70 nm and 'mild' means a diameter of 150 nm. The diameters of all samples have always the same values for mild and hard. In this way, large arrays of parallel objects ( $\approx 10^8$ ) are obtained with geometric parameters (length, width and number of modulations) defined at the experimentalist's discretion (find more details in chapter 3.1.2). A figure of all used samples in this chapter can be found in figure 3.9 (b).

Scanning electron microscopic investigation of the arrays shows the conformality of the deposition and the exact parallelism between the geometries of neighboring tubes.

Transmission electron micrographs display in figure 6.2 the multilayered structure of the isolated tubes, as well as clear transitions between the 70-nm wide 'hard' segments and their 150-nm wide 'mild' counterparts.

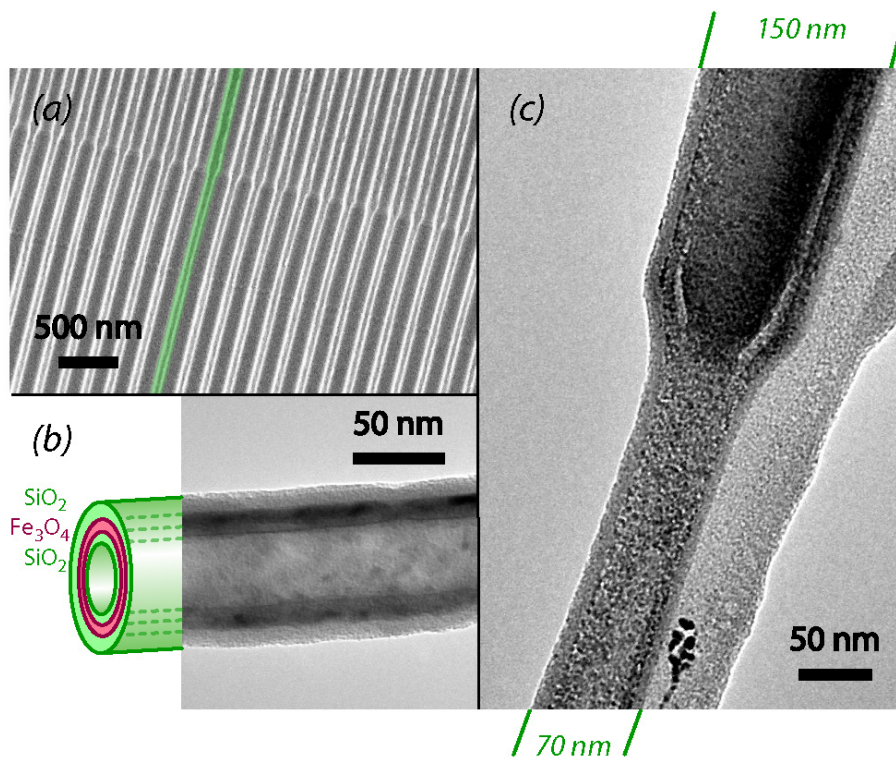


**Figure 6.2.:** Structures of the modulated iron III oxide nanotubes. (a) Scanning electron micrograph of a tube array embedded in the alumina matrix, displayed in section; the tubes' walls appear white on the the darker  $\text{Al}_2\text{O}_3$  background. (b) Transmission electron micrograph of a  $\text{Fe}_3\text{O}_4$  tube (after hydrogen reduction) protected by two thin silica layers. (c) TEM view of an isolated  $\text{SiO}_2/\text{Fe}_3\text{O}_4/\text{SiO}_2$  tube (layer thicknesses: 6 nm / 10 nm / 6 nm) near a transition between a narrow segment and a wide one. Its silhouette reflects that of the arrayed objects from (a).

## 6.2. Magnetic measurements and theoretical treatment

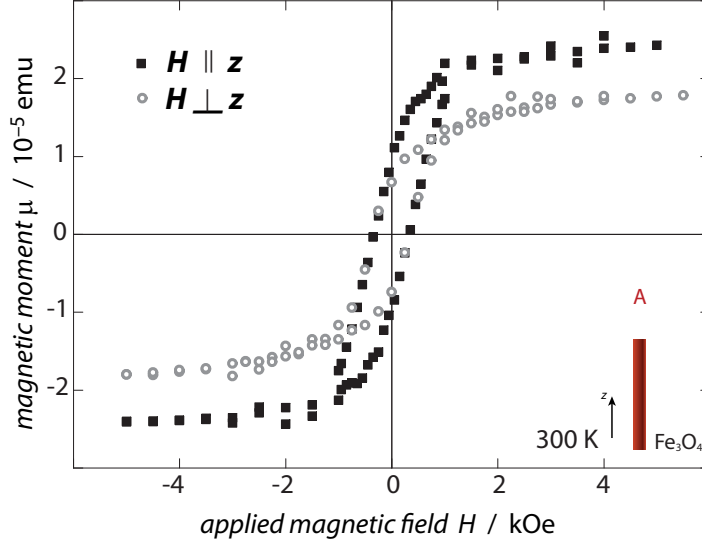


**Figure 6.3.:** Magnetic hysteresis loops of an array of  $\text{Fe}_3\text{O}_4$  nanotubes (10 nm wall thickness) in a field applied parallel or perpendicular to the long axis ( $z$  axis) of the tubes at 300 K. Both the coercive field  $H_c$  ( $x$  intercept) and the remanence  $\mu_{rem}$  ( $y$  intercept) are not significantly affected by the orientation of the sample ( $H_c^{\parallel} = 351$  Oe;  $H_c^{\perp} = 351$  Oe;  $\vec{H} \parallel \vec{z}$ ,  $\mu_{rem}^{\parallel} = 0.5 \mu_{sat}$ ;  $\mu_{rem}^{\perp} = 0.4 \mu_{sat}$ ). Anodization conditions of the template: mild(150 nm diameter) 15  $\mu\text{m}$ .

As ensembles, the nanotubes can be characterized in various orientations in respect to the applied field, as exemplified by the hysteresis loops of figure 6.3. The first shown sample consists only of one mild segment. When the sample is magnetized to saturation in a magnetic field  $H = 5$  kOe applied along the long axis of the tubes,  $\vec{H} \parallel \vec{z}$ , and the field is then turned off, 50 % of the saturated magnetization is retained (remanence,  $\mu_{rem}^{\parallel} = 0.5 \mu_{sat}$ ). In a perpendicularly applied field,  $\vec{H} \perp \vec{z}$ , the same experiment yields a remanence  $\mu_{rem}^{\perp} = 0.4 \mu_{sat}$ . Both the coercive field  $H_c$  and the remanence  $\mu_{rem}$  are not significantly affected by the orientation of the sample ( $H_c^{\parallel} = 351$  Oe;  $H_c^{\perp} = 351$  Oe;  $\vec{H} \perp \vec{z}$ ,  $\mu_{rem}^{\parallel} = 0.5 \mu_{sat}$ ;  $\mu_{rem}^{\perp} = 0.4 \mu_{sat}$ ). Next a sample with a long hard (70 nm diameter) and a short mild segment (150 nm diameter) is introduced. Now, the effect of the shape anisotropy and diameter modulations come into play. When the second sample (see figure 6.4) is magnetized to saturation in a magnetic field  $H = 6$  kOe applied along the long axis of the tubes,  $\vec{H} \parallel \vec{z}$ , and the field is then turned off, 90 % of the saturated magnetization is retained (remanence,  $\mu_{rem}^{\parallel} = 0.9 \mu_{sat}$ ). In a perpendicularly applied field,  $\vec{H} \perp \vec{z}$ , the same experiment yields a remanence  $\mu_{rem}^{\perp} = 0.4 \mu_{sat}$ . The large difference between  $\mu_{rem}^{\parallel}$  and  $\mu_{rem}^{\perp}$  defines  $z$  as the 'easy' axis of the sample, as expected from the strong shape anisotropy.

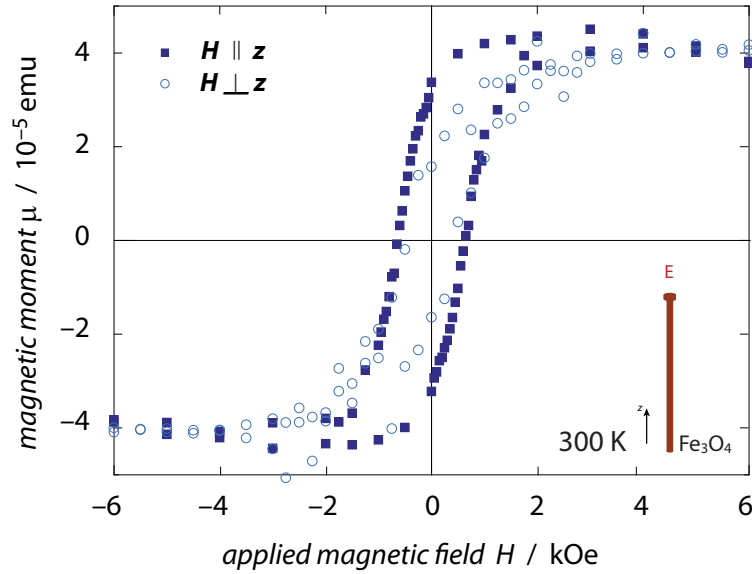


**Figure 6.4.:** Magnetic hysteresis loops of an array of  $\text{Fe}_3\text{O}_4$  nanotubes (10 nm wall thickness) in a field applied parallel or perpendicular to the long axis ( $z$  axis) of the tubes at 300 K. Both the coercive field  $H_c$  and the remanence  $\mu_{rem}$  are strongly affected by the orientation of the sample ( $H_c^{\parallel} = 660$  Oe;  $H_c^{\perp} = 480$  Oe;  $\vec{H} \perp \vec{z}$ :  $\mu_{rem}^{\parallel} = 0.9 \mu_{sat}$ ;  $\mu_{rem}^{\perp} = 0.4 \mu_{sat}$ ). Anodization conditions of the template (mild: 150 nm diameter, hard: 70 nm diameter): mild  $0.5 \mu\text{m}$ , hard  $20 \mu\text{m}$ .

Accordingly, the effects of the diameter modulations can clearly be observed by the same method. 6.5 summarizes the results of SQUID magnetic hysteresis loops recorded on five samples of  $\text{Fe}_3\text{O}_4$  nanotube arrays with different types of diameter modulations (as shown in the sketch of figure 6.5). The coercive field is almost unaffected by the geometry of the tubes when the field is applied  $\vec{H} \perp \vec{z}$ . In the  $\vec{H} \parallel \vec{z}$  orientation, however, a trend emerges when the coercive fields are considered as a function of the hard / mild ratio. Tubes with smaller diameter have much larger values of  $H_c^{\parallel}$  than the wider ones. This is due to the more pronounced shape anisotropy, as well as alleviated dipolar interactions between neighboring tubes [EBJ+08].

More interestingly, comparison between the last two samples (D and E on the right of figure 6.5) reveals that the introduction of a single short wide segment in the middle of a long narrow tube causes a drop in coercive field by more than 30 %. This is a token that the diameter modulations influence the magnetic reversal phenomena beyond the linear regime.

This suspicion is corroborated by simple models of the magnetization reversal (all theoretical details can be found following paragraphs). Of the three conceivable mechanisms for the reversal of the magnetization from the  $+z$  direction to  $-z$  (the coherent rotation, the vortex and the transverse mode) the vortex prevails for all geometries considered here (figure 6.7). In the vortex mode,

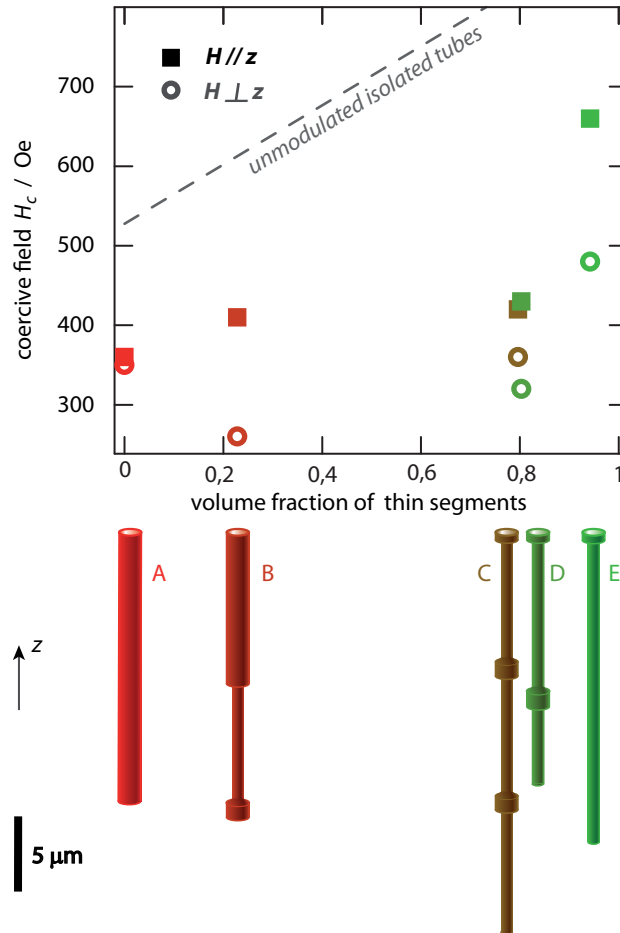


**Figure 6.5.:** Comparison of the coercive fields  $H_c$  of different types of modulated  $\text{Fe}_3\text{O}_4$  tubes (as arrays). The experimental data points show a strong effect of geometry on  $H_c$  when the field is applied parallel to the long axis (full squares), and a near independence of  $H_c$  upon geometry for the orthogonal orientation (empty circles). The gray line corresponds to coercive fields calculated for unmodulated isolated objects as an interpolation between the values of thin and thick tubes. The  $x$  axis quantifies the volume fraction of magnetic material in the thin segment (from 0 to 1). Anodization parameters of the template (mild: 150 nm diameter, hard: 70 nm diameter): (A) mild 15  $\mu\text{m}$ ; (B) mild 10  $\mu\text{m}$ , hard 8  $\mu\text{m}$ , mild 1  $\mu\text{m}$ ; (C) mild 0.5  $\mu\text{m}$ , hard 8  $\mu\text{m}$ , mild 1  $\mu\text{m}$ , hard 8  $\mu\text{m}$ , mild 1  $\mu\text{m}$ , hard 8  $\mu\text{m}$ ; (D) mild 0.5  $\mu\text{m}$ , hard 10  $\mu\text{m}$ , mild 1  $\mu\text{m}$ , hard 5  $\mu\text{m}$ ; (E) mild 0.5  $\mu\text{m}$ , hard 20  $\mu\text{m}$ . (c) Schematic of the five geometries considered.

the calculated coercive field is larger for the thinner ('hard') diameter than the thicker ('mild') one. Considering a linear relationship between  $H_c$  and the relative amounts of thick and thin segments yields the gray line of figure 6.5. Although the general trend obtained in this way corresponds to the observations for samples A, B and E, the two samples with short thick segments built in the middle of the tube clearly show the limits of such a simple linear treatment. The deviations are ascribed from it to the interaction of each tube with the stray field produced by its neighbors, which reduces the coercive field. The stray field of a simple tube is most intense at its extremities — in a modulated tube, the presence of additional non-vertical surfaces (surfaces which are orthogonal to the magnetization), strongly reinforces the stray field at the modulations. This is shown in figure 6.6 (a) for the example of geometry D, and for all geometries in figure 6.8. Accordingly, the dipolar interaction between neighboring tubes is significantly increased by the introduction of diameter modulations, even very short ones (table 6.1). This is the reason why geometries such as C and D, with a small volume fraction of thick tube, strongly deviate from the simple linear interpolation. When the coercive field lowering caused by the stray field is taken into account, the calculated values correspond to the experimental measurements much better (figure 6.6 (b)). The difference between calculated and measured values can originate from structural imperfections of the tubes prepared here, in particular the fact that the transition between thick and thin segments is not perfectly abrupt.

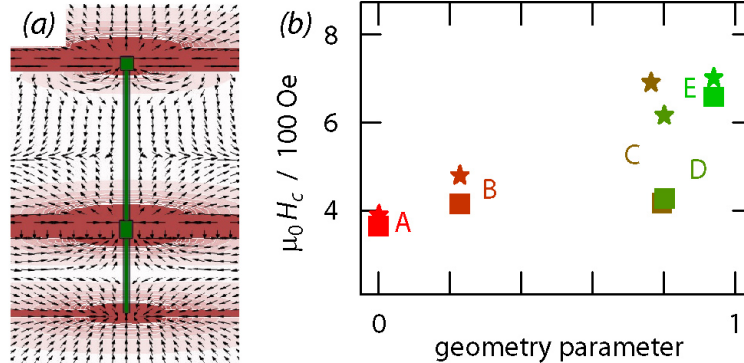


**Figure 6.6.:** Theoretical modeling of the modulated magnetic tube arrays. (a) Stray field direction (arrows) and intensity (levels of red) generated by a modulated tube magnetized in the  $+z$  direction, as exemplified for structure D. (b) Coercive fields calculated for the different types of tubes, taking into account the strength of the dipolar interactions between neighboring tubes. The theoretical values (stars) are compared with the measured ones (squares). Labels A to E refer to the geometries described in 6.5, and the geometry parameter equals the volume fraction of thin segments in aspect to the total volume.

For isolated magnetic nanotubes, the magnetization reversal, that is, the change of the magnetization from one of its energy minima ( $\vec{M} = M_0 \hat{z}$ ) to the other ( $\vec{M} = -M_0 \hat{z}$ ), can occur by one of only three idealized mechanisms: The coherent

rotation (C), where all the spins (local magnetic moments) rotate simultaneously; the Vortex mode (V), whereby spins in rotation remain tangent to the tube wall; and the Transverse mode (T), in which a net magnetization component in the  $(x, y)$  plane appears [LAE<sup>+</sup>07]. This has been already discussed in chapter 2.4. The coherent rotation does not occur in the tubes prepared here in this thesis, so it will no longer be considered. Figure 2.17 illustrates the coercive field of an isolated tube of radius  $R$  varying from 15 to 80 nm. With the equations 2.15 and 2.16 and the following parameters for the  $\text{Fe}_3\text{O}_4$  nanotubes the coercive fields for different reversal modes have been calculated:  $M_0 = 4.8 \times 10^5$  A/m,  $A = 10^{-11}$  J/m and  $K = -11 \times 10^3$  J/m<sup>3</sup> [O'H00]. The exchange length for iron III oxide is here  $l_{\text{ex}} = 8.311 \times 10^{-9}$  m [O'H00].

A crossing of the dashed red and pointed blue curves at  $R_c = 22$  nm approximately is observed, corresponding to a magnetization reversal for which both T and V mechanisms are possible at the same coercive field. At other given values of  $R$ , Escrig and co-workers showed that the system will reverse its magnetization by whichever mode opens an energetically accessible route first [EBJ<sup>+</sup>08], that is, by the mode that offers the lowest coercivity. Thus,  $\text{Fe}_3\text{O}_4$  tubes will reverse their magnetization by the T mode for  $R < 22$  nm, and by the V mode for  $R > 22$  nm. In order to simulate the nanotubes with modulated diameters, the coercive field for two different nanotubes with a tube thickness of 10 nm, one with a radius  $R_1$  ranging between 30 and 40 nm ( $H_c = 1109$  and 784 Oe, respectively) and the other with a radius  $R_2$  ranging between 70 and 80 nm ( $H_c = 545$  and 521 Oe, respectively) is simply considered. Thus, the coercivity for the modulated nanotube as a weighted average between the values obtained for the thick and thin tubes is attended. Figure 6.7 illustrates the coercive field of the tubes as a function of the length fraction of thin segments. The calculations confirm the increase of the field as a function of the length fraction of thin segments experimentally observed. However, the absolute values computed for the coercivity are higher than the experimental data. Such difference between calculations and experimental results are ascribed to the interaction of each tube with the magnetostatic field produced by the array, which reduces the coercive field. In order to treat this aspect, the modulated tubes as composed of different segments of tubes are considered. Thus, the magnetostatic interaction between two modulated tubes as the sum of the interactions between their segments is calculated. The magnetostatic interaction between two different segments of tubes can be calculated from [Aha96]

$$E_{\text{int}} = -\mu_0 \int \vec{M}_j(\vec{r}) \cdot \vec{H}_i(\vec{r}) d\nu, \quad (6.1)$$

where  $\vec{M}_j(\vec{r})$  is the magnetization of the segment  $j$  and  $\vec{H}_i(\vec{r})$  is the magnetostatic potential of the segment  $i$ . The expression for the magnetostatic field has been previously reported [EAAB08, EAA<sup>+</sup>09], and is given by

$$\vec{H}_{i(r,z)} = \vec{H}_{ir}(r, z)\hat{r} + \vec{H}_{iz}(r, z)\hat{z}, \quad (6.2)$$

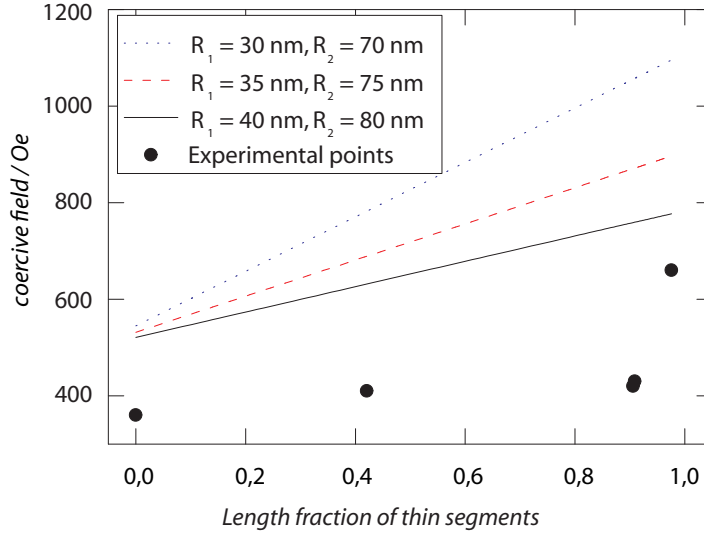


**Figure 6.7.:** Coercive fields of a modulated tube as a function of the length fraction of thin segments. Black dots correspond to those measured experimentally. Blue, red and black lines correspond to those calculated for different thinner and thicker tubes. Thickness of tube wall,  $d_w = 10$  nm.

where

$$\vec{H}_{i(r,z)} = \frac{M_0}{2} \int_0^\infty dk (R_i J_1(kR_i) - a_i J_1(ka_i)) - a_i J_i(kr) \left( e^{-k|\frac{L_i}{2}-z|} - e^{-k|-\frac{L_i}{2}-z|} \right), \quad (6.3)$$

and

$$H_{iz}(r, z) = \frac{M_0}{2} \int_0^\infty dk (R_i J_1(kR_i) - a_i J_1(ka_i)) J_0(kr) \times A \quad (6.4)$$

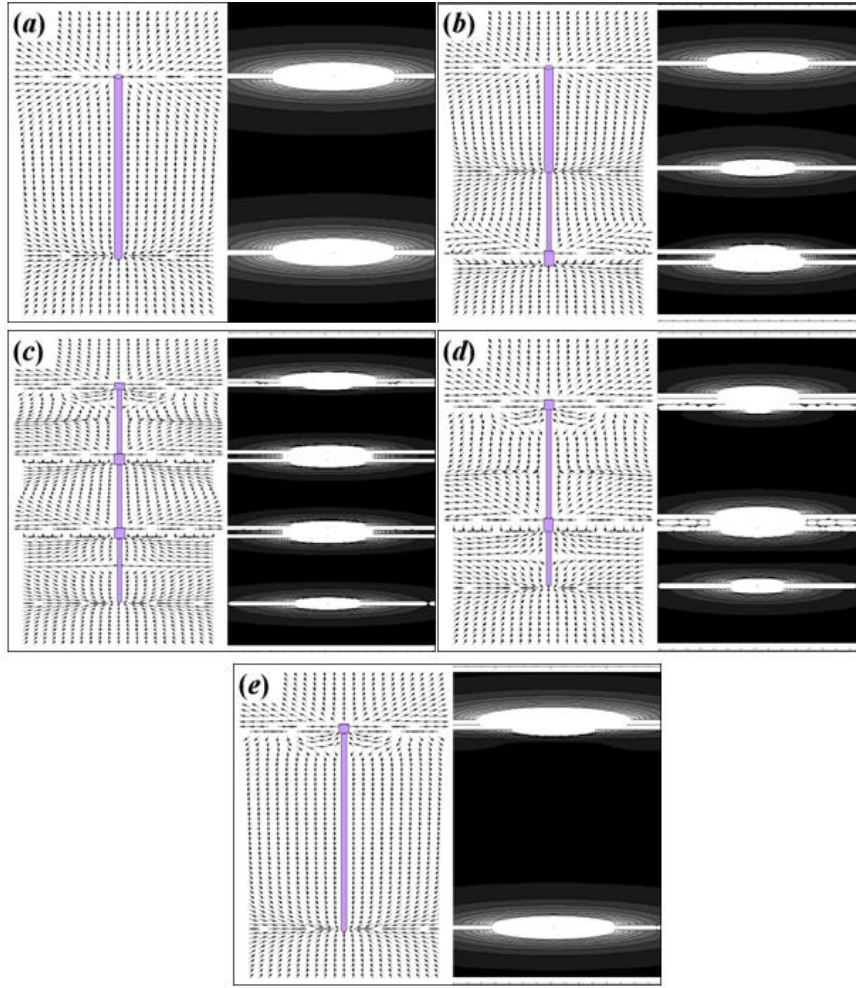
$$A = \left( \text{sgn} \left( \frac{L_i}{2} - z \right) e^{-k|\frac{L_i}{2}-z|} - \text{sgn} \left( -\frac{L_i}{2} - z \right) e^{-k|-\frac{L_i}{2}-z|} \right) \quad (6.5)$$

This field corresponds to the magnetostatic field of a segment of the modulated tube. Thus, the total magnetostatic field for the modulated tube is calculated, the contribution to the field of each segment has to be summed up. Figure 6.8 illustrates the magnetostatic field profile and the intensity of the field for the modulated nanotubes. Now, if it is considered that the separation between the segments is written in terms of the interaxial distance,  $d$ , and the vertical separation,  $s$ , as depicted in figure 6.9, then the magnetostatic interaction between two arbitrary segments is given by

$$E_{int}^{ij}(d, s) = -\pi\mu_0 M_0^2 \int_0^\infty \frac{dk}{k^2} B \cdot J_0(kd) (R_i J_1(kR_i) - a_i J_1(ka_i)) \quad (6.6)$$

$$B = e^{-\frac{k}{2}(L_i+L_j+2s)} (R_j J_1(kR_j) - a_j J_1(ka_j)) \quad (6.7)$$



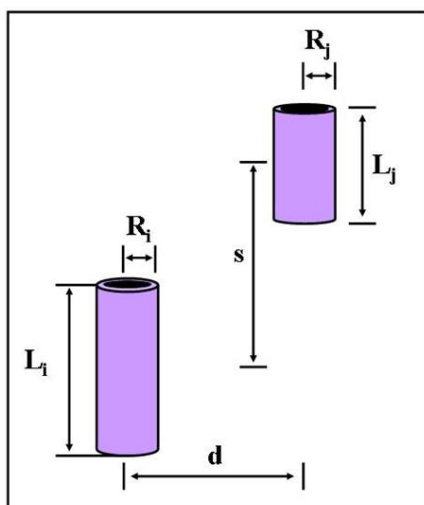


**Figure 6.8.:** Magnetostatic field profile and intensity of the field for tubes uniformly magnetized and geometries *A* to *E* as defined in figure 6.5. The color scale is chosen such that higher absolute values of the field are represented by lighter shades.

$$= \begin{cases} (1-e^{kL_i})(1-e^{kL_j}) & s \geq \frac{L_i+L_j}{2} \\ (1-e^{kL_i}-e^{kL_j}+e^{2ks}) & s \leq \frac{L_i+L_j}{2} \end{cases} \quad (6.8)$$






Equation (6.1-6.5) has been previously obtained for identical nanotubes [EAAB08].

It is easy to understand that the magnetostatic interaction between two modulated nanotubes will depend on their geometries (in this case on the type of modulated tube). Table 6.1 presents the magnetostatic interaction between two modulated nanotubes normalized to the interaction between the thicker ones (case A). Thus, it is observed that for a few cases this ratio is smaller than 1, which could be expected. However, a new phenomenon appears with the modulated tubes: because they have a lot of perpendicular surfaces to the magnetization vector, their interaction can be stronger than the interaction between two thick tubes.



**Figure 6.9.:** Relative position of interacting segments  $i$  and  $j$  of the modulated nanotube:  $d$  is the interaxial distance and  $s$  is the vertical separation.

This can be understood if it is considered that the stray field is intense in those surfaces that are perpendicular to the magnetization vector (see figure 6.8). So, it does not matter whether the modulated tubes have thin segments because the important feature here is those perpendicular surfaces.

Tube type	Interaction energy / Volume $E_{int}^{ij}(d, =)$	normalized $E_{int}$
A 	$5,42 \times 10^{-5}$	(1)
B 	$1,20 \times 10^{-4}$	1.14
C 	$8,56 \times 10^{-5}$	1.34
D 	$1,80 \times 10^{-5}$	1.06
E 	$1,05 \times 10^{-5}$	0.63

**Table 6.1.:** Comparison of the magnetostatic interaction energies  $E_{int}$  calculated from equation 6.10 for different types of nanotube arrays. The values are then normalized to the amount of magnetic material and reported with respect to case A. Thin tubes (E) interact with their neighbors less strongly than thicker ones (A); additionally, the presence of short thick segments (C, D) introduces major increases in the 305 interaction due to the non-vertical surfaces at the diameter modulations. The geometries A-E are as defined in figure 3.9 (b).

Thus, for an array of modulated tubes all of which are initially magnetized in the same direction, the magnetostatic interaction between neighboring tubes results in the magnetization reversal of some of the tubes. Then the macroscopic coercivity will be

$$H_C = H_C^i - H_{int}, \quad (6.9)$$

where  $H_C^i$  denotes the intrinsic coercivity  $H_C^C$ ,  $H_C^T$  or  $H_C^V$  of an isolated tube, and  $H_{int}$  corresponds to the stray field induced within the array. Escrig *et al.* have calculated this stray field for an array of simple cylindrical tubes given by

$$H_{int} = \frac{2K(L)}{\mu_0 M_0^2} \left( \frac{\epsilon \left| \tilde{E}_{int}^{ii}(d, 0) \right|}{K(L)} \right)^{\frac{1}{2}}. \quad (6.10)$$

Besides,  $\tilde{E}_{int}^{ii}(d, 0) = E_{int}^{ii}(d, 0)/\mu_0 M_0^2 V$  is the magnetostatic interaction between two identical nanotubes separated by an interaxis distance  $d$ . Using equation (6.2)

we have calculated the stray field  $H_{int}$  for the array of nanotubes of type A (see Figure 6.8 (c)). One should remember that the interaction energy for each modulated tube was normalized to the interaction energy of this system (case A). Thus, in order to calculate the stray field for arrays with more complex tubes (the modulated ones), it is simply considered that the stray field follows the same proportion as the interaction energy. As an illustration, when the system E is esteemed that the interaction energy will be around 0.6 times the interaction energy of the system A. Thus, it is expected that the total stray field induced inside the array E will be 0.6 times smaller than that calculated for the system A. The stray fields produced by an array of modulated nanotubes are significant for the experimentally investigated tubes, being on the order of 185 Oe for the system E to 415 Oe for the system B.

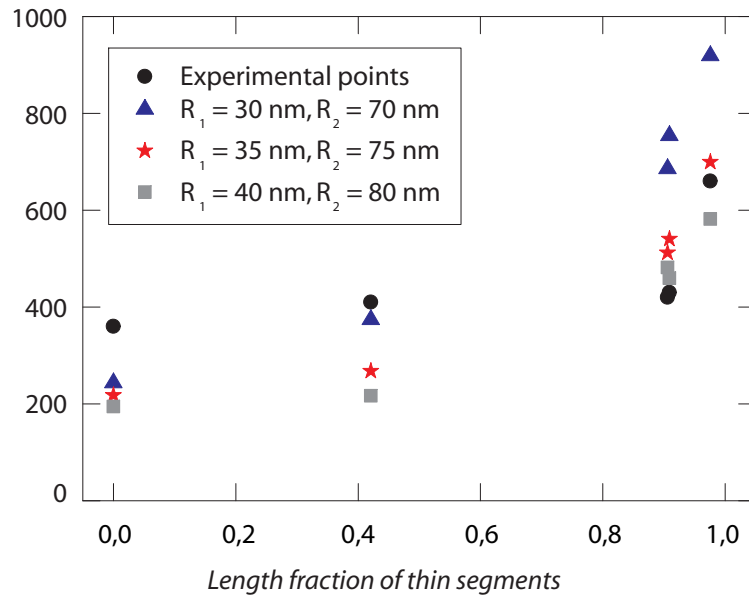


**Figure 6.10.:** Coercive field as a function of the length fraction of thin segments for modulated  $\text{Fe}_3\text{O}_4$  nanotubes. Blue triangles, red stars and gray squares correspond to those calculated for different thinner and thicker tubes. Parameters:  $D = 235 \text{ nm}$  and  $d_w = 10 \text{ nm}$ .

Figure 6.10 illustrates the coercive field of interacting arrays of modulated tubes as a function of the length fraction of thin segments. The calculations reproduce the unexpected behavior of the coercive field as a function of the length fraction of thin segments experimentally observed. It is observed that the system defined by  $R_1 = 35 \text{ nm}$  and  $R_2 = 75 \text{ nm}$  provides the best agreement with the measurements (see figure 6.6 (b)).

For  $\text{Fe}_3\text{O}_4$  nanotubes with a crystalline anisotropy from about

$K = -0.9 \times 10^4 \frac{J}{m^3}$  [O'H01] it is possible to see the influence of diameter modulations. But from recent measurements [KKM<sup>+</sup>11], it is clear that for future single-object studies with nanotubes also other material should be implemented with a lower crystalline anisotropy. The next chapter presents a new ALD process and also suffers as a proof of concept. First, the fabrication of Ni as a preparatory work before nickel/ cobalt is put forward.

# 7. Ni and NiCo nanotubes

## 7.1. Ni nanotubes

### 7.1.1. Introduction

In the previous chapter, the analysis and characterization of  $\text{Fe}_3\text{O}_4$  nanotubes with diameter modulations was presented. As a result from the observations, it was considered that also other interesting materials should be implemented and as well tested for future studies in controlling the pinning and depinning of domain walls. Materials such as permalloy, an alloy of 80 % nickel and 20 % iron, have a small crystalline anisotropy ( $K = -3 \times 10^2 \frac{\text{J}}{\text{m}^3} [\text{O'H01}]$ ). However, permalloy is really challenging to prepare by the ALD process. Hence, in this chapter the preparation and analysis of nickel/ cobalt is put forward. In the beginning of the synthesis process only nickel was implemented, afterwards the fabrication and analysis of nickel/ cobalt is shown. Nickel tubes fabricated by ALD are presented in this section. The geometry of these nanotubes is the main interesting aspect when comparing these with the described nickelwires or iron III oxide nanotubes. The template is prepared in the same method as mentioned earlier(s. chapter 3.1.2).

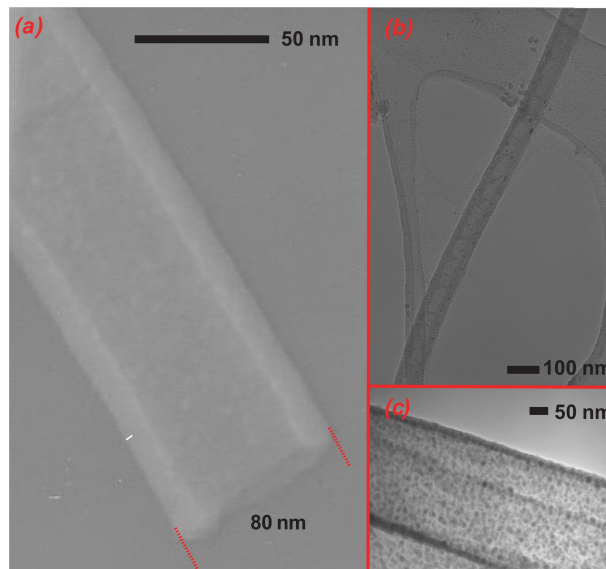


**Figure 7.1.:** (a) Transmission electron micrograph of an isolated  $\text{SiO}_2/\text{NiO}/\text{SiO}_2$  tube (layer thicknesses: 4 nm / 10 nm / 4 nm), the diameters of the pores are 80 or 160 nm, the length of the tubes is 10  $\mu\text{m}$ . (b) is an overview showing the homogeneous growth, (c) layerstack with granular structure.

The ALD processes of nickel as candidate is well known from different authors,

this process reclines on the nickel oxide process with the precursors nickelocene and ozone [DKGN07] (process parameters can be found in table A.3). Here, nickelocene and ozone are the two used precursors during the ALD process, the reduction from nickel oxide to nickel is realized in a Ar/H<sub>2</sub> atmosphere at 300°C for 3 hours. The nickeltubes are enclosed with a SiO<sub>2</sub> layer, to prevent the oxidation of the nickel in air. By varying this outer shell, Ni-shell with diameters of 150 nm (called: mild) to 70 nm (called: hard) can be achieved. Figure 7.1 displays thin nickel tubes in transmission electron micrographs. Figure 7.1 a) shows an isolated SiO<sub>2</sub>/ NiO / SiO<sub>2</sub> tube (layer thicknesses: 4 nm / 10 nm / 4 nm), the diameters of the pores are 80 or 160 nm, the length of the tubes is 10 μm. (b) is an overview showing the homogeneous growth, (c) layerstack with granular structure. The tubes are though homogeneously prepared, but in the magnification the grains of nickel particles can clearly be seen.

### 7.1.2. Magnetic measurements

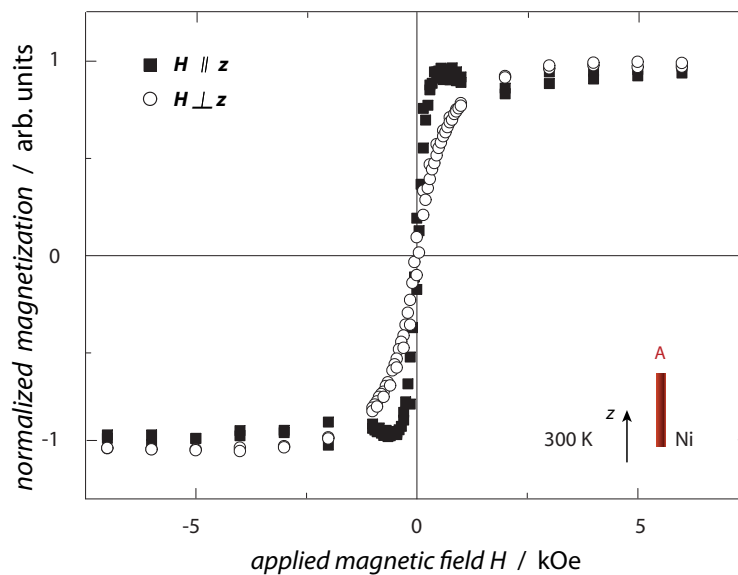


**Figure 7.2.:** Magnetic hysteresis loops of an array of Ni nanotubes (10 nm wall thickness) in a field applied parallel and perpendicular to the long axis ( $z$  axis) of the tubes at 300 K. The coercive field  $H_c$  ( $x$  intercept) and the remanence  $\mu_{rem}$  ( $y$  intercept) are not significantly affected by the orientation of the sample ( $H_c^{\parallel} = 50$  Oe ;  $\mu_{rem}^{\parallel} = 0.25 \mu_{sat}$  and  $H_c^{\perp} = 50$  Oe ;  $\mu_{rem}^{\perp} = 0.2 \mu_{sat}$ ). Anodization conditions of the template: mild 15 μm. At 300 K the coercive fields are very small. The values of the magnetization are normalized to the saturated magnetization.

Three samples with different geometrical parameters are presented. The samples are illustrated in figure 3.9 (c1). The nickeltubes are analyzed by ensemble measurements. Therefore, the magnetic measurements are recorded using a SQUID magnetometer (SQUID MPMS2 by Quantum Design). Figure 7.3 shows a typical hysteresis loop for these nickeltubes at room temperature with the orientation tubes parallel and perpendicular to the applied field. The geometry of the sample is shown in the figure.

There is a very small coercive field observable in both directions ( $H_c^{\parallel} = 50$  Oe and  $H_c^{\perp} = 50$  Oe), also the remanence is very small ( $\mu_{rem}^{\parallel} = 0.25 \mu_{sat}$  and  $\mu_{rem}^{\perp} = 0.2 \mu_{sat}$ ). The parallel configuration shows a slightly bigger remanence and is more squared in shape. These nanotubes consist of nanoparticles and behave superparamagnetically. The hysteresis at 5 K shows no shape anisotropy between the different orientations with respect to the applied field. The other two samples were as well measured at 5 K, also no differences between the orientations with respect to the applied field are seen (see figure B.1 and figure B.2). The different geometrical parameters of the samples do not come into play, the superparamagnetic effect of the particles dominates over the shape anisotropy.

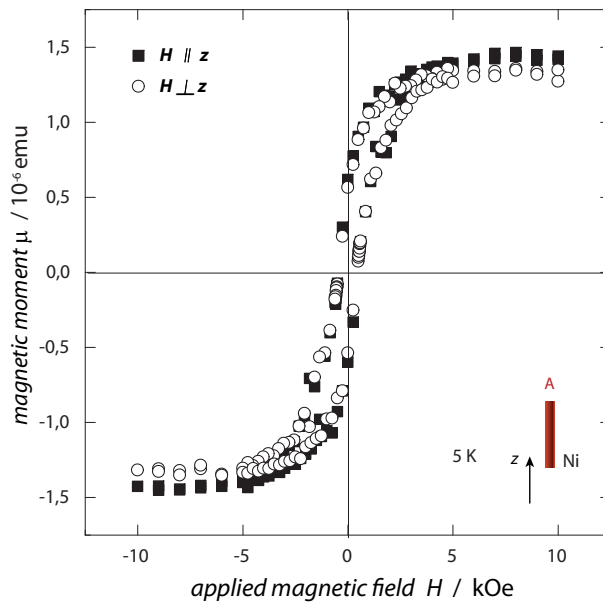


**Figure 7.3.:** The ensemble is measured at 5 K: Here the various orientations with respect to the applied field are shown. Both the coercive field ( $H_c^{\parallel} = 430$  Oe;  $H_c^{\perp} = 400$  Oe) have the same values with respect to the applied field, also the remanence ( $\mu_{rem}^{\parallel} = 0.7 \mu_{sat}$ ;  $\mu_{rem}^{\perp} = 0.7 \mu_{sat}$ ) is the same: no shape anisotropy can be observed.

Figure 7.4 shows two temperature dependent measurements in a curve of nickel tubes with a diameter of 70 nm and a length of 20  $\mu\text{m}$ . The sample is cooled at a zero magnetic field, then during the zero field cooling measurement, the sample is warmed up at a small applied magnetic field. The induced magnetization is



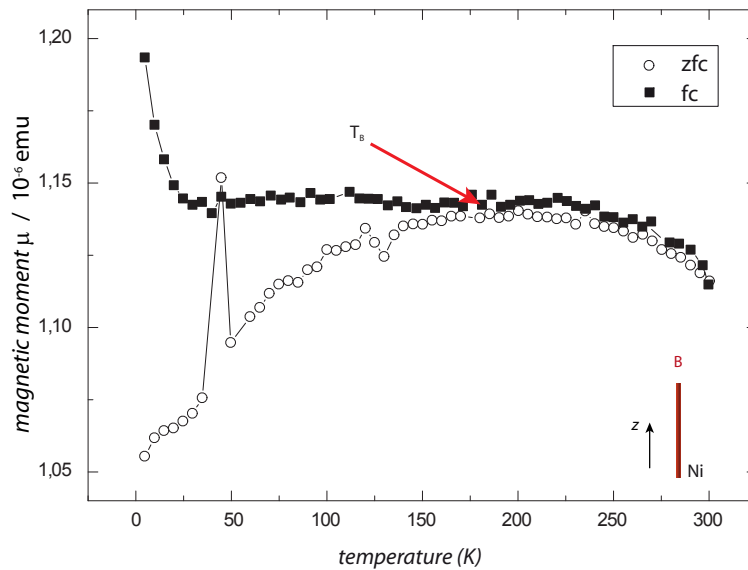


**Figure 7.4.:** The curve illustrates the two procedures of measuring the temperature-dependent magnetization: zero field cooling and field cooling. Shown is a sample of nickel nanotubes which behave superparamagnetic, defined by the characteristic  $T_B$ , the zfc and fc curve. The measurement was done at an applied field of 100 Oe. The outlier data point at 47 K comes from oxygen.

measured versus temperature. Figure 2.18 schematically shows that in the beginning of the zfc curve of figure 7.4 the particles are unordered cooled down at zero magnetic field (the spins are frozen). When the blocking temperature is reached, the magnetization has its highest value (see figure 7.4 blocking temperature is sketched in). Here, the blocking temperature for the nickel tubes is about 180 K. Then the magnetization slightly decreases with a rising temperature. The spins can rotate freely (s. figure 2.18 (b)).

The zero point of the measurement is disabled, so it is only a small part in which a pure ferromagnetic behavior of single part areas cannot be excluded. During the fc measurement the sample is cooled down in an applied field and the magnetization is detected (see figure 7.4). The magnetic moments have aligned after another in the field and are frozen. Here, the magnetization is saturated.

## 7.2. NiCo nanotubes

### 7.2.1. Introduction

This is the first time that the nickel/ cobalt material system has been successfully synthesized by ALD process. It is an ozone generated process with the precursors materials comprising nickelocene and cobaltocene. First, the ALD process is presented and subsequently the respective magnetic characterization of the samples. In this section it will be shown that the superparamagnetic behavior which was seen for the nickel tubes could be overcome by improving the reduction conditions, so that finally the geometries of the samples is put forward. The deposition was carried out at 220°C with two precursors: nickelocene/ cobaltocene and ozone. The nickel/ cobalt precursor contained nickelocene/ cobaltocene with a mixture ratio of 50 % (process parameters can be found in table A.4). Here, a method by chemical analysis and magnetic measurements will give detailed information of the elemental composition through the resulting values and the corresponding magnetic behavior. This is highlighted in section 7.2.2. To start with, TEM analysis is being put forward. Figure 7.5 displays a transmission

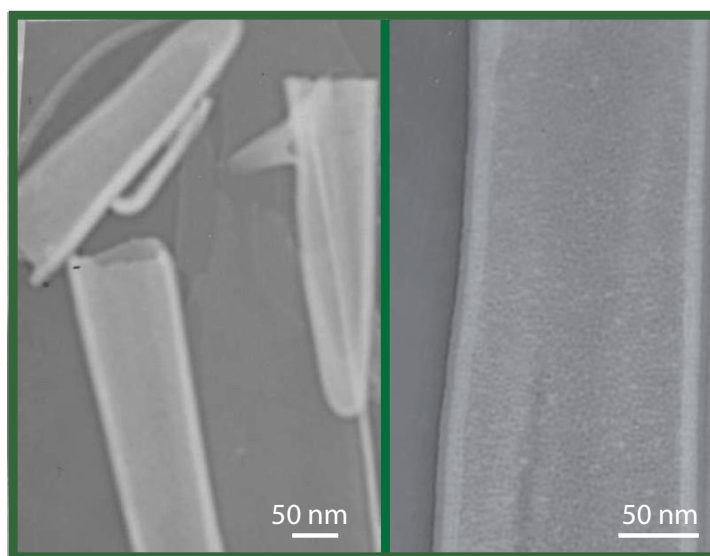


**Figure 7.5.:** Transmission electron micrographs of single nickel/ cobalt tubes, isolated from the alumina template by chromic acid etching.

electron micrograph of a nickel/ cobalt tube obtained after release from the alumina matrix in chromic acid solution. The left panel shows 3 broken tubes, the closed bottom area is clearly to see. Through the releasing process and the step afterwards the centrifugation process the tubes can be broken. The diameters shown here are about 70 nm. The right panel shows a thick segment (about 150 nm diameter) with a higher magnification. The different layers are clearly to see, there is a 5-nm thick SiO<sub>2</sub> layer deposited onto the alumina pore walls by atomic

layer deposition (ALD) [BZC<sup>+</sup>08] and the afterwards deposited nickel/ cobalt layer (10 nm). The thick segment corresponds to the mild anodization (see chapter 3.1.2). In the text the 70-nm wide segment is called 'hard' and the 150-nm wide segment is called 'mild'. The diameters of the samples are always the same. First, EDX was used to determine the nickel cobalt ratio. EDX analysis, this acts as a method to qualify the element present in the layer, but however it is difficult to quantify the amount due to the low element presence. From the periodic table the elements Co and Ni are very close to each other(atomic No. Co: 27 and Ni: 28), hence it is almost difficult with EDX to make a perfect detection and as well give a real composition ratio of the elements respectively. Due to this, only the results of composition ratio from the chemical analysis<sup>1</sup> are shown(table 7.1). The samples were solved in acid and then analyzed by absorption spectrometry. Graphite furnace atomic absorption spectrometry (GAAS)<sup>2</sup> and flame atomic absorption spectrometry (FAAS)<sup>3</sup> was used for the determination of the metal concentrations in solution. The results of a dissolved film and tubes show that the nickel content is about 99,6 %, cobalt has only a very low content of 0,4 %. The relative measurement error is about 5 %.

sample	Ni content	Cobalt content	deposition ratio $\approx$
film	338 $\mu g/L$	1.2 $\mu g/L$	Ni/Co: 99,7:0,3
nanotubes	473 $\mu g/L$	2.1 $\mu g/L$	Ni/Co: 99,6:0,4

**Table 7.1.:** The table shows the chemical analysis of a nickel/ cobalt film and tubes(both 10 nm layerthickness).

## 7.2.2. Magnetic measurements

It was shown that the samples consists of nickel/ cobalt with a bigger ratio Ni, the following magnetic measurements underline this assumption. The figure 7.6 shows a hysteresis of the thin nickel/ cobalt film (about 10 nm). On the one hand, it was shown that the samples consists of nickel/ cobalt with a bigger ratio nickel, where the behavior was strongly confirmed with magnetic measurements. The nickel/ cobalt shows a typical soft magnetic behavior. The coercive field  $H_c$  ( $x$  intercept) and the remanence  $\mu_{rem}$  ( $y$  intercept) are not significantly affected by the orientation of the sample. But the square shape of the hysteresis in the parallel direction underlines this assumption. The squareness is 70 % and is reduced with respect to the perpendicular measurement which yields 20 % squareness. The saturation magnetization was calculated and is about  $550 \text{ emu/cm}^2 \pm 100 \text{ emu/cm}^2$ . The calculated value is comparable to the bulk in the literature. There, nickel has a saturation magnetization of  $485 \text{ emu/cm}^2$  and cobalt of  $1440 \text{ emu/cm}^2$ [O'H01].

<sup>1</sup>Done by Torborg Krugmann

<sup>2</sup>GAAS Analytik Jena company, contrAA 700

<sup>3</sup>FAAS: Thermo company, SOLAAR S

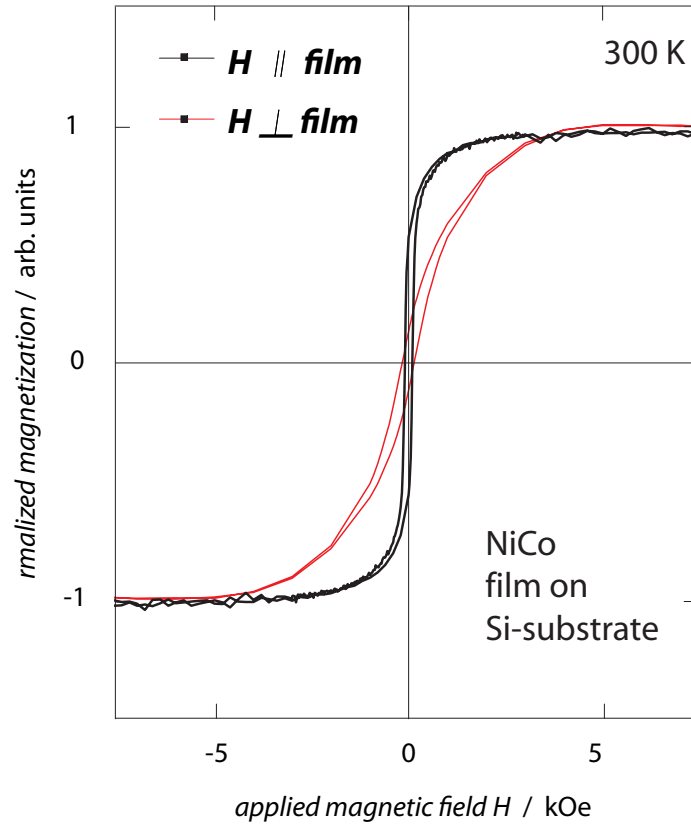


**Figure 7.6.:** Magnetic hysteresis loops of a nickel/ cobalt film (10 nm thickness) in a field applied parallel and perpendicular to the long axis ( $z$  axis) of the film at 300 K. The coercive field  $H_c$  and the remanence  $\mu_{rem}$  are not significantly affected by the orientation of the sample ( $H_c^{\parallel} = 100$  Oe ;  $\mu_{rem}^{\parallel} = 0.7 \mu_{sat}$  and  $H_c^{\perp} = 100$  Oe ;  $\mu_{rem}^{\perp} = 0.2 \mu_{sat}$ ). The values of the magnetization are normalized to the saturated magnetization.

Now, the different nickel/ cobalt nanotubes are introduced. First, one sample with a thick diameter is introduced. This is one sample of the first charge. In this first charge, the nickel/ cobalt oxide samples were reduced in  $Ar/H_2$  for 3 h. The measurement was done at 300 K (SQUID MPMSXL by Quantum Design). Figure 7.7 shows a hysteresis loop at room temperature with the orientation tubes parallel and perpendicular to the applied field. The geometry of the sample is shown in the figure.

There is a very small coercive field observable in both directions ( $H_c^{\parallel} = 30$  Oe and  $H_c^{\perp} = 23$  Oe), also the remanence is very small ( $\mu_{rem}^{\parallel} = 0.15 \mu_{sat}$  and  $\mu_{rem}^{\perp} = 0.02 \mu_{sat}$ ). The coercive field and the remanence, is though very small but however, it is bigger in the parallel direction in comparison to the perpendicular orientation to the applied field. This is also an indication that the nickel/ cobalt consists of a bigger ratio of nickel than cobalt, it assumes a soft magnetic behavior. The values of the magnetization are normalized to the saturated magnetization. If one consider the small coercive fields and remanence at room temperature and also the vanishing shape anisotropy, there is no significant difference between the

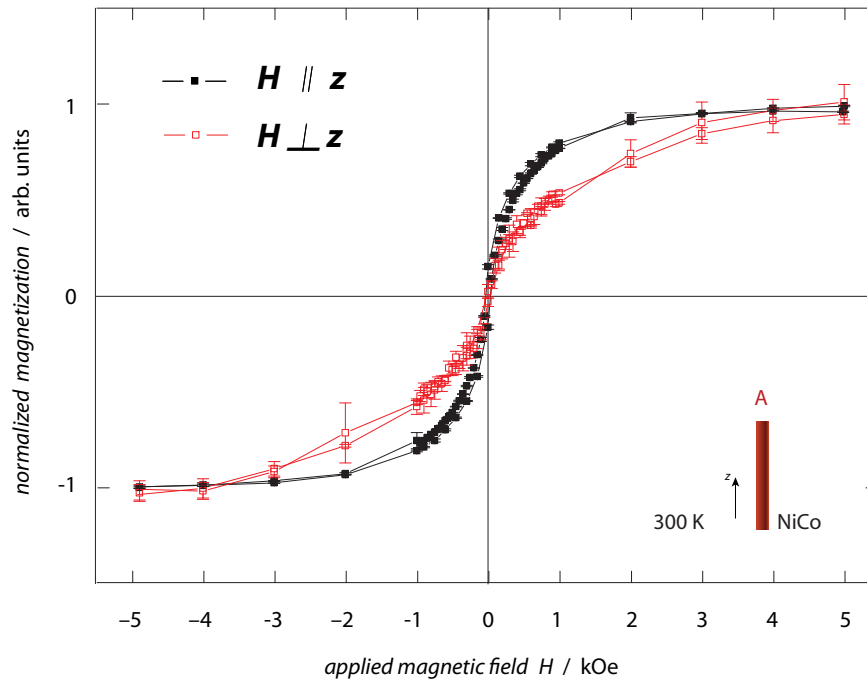


**Figure 7.7.:** Magnetic hysteresis loops of an array of nickel/ cobalt nanotubes (10 nm wall thickness) in a field applied parallel and perpendicular to the long axis ( $z$  axis) of the tubes at 300 K. The coercive field  $H_c$  and the remanence  $\mu_{rem}$  are not significantly affected by the orientation of the sample ( $H_c^{\parallel} = 30$  Oe ;  $\mu_{rem}^{\parallel} = 0.15 \mu_{sat}$  and  $H_c^{\perp} = 23$  Oe;  $\mu_{rem}^{\perp} = 0.02 \mu_{sat}$ ). Anodization conditions of the template: mild(150 nm diameter) 15  $\mu\text{m}$ . At 300 K the coercive fields are very small. The error bar of the standard deviation of the magnetization is included.

perpendicular and parallel orientation of the tubes in the applied field, it assumes that these nanotubes consist of nanoparticles and behave superparamagnetically. The following temperature dependent measurement underlines this assumption. Figure 7.8 shows two temperature dependent measurements in a curve of nickel/ cobalt tubes with a diameter of 150 nm and a length of 15  $\mu\text{m}$ . As mentioned before the sample is cooled at a zero magnetic field, then during the zero field cooling measurement the sample is warmed up at a small applied magnetic field. The induced magnetization is measured versus temperature. In the beginning of zfc curve the particles are unordered cooled down in zero magnetic field. The magnetization increases with a rising temperature till the blocking temperature is reached. Here, the blocking temperature for the nickel/ cobalt tubes is about 102 K. Afterwards the magnetization slightly decreases with a increasing temperature. The other curve shows a fc measurement in which the sample is cooled down in an applied field and the magnetization is detected (see figure 7.8). In the field the spins have aligned after another and are frozen, in the end of the curve magnetization is nearly constant. These temperature dependent measurement show that these nanotubes behave superparamagnetically, the superparamagnetic effect of the particles dominates over the shape anisotropy.

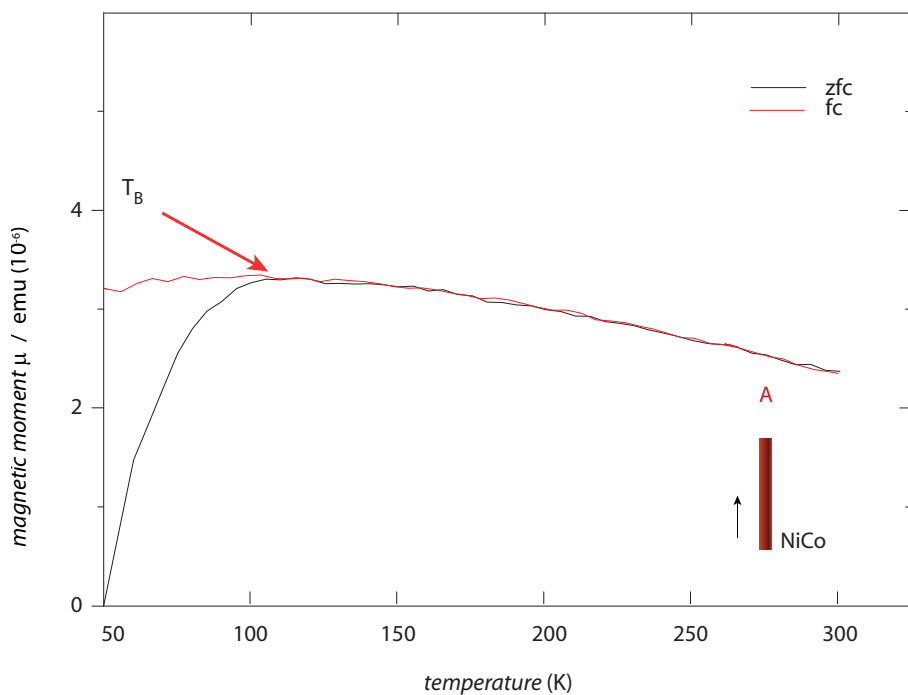


**Figure 7.8.:** The curve illustrates the two procedures of measuring the temperature-dependent magnetization: zero field cooling and field cooling. Shown is a sample of nickel nanotubes which behave superparamagnetic, defined by the characteristic  $T_B$  at 102 K, the zfc and fc curve. The measurement was done at an applied field of 100 Oe.

Next, three samples with different geometries are presented. They are schematically drawn in figure 3.9 (c2). Here, the reduction process was optimized. These nanotubes were reduced in Ar/H<sub>2</sub> for only 90 min. In the following measurements the shape anisotropy comes into play, as well as the differences of the diameters of presented samples would be the parameter to be investigated in the magnetic measurements.

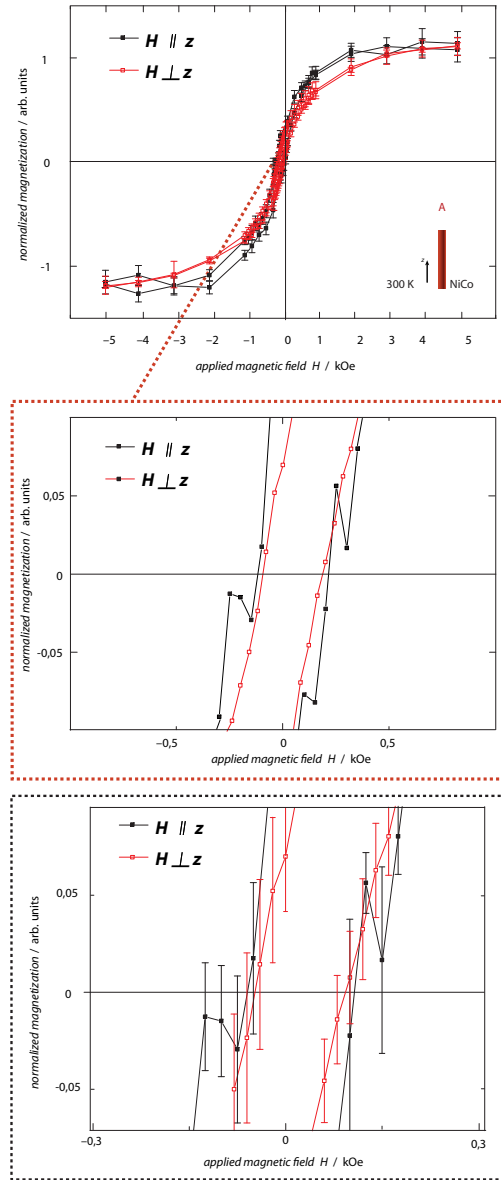


**Figure 7.9.:** Magnetic hysteresis loops of an array of nickel/ cobalt nanotubes (10 nm wall thickness) in a field applied parallel or perpendicular to the long axis ( $z$  axis) of the tubes at 300 K. Both the coercive field  $H_c$  and the remanence  $\mu_{rem}$  are not strongly affected by the orientation of the sample ( $H_c^{\parallel} = 100$  Oe;  $H_c^{\perp} = 66$  Oe;  $\vec{H} \perp \vec{z}$ ,  $\mu_{rem}^{\parallel} = 0.2 \mu_{sat}$ ;  $\mu_{rem}^{\perp} = 0.15 \mu_{sat}$ ). Anodization conditions of the template: mild(150 nm diameter) 15  $\mu\text{m}$ . The error bar of the standard deviation of the magnetization is included. The area around coercive field is also shown in two magnifications to see that the error of the standard deviation is very big for some values.

The first sample is shown in figure 7.9. The measurement was done at 300 K (SQUID MPMS2 by Quantum Design). When the sample is magnetized to saturation in a magnetic field  $H = 5$  kOe applied along the long axis of the tubes,  $\vec{H} \parallel \vec{z}$ , and the field is then turned off, 20 % of the saturated magnetization is retained (remanence,  $\mu_{rem}^{\parallel} = 0.2 \mu_{sat}$ ). In a perpendicularly applied field,  $\vec{H} \perp \vec{z}$ , the same experiment yields a remanence  $\mu_{rem}^{\perp} = 0.15 \mu_{sat}$ . This sample shows only a small difference between the coercive fields parallel and perpendicular to the applied field ( $H_c^{\parallel} = 66$  Oe;  $H_c^{\perp} = 100$  Oe), but the coercive field parallel to the tube axis is bigger than the coercive field perpendicular to the tube axis. The direction parallel to the tubes is defined as the 'easy' axis of the sample. From this behavior, one could consider and generalize a soft magnetic behavior of the sample. Hence, a bigger ratio of nickel is assumed. The saturation magnetization was calculated and is about  $580 \text{ emu/cm}^2 \pm 30 \text{ emu/cm}^2$  and so comparable to the bulk in literature. There nickel has a saturation magnetization of 485 and cobalt 1440  $\text{emu/cm}^2$ [O'H01].

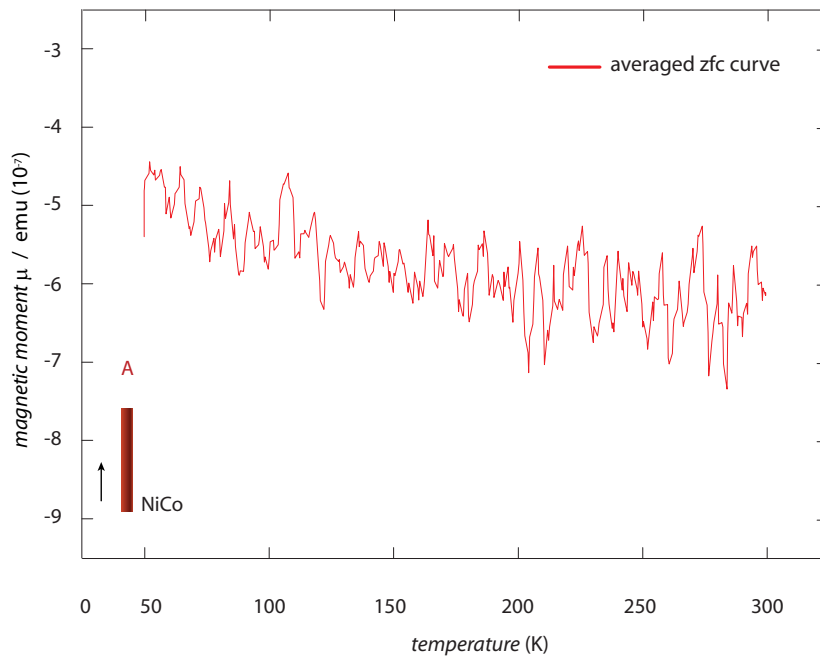


**Figure 7.10.:** The zfc curve nickel/ cobalt nanotubes reveals a continuous rise of the magnetic moment, non-superparamagnetic behavior is observed. The measurement was done at an applied field of -100 Oe. The averaged curve of zfc measurement is shown. Anodization conditions of the template: mild(150 nm diameter) 15  $\mu\text{m}$ .

Figure 7.10 shows one temperature dependent measurements in a curve of nickel/ cobalt tubes with a diameter of 150 nm and a length of 15  $\mu\text{m}$ . The sample is cooled at a zero magnetic field, then during the zero field cooling measurement the sample is warmed up at a small applied magnetic field. In this measurement no superparamagnetic is observed, as there is only a small jump to low temperatures



shown. The red line shows a curve of the averaged measured values.

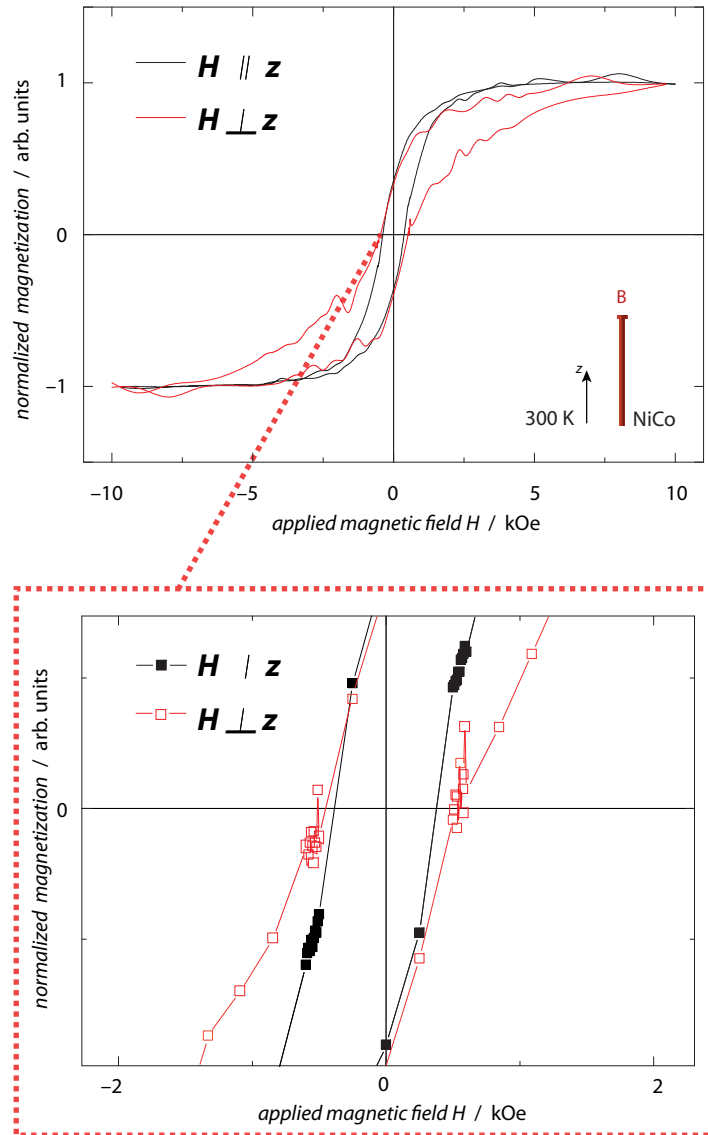


**Figure 7.11.:** Magnetic hysteresis loops of an array of nickel/ cobalt nanotubes (10 nm wall thickness) in a field applied parallel or perpendicular to the long axis ( $z$  axis) of the tubes at 300 K. Both the coercive field  $H_c$  and the remanence  $\mu_{rem}$  are affected by the orientation of the sample ( $H_c^{\parallel} = 383$  Oe;  $H_c^{\perp} = 482$  Oe;  $\vec{H} \perp \vec{z}$   $\mu_{rem}^{\parallel} = 0.4 \mu_{sat}$ ;  $\mu_{rem}^{\perp} = 0.4 \mu_{sat}$ ). Anodization conditions of the template (mild: 150 nm diameter, hard: 70 nm diameter): hard 1  $\mu\text{m}$  and mild 20  $\mu\text{m}$ . The values of the magnetization are normalized to the saturated magnetization.

Now, the second sample is shown in figure 7.11. The SQUID measurement was done at 300 K. When the sample is magnetized to saturation in a magnetic field  $H = 10$  kOe applied along the long axis of the tubes,  $\vec{H} \parallel \vec{z}$ , and the field is then

turned off, 40 % of the saturated magnetization is retained (remanence,  $\mu_{rem}^{\parallel} = 0.4 \mu_{sat}$ ). In a perpendicularly applied field,  $\vec{H} \perp \vec{z}$ , the same experiment yields also a remanence  $\mu_{rem}^{\perp} = 0.4 \mu_{sat}$ . The differences in the coercive fields between  $H_c^{\parallel} = 383$  Oe and  $H_c^{\perp} = 482$  Oe are about 100 Oe. The hysteresis curve shows for the parallel alignment a higher squareness and not as expected for the perpendicular alignment. In the perpendicular alignment there are two thicker parts in the hysteresis, in the part of the reversal process of the tubes. The shape resembles results obtained on 1D-cylindrical discs [Neu06] and 1D-ring nanostructures [Rec07] where it has been interpreted as features of a vortex rotation. Here, the current results might stem from a vortex wall reversal. To explain this new phenomena, simulations has to be done in future. Here, only the proof of concept is done for promising future studies with a soft magnetic material.

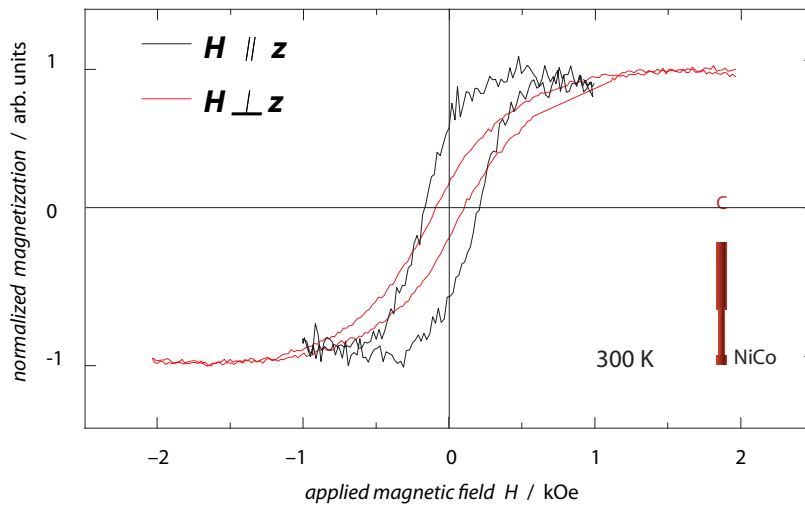


**Figure 7.12.:** Magnetic hysteresis loops of an array of nickel/ cobalt nanotubes (10 nm wall thickness) in a field applied parallel to the long axis ( $z$  axis) of the tubes at 300 K. The coercive field  $H_c$  and the remanence  $\mu_{rem}$  are strongly affected by the orientation of the sample  $H_c^{\parallel} = 161$  Oe;  $\mu_{rem}^{\parallel} = 0.65 \mu_{sat}$  and  $H_c^{\perp} = 45$  Oe;  $\mu_{rem}^{\perp} = 0.2 \mu_{sat}$ . Anodization conditions of the template(mild: 150 nm diameter, hard: 70 nm diameter): mild 10  $\mu\text{m}$  and hard 8  $\mu\text{m}$ , and mild 1  $\mu\text{m}$ .

The figure 7.12 shows hysteresis loops of the third sample. These measurements were done with the VSM while the sample was measured in two configuration against the applied field parallel or perpendicular (figure 7.12). These measurements were done at 300 K. The coercive fields differ between the two measurement configurations. If the field is parallel to the wire axis  $H_c^{\parallel} = 161$  Oe and if the field is applied perpendicular  $H_c^{\perp} = 45$  Oe. Also the remanence has different values:  $\mu_{rem}^{\parallel} = 0.65 \mu_{sat}$  and  $\mu_{rem}^{\perp} = 0.2 \mu_{sat}$ . The difference between  $\mu_{rem}^{\parallel}$  and  $\mu_{rem}^{\perp}$  defines  $z$  as the 'easy' axis of the sample, as expected from the shape anisotropy. These results were also found for nickel/ cobalt wires prepared by electrodeposition [VBM<sup>+</sup>12]. Here, also the coercive field is higher for the  $\vec{H} \parallel \vec{z}$

alignment compared with figure 7.11. Indeed, a hysteresis loop measured at 50 K (with  $\vec{H} \parallel \vec{z}$  and  $\vec{H} \perp \vec{z}$ ) on the ensemble of tubes is shown. The squareness is 70 % and coercive field (428 Oe) is reduced with respect to the perpendicular measurement (which yields 20 % squareness and 161 Oe coercive field). So, for lower temperatures higher values for the coercive fields can be found.

First, one sample without any modulation was presented if one compare this sample to the second one, it is obvious that the diameter variation have an influence on the coercive field. If the diameter is almost thin, so the sample consists more of a hard segment, the coercive field gets higher. This was also seen for the iron III oxide tubes, the sample consisting of only one mild segment has almost no remanence (see figure 6.3), there are no differences in the coercive fields, if the tubes are parallel or perpendicular to the applied field. But if the sample consists of a bigger thinner segment the coercive fields see figure 6.4) increase. If the figures 7.9 and 7.12 are compared the diameter variations have an influence on the coercive fields and the remanence. If one more variation is included the values are decreased. Now, the experimental results are summarized and an outlook is given in the following chapter 8.

## 8. Summary

In this thesis different materials and cylindrical nanostructures were fabricated to analyze the magnetic reversal mechanisms. The pinning and depinning of domain walls was in addition analyzed. It could be shown and demonstrated that porous alumina act as a suitable template system in creating of 3D-cylindrical nanoobjects with the controlled introduction of variations in diameter, which could function as pinning sites for magnetic domain boundaries. The nanowires were fabricated by ED while the nanotubes by ALD process.

The results of nanowires and nanotubes revealed that the designed structural irregularities have consequences of prime importance on the magnetic characteristics of the nanowires and the nanotubes. The nanowires results also show that in single-object measurements, it was able to observe hints on domain wall pinning in some cases, but the pinning probability is very low. Furthermore, the presence of modulations also affects the magnetic properties of wire ensembles. In a simple analytical framework, it was possible to account for the differences between the various types of modulated wires and calculate their enhanced interaction in the array. The model reveals the limitations for multiple modulations: This is a token that they influence either the nucleation domain boundaries or their propagation. Micromagnetic simulations could help for future studies, this was slightly introduced and as recently shown in some new publications e.g. from Yan and co-workers[YAK+11]. Also for the nanotubes, it was demonstrated that diameter modulations have an influence on the magnetic reversal. Ensemble measurements combined with theoretical modeling revealed the special properties of diameter changes with respect to the stray field of elongated magnetic nanoobjects.

On the one hand, it was shown that the geometry of the nanostructures can influence the magnetic properties, on the other hand, it is also important that the template is filled with magnetic material comprising a low crystalline anisotropy. Different material systems were presented. Nickel was fabricated by ED and also by ALD, alloy of nickel/ cobalt by ALD as well as iron oxide by ALD, respectively. In the nickel nanowires presented here, the pinning is not systematic. Most likely, the difference of the domain wall energy between thick and thin wire segments is too small with respect to the influence of magnetocrystalline anisotropy and thermal fluctuations. Such factors will introduce a stochastic component into the pinning phenomena. The difficulty can most logically be overcome by the use of soft magnetic materials and the creation of modulations between segments with diameters in a larger ratio. Materials like permalloy, an alloy of 80 % nickel and 20 % iron, could be a representing candidate because of its interesting small crystalline anisotropy. However, permalloy is really challenging to prepare by ALD process. So, the preparation and analysis of nickel/ cobalt was put forward.

---

Starting from Ni, for the first time, nickel/ cobalt could be synthesized successfully by ALD from nickelocene, cobaltocene and ozone. The chemical route of this ALD process was accomplished through the deposition in a single precursor thereby resulting in a fixing ratio for the nickel/ cobalt material system. As a proof of concept, the soft magnetic material comprising nickel/ cobalt(Ni/Co: 99,6:0,4) was fabricated.

As a second material  $\text{Fe}_3\text{O}_4$  was synthesized. The Verwey transition which occurred in the nanotubes indicated the magnetite. This transition has no influence on the magnetic properties. The effective anisotropy only consists of the shape anisotropy and the impact of the diameter modulations of the nanotubes could be analyzed.

The experimental results show that the magnetocrystalline anisotropy of the material, even if it is polycrystalline, can compete with the effects of the shape anisotropy. So, the implementation of nickel/ cobalt by ALD is a promising process for future studies of a soft magnetic material(controlling the nickel/ cobalt ratio by ALD in two precursors).

It was demonstrated that effects like superparamagnetism could influence the magnetic properties of the nanostructures. These nanostructures consists only of nanoparticles. Shape anisotropy of these samples is only dominated by the particles and not by the whole nanostructure. But the superparamagnetic effect could be successfully overcome by improving the preparative process. In this case the reduction process which is needed when a metallic oxide is deposited e.g.  $\text{Fe}_2\text{O}_3$  to  $\text{Fe}_3\text{O}_4$  was however improved. The reduction process for the iron oxide nanotubes and the nickel/ cobalt could be optimized, so that the material system consisting of iron III oxide as well as the alloy of nickel/ cobalt were no longer superparamagnetic. To conclude, the reduction process has a major influence on the magnetic behavior of the nanostructures, so this should also be analyzed in detail for future studies of e.g. new nickel/ cobalt compositions.

This work has shown that it is possible to tailor the properties of the nanostructures via the geometrical shape and the complex chemical composition. The segmentation of nanowires and nanotubes comprising different soft magnetic material could enhance the pinning probability at the diameter modulations. In future studies, single-object measurements as measured for nickel nanowires (magneto-optical Kerr effect, magnetic force microscopy) should be used to study the magnetic switching events spatially resolved in the individual segments and without dipole interactions. These nanostructures could work as models for the implementations of novel data storage applications working with the controlled motion of domain walls. Thus, it could be possible to use a 3D-nanostructure for a higher storage density. The enhanced stray field at diameter modulations have to be considered and investigated in more detail for the implementation of these structures in new data storage applications.

# Bibliography

- [AAN09] S. Allende, D. Altbir, and K. Nielsch. 'Magnetic cylindrical nanowires with single modulated diameter'. *Phys. Rev. B*, **80**:174402, 2009.
- [ABDH97] A. O. Adeyeye, J. A. C. Bland, C. Daboo, and D. G. Hasko. 'Magnetostatic interactions and magnetization reversal in ferromagnetic wires'. *Phys. Rev. B*, **56**:3265–3270, 1997.
- [ACM86] D. J. h Arrowsmith, A. W. Clifford, and D. A. Moth. 'Fracture of anodic oxide formed on aluminum in sulfuric-acid'. *J. Mater. Sci. Lett.*, **5**:921–922, 1986.
- [AG02] P. Aranda and J. M. Garcia. 'Porous membranes for the preparation of magnetic nanostructures'. *J. Magn. Magn. Mater.*, **249**:214–219, 2002.
- [Aha96] A. Aharoni. *'Introduction to the theory of ferromagnetism'*. Clarendon, 1996.
- [Alb06] O. Albrecht. *'SQUID und AC-Suszeptometrie an Nanomagneteten'*. Diploma thesis, Department Physik der Universität Hamburg, 2006.
- [Alb10] O. Albrecht. *'Static and dynamic properties of confined magnetic nanostructures'*. PhD thesis, Department Physik der Universität Hamburg, 2010.
- [ANN<sup>+</sup>01] H. Asoh, K. Nishio, M. Nakao, T. Tamamura, and H. Masuda. 'Conditions for fabrication of ideally ordered anodic porous alumina using pretextured Al'. *J. Electrochem. Soc.*, **148**:B152–B156, 2001.
- [ARS<sup>+</sup>03] T. Aaltonen, M. Ritala, T. Sajavaara, J. Keinonen, and M. Leskelä. 'Atomic layer deposition of platinum thin films'. *Chem. Mater.*, **15**:1924–1928, 2003.
- [AZP<sup>+</sup>10] O. Albrecht, R. Zierold, C. Patzig, J. Bachmann, B. Sturm, C. Rheinländer, M. Grundmann, D. Görnitz, B. Rauschenbach, and K. Nielsch. 'Tubular magnetic nanostructures based on glancing angle deposited templates and atomic layer deposition'. *Phys. Status Solidi B*, **247**:1365137, 2010.
- [Bö9] Tim Böhnert. *'Magneto-Widerstandsmessungen an fotolithografisch kontaktierten Nickel-Nanodrähten'*. Diploma thesis, Department Physik der Universität Hamburg, 2009.

- [Bar30] H. Barkhausen. 'Whistling tones from the earth'. *Proc. IRE*, **18**:7, 1930.
- [BGM<sup>+</sup>01] C. T. Black, K. W. Guarini, K. R. Milkove, S. M. Baker, T. P. Russell, and M. T. Tuominen. 'Integration of self-assembled diblock copolymers for semiconductor capacitor fabrication'. *Appl. Phys. Lett.*, **79**:409–411, 2001.
- [BH49] W. Blum and G. B. Hogaboom. '*Principles of electroplating and electroforming (electrotyping)*'. New York, NY : McGraw-Hill, 1949.
- [BJK<sup>+</sup>07] J. Bachmann, J. Jing, M. Knez, S. Barth, H. Shen, S. Mathur, U. Gösele, and K. Nielsch. 'Ordered ironoxide nanotube arrays of controlled geometry and tunable magnetism by atomic layer deposition'. *J. Am. Chem. Soc.*, **129**:9554–9555, 2007.
- [BK09] S. Bedanta and W. Kleemann. 'Supermagnetism'. *J. Phys. D: Appl. Phys.*, **42**:013001, 2009.
- [Blu01] S. Blundell. '*Magnetism in condensed matter*'. Oxford University Press, 2001.
- [BML<sup>+</sup>08] J. Briones, F. Montaigne, D. Lacour, M. Hehn, M. J. Carey, and J. R. Childress. 'Magnetic domain wall propagation in a submicron spin-valve stripe: Influence of the pinned layer'. *Appl. Phys. Lett.*, **92**:032508, 2008.
- [BMT<sup>+</sup>98] L. Belliard, J. Miltat, A. Thiaville, S. Dubois, J.L. Duvail, and L. Piraux. 'Observing magnetic nanowires by means of magnetic force microscopy'. *J. Magn. Magn. Mater.*, **190**:1–16, 1998.
- [Bon00] D.A. Bonnell. '*Scanning probe microscopy and spectroscopy: Theory, techniques, and applications*'. John Wiley & Sons, 2000.
- [BTH<sup>+</sup>04] W. Bruckner, J. Thomas, R. Hertel, R. Schafer, and C.M. Schneider. 'Magnetic domains in a textured Co nanowire'. *J. Magn. Magn. Mater.*, **283**:82–88, 2004.
- [BVR<sup>+</sup>92] J. S. Beck, J. C. Vartuli, W. J. Roth, M. E. Leonowicz, C. T. Kresge, K. D. Schmitt, C. T. W. Chu, D. H. Olson, and E. W. Sheppard. 'A new family of mesoporous molecular sieves prepared with liquid crystal templates'. *J. Am. Chem. Soc.*, **114**:10834–10843, 1992.
- [BYK<sup>+</sup>08] C. Bae, H. Yoo, S. Kim, K. Lee, J. Kim, M. M. Sung, and H. Shin. 'Template-directed synthesis of oxide nanotubes: Fabrication, characterization, and applications'. *Chem. Mater.*, **20**:756–767, 2008.
- [BZC<sup>+</sup>08] J. Bachmann, R. Zierold, Y. T. Chong, R. Hauert, C. Sturm, R. Schmidt-Grund, B. Rheinländer, M. Grundmann, U. Gösele, and K. Nielsch. 'Selbstkatalytische Atomlagenabscheidung von Siliciumdioxid'. *Angew. Chem. Int. Edit.*, **47**:6177–6179, 2008.

- [Cab36] V. Caboni. *Italian Patent*. 339232, 1936.
- [CAS<sup>+</sup>11] J. Y. Chen, N. Ahmad, D. W. Shi, W. P. Zhou, and X. F. Han. 'Synthesis and magnetic characterization of Co-NiO-Ni core-shell nanotube arrays'. *J. Appl. Phys.*, **110**:073912, 2011.
- [CGGH05] C. D. Cheng, R. K. Gonela, Q. Gu, and D. T. Haynie. 'Self-assembly of metallic nanowires from aqueous solution'. *Nano Lett.*, **5**:175–178, 2005.
- [CH61] P. Csokán and M. Holló. 'Beitrag zur Frage des Bildungsmechanismus von anodisch erzeugten Hartoxydschichten'. *Mater. Corros.*, **12**:288–295, 1961.
- [Cho97] S. Y. Chou. 'Patterned magnetic nanostructures and quantized magnetic disks'. *P. IEEE*, **85**:652, 1997.
- [CKA<sup>+</sup>99] R. P. Cowburn, D. K. Koltsov, A. O. Adeyeye, M. E. Welland, and D. M. Tricker. 'Single-domain circular nanomagnets'. *Phys. Rev. Lett.*, **83**:1042, 1999.
- [CLY94a] C-R. Chang, C. M. Lee, and J.-S. Yang. 'Atomic-structure and electronic-structure of amorphous Si from first-principles molecular-dynamics simulations'. *Phys. Rev. B*, **50**:6461, 1994.
- [CLY94b] C-R. Chang, C. M. Lee, and J.-S. Yang. 'Magnetization curling reversal for an infinite hollow cylinder'. *Phys. Rev. B*, **50**:6461–6464, 1994.
- [CS62] P. Csokán and C. C. Sc. 'Hard anodizing: Studies of the relation between anodizing conditions and the growth and properties of hard anodic oxide coatings'. *Electroplat. Metal Finish*, **15**:75–82, 1962.
- [Cso64] P. Csokán. 'Some observations on the growth mechanism of hard anodic oxide coatings on aluminium'. *T. I. Me. Finish.*, **41**:51–56, 1964.
- [CSRC05] N. B. Chaure, P. Stamenov, F.M.F. Rhen, and J.M.D. Coey. 'Oriented cobalt nanowires prepared by electrodeposition in a porous membrane'. *J. Magn. Magn. Mater.*, **290**:1210–1213, 2005.
- [CWI<sup>+</sup>05] S. Z. Chu, K. Wada, S. Inoue, M. Isogai, and A. Yasumori. 'Fabrication of ideally ordered nanoporous alumina films and integrated alumina nanotubule arrays by high-field anodization'. *Adv. Mater.*, **17**:2115–2119, 2005.
- [CYY<sup>+</sup>11] Y. T. Chong, M. Y. E. Yau, Y. Yang, M. Zacharias, D. Gorlitz, K. Nielsch, and J. Bachmann. 'Superparamagnetic behavior in cobalt iron oxide nanotube arrays by atomic layer deposition'. *J. Appl. Phys.*, **110**:043930, 2011.



- [DDB<sup>+</sup>08] A. A. Dameron, S. D. Davidson, B. B. Burton, P. F. Carcia, R. S. McLean, and S. M. George. 'Gas diffusion barriers on polymers using multilayers fabricated by Al<sub>2</sub>O<sub>3</sub> and rapid SiO<sub>2</sub> atomic layer deposition'. *J. Phys. Chem. C*, **112**:4573–4580, 2008.
- [DDG69] J. W. Diggle, T. C. Downie, and C. W. Goulding. 'Anodic oxide films on aluminum'. *Chem. Rev.*, **69**:365, 1969.
- [Des90] Quantum Design. '*Manual MPMS/MPMS2*'. 1986/1990.
- [Din93] J. W. Dini. '*Electrodeposition: The materials science of coatings and substrates*'. Noyes Publications, 1993.
- [DKGN07] M. Daub, M. Knez, U. Gösele, and K. Nielsch. 'Ferromagnetic nanotubes by atomic layer deposition in anodic alumina membranes'. *J. Appl. Phys*, **101**:09J111, 2007.
- [DL92] M. E. Davis and R. F. Lobo. 'Zeolite and molecular sieve synthesis'. *Chem. Mater.*, **4**:756–768, 1992.
- [DL00] M. Datta and D. Landolt. 'Fundamental aspects and applications of electrochemical microfabrication'. *Electrochim. Acta*, **45**:2535–2558, 2000.
- [DP89] A. Despic and V. P. Parkhutik. '*Modern aspects of electrochemistry*'. Plenum, New York, 1989.
- [DP99] M. J. Donahue and D. G. Porter. '*OOMMF Users Guide*'. NIST, 1999.
- [EAA<sup>+</sup>09] J. Escrig, S. Allende, D. Altbir, M. Bahian, J. Torrejón, G. Badini, and M. Vázquez. 'Magnetostatic bias in multilayer microwires: Theory and experiments'. *J. Appl. Phys.*, **105**:023907, 2009.
- [EAAB08] J. Escrig, S. Allende, D. Altbir, and M. Bahiana. 'Magnetostatic interactions between magnetic nanotubes'. *Appl. Phys. Lett.*, **93**:023101, 2008.
- [EAJ<sup>+</sup>07] J. Escrig, D. Altbir, M. Jaafar, D. Navas, A. Asenjo, and M. Vázquez. 'Remanence of Ni nanowire arrays: Influence of size and labyrinth magnetic structure'. *Phys. Rev. B*, **75**:184429, 2007.
- [EBJ<sup>+</sup>08] J. Escrig, J. Bachmann, J. Jing, M. Daub, D. Altbir, and K. Nielsch. 'Crossover between two different magnetization reversal modes in arrays of iron oxide nanotubes'. *Phys. Rev. B*, **77**:214421, 2008.
- [EG03] J. W. Elam and S. M. George. 'Growth of ZnO/Al<sub>2</sub>O<sub>3</sub> alloy films using atomic layer deposition techniques'. *Chem. Mater.*, **15**:1020–1028, 2003.

- [ELP<sup>+</sup>08] J. Escrig, R. Lavín, J. L. Palma, J. C. Denardin, D. Altbir, A. Cortés, and H. Gómez. 'Geometry dependence of coercivity in Ni nanowire arrays'. *Nanotechnology*, 19:075713, 2008.
- [ELR<sup>+</sup>03] J. Escrig, P. Landeros, C. J. Retamal, D. Altbir, and J. J. d'Albuquerque e Castro. 'Magnetic behavior of nanoparticles in patterned thin films'. *Appl. Phys. Lett.*, 82:3478–3480, 2003.
- [ERMG03] J. W. Elam, D. Routkevitch, P. P. Mardilovich, and S. M. George. 'Conformal Coating on Ultrahigh-Aspect-Ratio Nanopores of Anodic Alumina by Atomic Layer Deposition'. *Chem. Mater.*, 15:3507–3517, 2003.
- [Esc10] J. Escrig. private communication, 2010.
- [ESE95] A.M. El-Sherik and U. Erb. 'Synthesis of bulk nanocrystalline nickel by pulsed electrodeposition'. *J. Mater. Sci.*, 30:5743–5749, 1995.
- [Fas98] G. Fasol. 'Applied physics - Nanowires: Small is beautiful'. *Science*, 280:545–546, 1998.
- [FB68] Jr. W. Fuller Brown. 'The fundamental theorem of fine-ferromagnetic-particle theory'. *J. Appl. Phys.*, 39:993–994, 1968.
- [FBKR<sup>+</sup>04] S. Fournier-Bidoz, V. Kitaev, D. Routkevitch, I. Manners, and G. A. Ozin. 'Highly ordered nanosphere imprinted nanochannel alumina (NINA)'. *Adv. Mater.*, 16:2193–2196, 2004.
- [FBPW75] R. L. Fleischer, P. Buford Price, and R. M. Walker. '*Nuclear tracks in solids: Principles and applications*'. University of California press, 1975.
- [FFBF07] T. Fischbacher, M. Franchin, G. Bordignon, and H. Fangohr. 'A systematic approach to multiphysics extensions of finite-element-based micromagnetic simulations: Nmag'. *IEEE Trans. Magn.*, 43:2896–2898, 2007.
- [FKC<sup>+</sup>06] M. M. Frank, S. J. Koester, M. Copel, J. A. Ott, V. K. Paruchuri, H. Shang, and R. Loesing. 'Hafnium oxide gate dielectrics on sulfur-passivated germanium'. *Appl. Phys. Lett.*, 89:112905, 2006.
- [FP99] A. Fert and L. Piraux. 'Magnetic nanowires'. *J. Magn. Magn. Mater.*, 200:338–358, 1999.
- [Fra07] F. C. Frary. 'Rapid analysis by electrolysis without rotating electrodes'. *J. Am. Chem. Soc.*, 29:1592–1596, 1907.
- [FSS<sup>+</sup>02] H. Forster, T. Schrefl, W. Scholz, D. Suess, V. Tsiantos, and J. Fidler. 'Micromagnetic simulation of domain wall motion in magnetic nano-wires'. *J. Magn. Magn. Mater.*, 249:181–186, 2002.

- [FTMD04] K. Fukutani, K. Tanji, T. Motoi, and T. Den. 'Ultra-high pore density nanoporous films produced by the phase separation of eutectic Al-Si for template-assisted growth of nanowire arrays'. *Adv. Mater.*, **16**:1456–1460, 2004.
- [FTW03] P. S. Fodor, G. M. Tsoi, and L. E. Wenger. 'Modeling of hysteresis and magnetization curves for hexagonally ordered electrodeposited nanowires'. *J. Appl. Phys.*, 93:7438–7440, 2003.
- [GB08] I. Gurrappa and L. Binder. 'Electrodeposition of nanostructured coatings and their characterization: a review'. *Sci. Technol. Adv. Mat.*, **9**:043001, 2008.
- [Geo10] S. M. George. 'Atomic layer deposition: An Overview'. *Chem. Rev.*, **110**:111–131, 2010.
- [GGL<sup>+</sup>11] M. Godlewski, E. Guziejewicz, M. I. Lukasiewicz, I. A. Kowalik, M. Sawicki, B. S. Witkowski, R. Jakiela, W. Lisowski, J. W. Sobczak, and M. Krawczyk. 'Role of interface in ferromagnetism of (Zn,Co)O films'. *Phys. Status Solidi B*, **248**:1596–1600, 2011.
- [Gil55] T. L. Gilbert. 'Lagrangian formulation of the gyromagnetic equation of the magnetization'. *Phys. Rev.*, **100**:1243–1243, 1955.
- [GNB<sup>+</sup>11] D. Gu, D. Nminibapiel, H. Baumgart, H. Robinson, and V. Kochergin. 'Atomic layer deposition of antimony telluride thin films using (Me<sub>3</sub>Si)<sub>2</sub>Te with SbCl<sub>3</sub> as precursors'. *ECS Transactions*, **41**:255–261, 2011.
- [Gol03] J. Goldstein. '*Scanning electron microscope and X-ray microanalysis*'. Springer, Berlin, 2003.
- [GTM02] J.M. García, A. Thiaville, and J. Miltat. 'MFM imaging of nanowires and elongated patterned elements'. *J. Magn. Magn. Mater.*, **249**:163–169, 2002.
- [HB94] B. Heinrich and J. A. C. Bland. '*Ultrathin Magnetic Structures*'. Springer, Berlin, 1994.
- [HCD<sup>+</sup>08] A. I. Hochbaum, R. Chen, R.D. Delgado, W. Liang, E.C. Garnett, M. Najarian, A. Majumdar, and P. Yang. 'Enhanced thermoelectric performance of rough silicon nanowires'. *Nature*, **451**:163–167, 2008.
- [HCY<sup>+</sup>05] H.N. Hu, H.Y. Chen, S.Y. Yu, J.L. Chen, G.H. Wu, F.B. Meng, J.P. Qu, Y. Li, H. Zhu, and J.Q. Xiao. 'Textured Co nanowire arrays with controlled magnetization direction'. *J. Magn. Magn. Mater.*, **295**:257–262, 2005.
- [Hec88] J. G. Hecker. 'Aluminum hard coats'. *Proc. finish.*, **53**:88–92, 1988.

- [Her01] R. Hertel. 'Micromagnetic simulations of magnetostatically coupled Nickel nanowires'. *J. Appl. Phys.*, **90**:5752–5758, 2001.
- [Her02] R. Hertel. 'Computational micromagnetism of magnetization processes in nickel nanowires'. *J. Magn. Magn. Mater.*, **249**:251–256, 2002.
- [HF54] M. S. Hunter and P. Fowle. 'Determination of barrier layer thickness of anodic oxide coatings'. *J. Elec. Soc.*, **101**:481–485, 1954.
- [HN00] D. Hinzke and U. Nowak. 'Magnetization switching in nanowires: Monte Carlo study with fast Fourier transformation for dipolar fields'. *J. Magn. Magn. Mater.*, **221**:365–372, 2000.
- [HOB<sup>+</sup>96] M. Hehn, K. Ounadjela, J. P. Bucher, F. Rousseaux, D. Decanini, B. Bartenlian, and C. Chappert. 'Nanoscale magnetic domains in mesoscopic magnets'. *Science*, **272**:1782–1785, 1996.
- [HSS<sup>+</sup>09] X.-F. Han, S. Shamaila, R. Sharif, J.-Y. Chen, H.-R. Liu, and D.-P. Liu. 'Structural and Magnetic Properties of Various Ferromagnetic Nanotubes'. *Adv. Mater.*, **21**:4619–4624, 2009.
- [HTM<sup>+</sup>08] M. Hayashi, L. Thomas, R. Moriya, C. Rettner, and S. S. P. Parkin. 'Current-Controlled Magnetic Domain-Wall Nanowire Shift Register'. *Science*, **320**:209–211, 2008.
- [HNVN<sup>+</sup>11] T. Hirvikorpi, M. Vaha-Nissi, J. Vartiainen, P. Penttila, J. Nikkola, A. Harlin, R. Serimaa, and M. Karppinen. 'Effect of heat-treatment on the performance of gas barrier layers applied by atomic layer deposition onto polymer-coated paperboard'. *J. Appl. Polym. Sci.*, **122**:2221–2227, 2011.
- [JBS84] S. John, V. Balasubramanian, and B. A. Shenoi. 'Hard anodizing aluminium and its alloys-AC in sulphuric acid- sodium sulphate bath'. *Met. Finish*, **82**:33–39, 1984.
- [Jes97] O. Jessensky. '*Untersuchungen zum Porenwachstum in 6H-Siliziumkarbid und anodischem Aluminiumoxid*'. PhD thesis, Martin-Luther-Universität Halle-Wittenberg, 1997.
- [JGK<sup>+</sup>00] Y. Jaccard, P. Guittienne, D. Kelly, J. E. Wegrowe, and J. P. Ansermet. 'Uniform magnetization rotation in single ferromagnetic nanowires'. *Phys. Rev. B*, **62**:1141–1147, 2000.
- [Jil91] D. Jiles. '*Introduction to magnetism and magnetic materials*'. Cahapman& Hall, 1991.
- [Joh98] M. Johnson. 'Hybrid ferromagnet–semiconductor devices'. volume 16, pages 1806–1811. AVS, 1998.

- [KBG<sup>+</sup>02] M. Kroll, W. J. Blau, D. Grandjean, R.E. Benfield, F. Luis, P.M. Paulus, and L.J. de Jongh. 'Magnetic properties of ferromagnetic nanowires embedded in nanoporous alumina membranes'. *J. Magn. Magn. Mater.*, **249**:241–245, 2002.
- [KEC<sup>+</sup>05] O. Kazakova, D. Ertz, T.A. Crowley, J.S. Kulkarni, and J.D. Holmes. 'Temperature dependence of magnetization reversal in Co and Fe<sub>3</sub>O<sub>4</sub> nanowire arrays'. *J. Magn. Magn. Mater.*, **286**:171–176, 2005.
- [Ker77] J. Kerr. 'On rotation of the plane of polarization by reflection from the pole of a magnet'. *Philos. Mag. B*, **5**, 1877.
- [KG00] J. W. Klaus and S. M. George. 'Atomic layer deposition of SiO<sub>2</sub> at room temperature using NH<sub>3</sub>-catalyzed sequential surface reactions'. *Surf. Sci.*, **447**:81–90, 2000.
- [KHR53] F. Keller, M. S. Hunter, and D. L. Robinson. 'Structural features of oxide coatings on aluminium'. *J. Electrochem. Soc.*, **100**:411–419, 1953.
- [Kit99] C. Kittel. '*Einführung in die Festkörperphysik*'. Oldenbourg, 1999.
- [KKM<sup>+</sup>11] J. Kimling, F. Kronast, S. Martens, T. Böhnert, M. Martens, J. Herrero-Albillos, L. Tati-Bismaths, U. Merkt, K. Nielsch, and G. Meier. 'Photoemission electron microscopy of three-dimensional magnetization configurations in core-shell nanostructures'. *Phys. Rev. B*, **84**:174406, 2011.
- [Kne62] E. Kneller. '*Ferromagnetismus*'. Springer, 1962.
- [KNN07] M. Knez, K. Nielsch, and L. Niinistö. 'Synthesis and Surface Engineering of Complex Nanostructures by Atomic Layer Deposition'. *Adv. Mater.*, **19**:3425–3438, 2007.
- [KNS02] A. Kros, R.J.M. Nolte, and N.A.J.M. Sommerdijk. 'Conducting polymers with confined dimensions: Track-etch membranes for amperometric biosensor applications'. *Adv. Mater.*, **14**:1779–1782, 2002.
- [KRE<sup>+</sup>05] R. Kozhuharova, M. Ritschel, D. Elefant, A. Graff, I. Monch, T. Muhl, C.M. Schneider, and A. Leonhardt. '(Fe<sub>x</sub>Co<sub>1-x</sub>)-alloy filled vertically aligned carbon nanotubes grown by thermal chemical vapor deposition'. *J. Magn. Magn. Mater.*, **290**:250–253, 2005.
- [LAE<sup>+</sup>07] P. Landeros, S. Allende, J. Escrig, E. Salcedo, D. Altbir, and E. E. Vogel. 'Reversal modes in magnetic nanotubes'. *Appl. Phys. Lett.*, **90**:102501, 2007.
- [Lan94] D. Landolt. 'Electrochemical and materials science aspects of alloy deposition'. *Electrochim. Acta*, **39**:1075–1090, 1994.

- [LBD60] E. Lichtenberger-Bajza and P. Donony, A. and Csokoan. 'Untersuchung der Struktur und anderer Eigenschaften von durch anodische Oxydation auf Aluminium erzeugten Hartoxydschichten'. *Mater. Corros.*, **11**:701–707, 1960.
- [LBKN<sup>+</sup>08] M. Lie, K. Barnholt Klepper, O. Nilsen, H. Fjellvag, and A. Kjekshus. 'Growth of iron cobalt oxides by atomic layer deposition'. *Dalton T.*, pages 253–259, 2008.
- [LDE<sup>+</sup>09] R. Lavín, J. C. Denardin, J. Escrig, D. Altbir, A. Cortés, and H. Gómez. 'Angular dependence of magnetic properties in Ni nanowire arrays'. *J. Appl. Phys.*, **106**:103903, 2009.
- [LDRKB01] L. Lopez-Diaz, J. Rothman, M. Klaui, and J. A. C. Bland. 'Vortex formation in magnetic narrow rings: The role of magneto-crystalline anisotropy'. *J. Appl. Phys.*, **89**:7579–7581, 2001.
- [LEA<sup>+</sup>05] P. Landeros, J. Escrig, D. Altbir, D. Laroz, J. J. d'Albuquerque e Castro, and P. Vargas. 'Scaling relations for magnetic nanoparticles'. *Phys. Rev. B*, **71**:094435, 2005.
- [LGY04] M. Law, D. J. Goldberger, and P. Yang. 'Semiconductor nanowires and nanotubes'. *Annu. Rev. Mater. Res.*, **34**:83–122, 2004.
- [Lin02] J. Lindner. 'Ferromagnetische Resonanz an ultradünnen magnetischen Einfach- und Mehrfachlagen der 3d-Übergangsmetalle Statik und Dynamik'. PhD thesis, Fachbereich Physik der Freien Universität Berlin, 2002.
- [LJGN06] W. Lee, R. Ji, U. Gösele, and K. Nielsch. 'Fast fabrication of long-range ordered porous alumina membranes by hard anodization'. *Nat. Mater.*, **5**:741–747, 2006.
- [LJR<sup>+</sup>06] W. Lee, R. Ji, C. A. Ross, U. Gösele, and K. Nielsch. 'Wafer-scale Ni imprint stamps for porous alumina membranes based on interference lithography'. *Small*, **2**:978–982, 2006.
- [LL35] L. D. Landau and E. M. Lifshitz. 'On the theory of the dispersion of magnetic permeability in ferromagnetic bodies'. *reprinted Soviet. Physics JET P<sub>U</sub>SSR*, **8**: 153 – –169, 1935.
- [LMB<sup>+</sup>98] A. P. Li, F. Müller, A. Birner, K. Nielsch, and U. Gösele. 'Hexagonal pore arrays with a 50–420 nm interpore distance formed by self-organization in anodic alumina'. *J. Appl. Phys.*, **84**:6023–6026, 1998.
- [LMT<sup>+</sup>02] S. B. Lee, D. T. Mitchell, L. Trofin, T. K. Nevanen, H. Soderlund, and C. R. Martin. 'Antibody-based bio-nanotube membranes for enantiomeric drug separations'. *Science*, **296**:2198–2200, 2002.

- [Loh93] M. M. Lohregel. 'Thin anodic oxide layers on aluminum and other valve metals -high-field regime'. *Mat. Sci. Eng. R.*, **11**:243–294, 1993.
- [LR99] M. Leskelä and M. Ritala. 'ALD precursor chemistry : Evolution and future challenges'. *J. Phys. IV France*, **9**:Pr8–837–Pr8–852, 1999.
- [LR02] M. Leskelä and M. Ritala. 'Atomic layer deposition (ALD):From precursors to thin film structures'. *Thin Solid Films*, **409**:138–146, 2002.
- [LR03] M. Leskelä and M. Ritala. 'Atomic Layer Deposition Chemistry: Recent Developments and Future Challenges'. *Angew. Chem. Int. Edit.*, **42**:5548–5554, 2003.
- [LRG03] B. S. Lim, A. Rahtu, and R. G. Gordon. 'Atomic layer deposition of transition metals'. *Nat. Mater.*, **2**:749–754, 2003.
- [LSG08] W. Lee, R. Scholz, and U. Gösele. 'A continuous process for structurally well-defined Al<sub>2</sub>O<sub>3</sub> nanotubes based on pulse anodization of aluminum'. *Nano Lett.*, **8**:2155–2160, 2008.
- [LSS+08] W. Lee, K. Schwirn, M. Steinhart, E. Pippel, R. Scholz, and U. Gösele. 'Structural engineering of nanoporous anodic aluminium oxide by pulse anodization of aluminium'. *Nat. Nanotechnol.*, **3**:234–239, 2008.
- [LTD] Durham Magneto-optics LTD. 'Nanomoke 2 specifications'. Technical report.
- [LWG+10] M. I. Lukasiewicz, B. Witkowski, M. Godlewski, E. Guziewicz, M. Sawicki, W. Paszkowicz, R. Jakiela, T. A. Krajewski, and G. Luka. 'Effects related to deposition temperature of ZnCoO films grown by atomic layer deposition - uniformity of Co distribution, structural, optical, electrical and magnetic properties'. *Phys. Status Solidi B*, **247**:16661670, 2010.
- [LWGG+08] M. Lukasiewicz, A. Wojcik-Glodowska, M. Godlewski, E. Guziewicz, R. Jakiela, T. Krajewski, L. Wachnicki, A. Szczepanik, E. Lusakowska, W. Paszkowicz, R. Minikayev, M. Kiecana, and M. Sawicki. 'ZnCoO films obtained at low temperature by atomic layer deposition using organic zinc and cobalt precursors'. *Acta Phys. Pol. A*, **114**:1235–1240, 2008.
- [Mar94] C. R. Martin. 'Nanomaterials: A Membrane-Based Synthetic Approach'. *Science*, **266**:1961–1966, 1994.
- [Mar10] S. Martens. Private communication, 2010.
- [Mar11] S. Martens. Private communication, 2011.

- [MAW<sup>+</sup>01] H. Masuda, H. Asoh, M. Watanabe, K. Nishio, M. Nakao, and T. Tamamura. 'Square and triangular nanohole array architectures in anodic alumina'. *Adv. Mater.*, **13**:189–192, 2001.
- [MBE<sup>+</sup>07] G. Meier, M. Bolte, R. Eiselt, B. Kruger, D. H. Kim, and P. Fischer. 'Direct imaging of stochastic domain-wall motion driven by nanosecond current pulses'. *Phys. Rev. Lett.*, **98**:187202, 2007.
- [MDA09] J. Meier, B. Doudin, and J.-Ph. Ansermet. 'Magnetic-Properties Of Nanosized Wires'. *J. Appl. Phys.*, **79**:6010 – 6012, 2009.
- [MF95] H. Masuda and K. Fukuda. 'Ordered Metal Nanohole Arrays Made by a Two-Step Replication of Honeycomb Structures of Anodic Alumina'. *Science*, **268**:1466–1468, 1995.
- [MHO97] H. Masuda, F. Hasegawa, and S. Ono. 'Self-ordering of cell arrangement of anodic porous alumina formed in sulfuric acid solution'. *J. Electrochem. Soc.*, **144**:L127–L130, 1997.
- [MIB<sup>+</sup>11] X. Meng, M. Ionescu, M. Banis, Y. Zhong, H. Liu, Y. Zhang, S. Sun, R. Li, and X. Sun. 'Heterostructural coaxial nanotubes of CNT@Fe<sub>2</sub>O<sub>3</sub> via atomic layer deposition: effects of surface functionalization and nitrogen-doping'. *J. Nanopart. Res.*, **13**:1207–1218, 2011.
- [MJTD01] I. Mikulskas, S. Juodkazis, R. Tomasiunas, and J. G. Dumas. 'Aluminum oxide photonic crystals grown by a new hybrid method'. *Adv. Mater.*, **13**:1574–1577, 2001.
- [MKG<sup>+</sup>98] G. Meier, M. Kleiber, D. Grundler, D. Heitmann, and R. Wiesendanger. 'Vertical polarization of quantum magnets in high density arrays of nickel dots with small height-to-diameter ratio'. *Appl. Phys. Lett.*, **72**:2168–2170, 1998.
- [ML98] A. M. Morales and C. M. Lieber. 'A laser ablation method for the synthesis of crystalline semiconductor nanowires'. *Science*, **279**:208–211, 1998.
- [MM11] J. M. Montero-Moreno. Private communication, 2011.
- [MM12] J. M. Montero-Moreno. Private communication, 2012.
- [MRR<sup>+</sup>53] N. Metropolis, A. Rosenbluth, M. Rosenbluth, A. Teller, and E. Teller. 'Equation of State Calculations by Fast Computing Machines'. *J. Chem. Phys.*, **21**:1087–109, 1953.
- [MSM<sup>+</sup>02] K. Miyake, K. Shigeto, K. Mibu, T. Shinjo, and T. Ono. 'Geometrical confinement of a domain wall in a nanocontact between two NiFe wires'. *Appl. Phys. Lett.*, **91**:3468–3470, 2002.



- [MSP<sup>+</sup>11] J. Malm, E. Sahramo, J. Perala, T. Sajavaara, and M. Karppinen. 'Low-temperature atomic layer deposition of ZnO thin films: Control of crystallinity and orientation'. *Thin Solid Films*, **519**:5319–5322, 2011.
- [MTB90] H. Masuda, H. Tanaka, and N. Baba. 'Preparation Of Porous Material By Replacing Microstructure Of Anodic Alumina Film With Metal'. *Chem. Lett.*, pages 621–622, 1990.
- [MYO98] H. Masuda, K. Yada, and A. Osaka. 'Self-ordering of cell configuration of anodic porous alumina with large-size pores in phosphoric acid solution'. *Jap. J. Appl. Phys.*, **37**:L1340–L1342, 1998.
- [Neu06] I. Neudecker. '*Magnetization dynamics of confined ferromagnetic systems*'. PhD thesis, Universität Regensburg, 2006.
- [NHVV<sup>+</sup>07] D. Navas, M. Hernández-Vélez, M. Vázquez, W. Lee, and K. Nielsch. 'Ordered Ni nanohole arrays with engineered geometrical aspects and magnetic anisotropy'. *Appl. Phys. Lett.*, **90**:192501, 2007.
- [Nie02] K. Nielsch. '*Hochgeordnete ferromagnetische Nano-Stabensembles*'. PhD thesis, Martin-Luther-Universität Halle-Wittenberg, 2002.
- [NLF<sup>+</sup>04] O. Nilsen, M. Lie, S. Foss, H. Fjellvag, and A. Kjekshus. 'Effect of magnetic field on the growth of  $\alpha$ -Fe<sub>2</sub>O<sub>3</sub> thin films by atomic layer deposition'. *Appl. Surf. Sci.*, **227**:4047, 2004.
- [NMLG00] K. Nielsch, F. Muller, A. P. Li, and U. Gösele. 'Uniform nickel deposition into ordered alumina pores by pulsed electrodeposition'. *Adv. Mater.*, **12**:582–586, 2000.
- [NNP<sup>+</sup>04] L. Niinistö, M. Nieminen, J. Pääsaari, J. Niinistö, M. Putkonen, and M. Nieminen. 'Advanced electronic and optoelectronic materials by Atomic Layer Deposition: An overview with special emphasis on recent progress in processing of high-k dielectrics and other oxide materials'. *Phys. Stat. Sol. A*, **201**:1443–1452, 2004.
- [NWB<sup>+</sup>01] K. Nielsch, R. B. Wehrspohn, J. Barthel, J. Kirschner, U. Gösele, S. F. Fischer, and H. Kronmüller. 'Hexagonally ordered 100 nm period nickel nanowire arrays'. *Appl. Phys. Lett.*, **79**:1360–1362, 2001.
- [NWB<sup>+</sup>02] K. Nielsch, R. B. Wehrspohn, J. Barthel, J. Kirschner, S. F. Fischer, H. Kronmüller, T. Schweinbock, D. Weiss, and U. Gösele. 'High density hexagonal nickel nanowire array'. *J. Magn. Magn. Mater.*, **249**:234–240, 2002.
- [O'H00] R. C. O'Handley. '*Modern magnetic materials: Principles and applications*'. Wiley, 2000.

- [O'H01] R. C. O'Handley. 'Magnetic Materials'. In Robert A. Meyers, editor, *Encyclopedia of Physical Science and Technology*, pages 919 – 944. Academic Press, New York, 2001.
- [Olb88] B. Olbertz. 'Hartanodisieren eröffnet Aluminium vielfältige technische Anwendungsmöglichkeiten'. *Aluminium*, **3**:268–270, 1988.
- [ORZ<sup>+</sup>09] L. O'Brien, D. E. Read, H. T. Zeng, E. R. Lewis, D. Petit, and R. P. Cowburn. 'Bidirectional magnetic nanowire shift register'. *Appl. Phys. Lett.*, **95**:232502, 2009.
- [OSA04] S. Ono, M. Saito, and H. Asoh. 'Self-ordering of anodic porous alumina induced by local current concentration: Burning'. *Electrochem. Solid St.*, **7**:B21–B24, 2004.
- [OSIA04] S. Ono, M. Saito, M. Ishiguro, and H. Asoh. 'Controlling factor of self-ordering of anodic porous alumina'. *J. Electrochem. Soc.*, **151**:B473–B478, 2004.
- [OTK<sup>+</sup>06] R. Oriňáková, A. Turoňová, D. Kladeková, A. Gálová, and R. Smith. 'Recent developments in the electrodeposition of nickel and some nickel-based alloys'. *J. Appl. Electrochem.*, **36**:957–972, 2006.
- [Ozi92] G. A. Ozin. 'Nanochemistry: Synthesis in diminishing dimensions'. *Adv. Mater.*, **4**:612–649, 1992.
- [PBBMD08] L. Peraldo Bicelli, B. Bozzini, C. Mele, and L. D'Urzo. 'A Review of Nanostructural Aspects of Metal Electrodeposition'. *Int. J. Electrochem. Sci.*, **3**:356 – 408, 2008.
- [PCJD03] Q. A. Pankhurst, J. Connolly, S. K. Jones, and J. Dobson. 'Applications of magnetic nanoparticles in biomedicine'. *J. Phys. D Appl. Phys.*, **36**:R167–R181, 2003.
- [PDK<sup>+</sup>11] V. Pore, M. Dimri, H. Khanduri, R. Stern, J. Lu, L. Hultman, K. Kukli, M. Ritala, and M. Leskela. 'Atomic layer deposition of ferromagnetic cobalt doped titanium oxide thin films'. *Thin Solid Films*, **519**:3318–3324, 2011.
- [PHJ98] D. Y. Petrovykh, F. J. Himpsel, and T. Jung. 'Width distribution of nanowires grown by step decoration'. *Surf. Sci.*, **407**:189–199, 1998.
- [PHT08] S. S. P. Parkin, M. Hayashi, and L. Thomas. 'Magnetic Domain-Wall Racetrack Memory'. *Science*, **320**:190–194, 2008.
- [Pit09] K. Pitzschel. 'Atomic Layer Deposition'. *Welt der Physik*, <http://www.weltderphysik.de/gebiete/stoffe/duenne-schichten-und-oberflaechen/atomic-layer-deposition>, 12.06.2009.

- [PLK<sup>+</sup>01] P.M. Paulus, F. Luis, M. Kroll, G. Schmid, and L. J. de Jongh. 'Low-temperature study of the magnetization reversal and magnetic anisotropy of Fe, Ni, and Co nanowires'. *J. Magn. Magn. Mater.*, **224**:180–196, 2001.
- [PMME<sup>+</sup>09] K. Pitzschel, J. M. Montero-Moreno, J. Escrig, O. Albrecht, K. Nielsch, and J. Bachmann. 'Controlled introduction of diameter modulations in arrayed magnetic iron oxide nanotubes'. *ACS Nano*, **3**:3463–3468, 2009.
- [Pri94] G.A. Prinz. '*Magnetic Metal Films on Semiconductor Substrates*'. Springer, Berlin, 1994.
- [PS92] V.P. Parkhutik and V.I. Shershulsky. 'Theoretical Modelling of Porous Oxide Growth on Aluminium'. *J. Appl. Phys.*, **25**:1258, 1992.
- [Puu05] R. L. Puurunen. 'Surface chemistry of atomic layer deposition: A case study for the trimethylaluminum/water process'. *J. Appl. Phys.*, **97**:121301, 2005.
- [Qua08] QuantumDesign. '*QuantumDesign. vibrating sample magnetometer (VSM) option: User's manual*'. 2008.
- [RBZ<sup>+</sup>02] J. Rivas, A.K.M. Bantu, G. Zaragoza, M.C. Blanco, and M.A. Lopez-Quintela. 'Preparation and magnetic behavior of arrays of electrodeposited Co nanowires'. *J. Magn. Magn. Mater.*, **249**:220–227, 2002.
- [Rec07] K. Reckwell. '*Mikrowellenspektroskopie an ferromagnetischen Mikrostrukturen*'. Diploma thesis, Department Physik der Universität Hamburg, 2007.
- [Ren13] K. Renger. '*Die anfängliche Suszeptibilität von Eisen und Magnetit in Abhängigkeit von der Temperatur*'. PhD thesis, Technische Hochschule Zürich, 1913.
- [RFH<sup>+</sup>01] C. A. Ross, M. Farhoud, M. Hwang, H. I. Smith, M. Redjdal, and F. B. Humphrey. 'Micromagnetic behavior of conical ferromagnetic particles'. *J. Appl. Phys.*, **89**:1310–1319, 2001.
- [RGGV00] K. . Raposo, J.M. García, J.M. González, and M. Vázquez. 'Long-range magnetostatic interactions in arrays of nanowires'. *J. Magn. Magn. Mater.*, **222**:227–232, 2000.
- [RJK<sup>+</sup>08] M. Rooth, A. Johansson, K. Kukli, J. Aarik, M. Boman, and A. Harsta. 'Atomic Layer Deposition of Iron Oxide Thin Films and Nanotubes using Ferrocene and Oxygen as Precursors'. *Chem. Vapor Depos.*, **14**:67–70, 2008.

- [RKLD<sup>+</sup>01] J. Rothman, M. Kläui, L. Lopez-Diaz, C. A. F. Vaz, A. Bleloch, J. A. C. Bland, Z. Cui, and R. Speaks. 'Observation of a Bi-Domain State and Nucleation Free Switching in Mesoscopic Ring Magnets'. *Phys. Rev. Lett.*, **86**:1098–1101, 2001.
- [RPS<sup>+</sup>05] A. Rajendra, B. J. Parmar, A. K. Sharma, H. Bhojraj, M. M. Nayak, and K. Rajanna. 'Hard anodisation of aluminium and its application to sensorics'. *Surf. Eng.*, **21**:193–197, 2005.
- [SFS<sup>+</sup>03] W. Scholz, T. Fidler, J. Schrefl, D. Suess, H. Dittrich, R. Forster, and V. Tsiantos. 'Scalable Parallel Micromagnetic Solvers for Magnetic Nanostructures'. *Comp. Mater. Sci.*, **28**:366–383, 2003.
- [SMST04] S. Shingubara, K. Morimoto, H. Sakaue, and T. Takahagi. 'Self-organization of a porous alumina nanohole array using a sulfuric/oxalic acid mixture as electrolyte'. *Electrochem. Solid St.*, **7**:E15–E17, 2004.
- [SMV<sup>+</sup>98] C. Stamm, F. Marty, V. Vaterlaus, V. Weich, S. Egger, U. Maier, U. Ramsperger, H. Fuhrmann, and D. Pescia. 'Two-Dimensional Magnetic Particles'. *Science*, **282**:449–451, 1998.
- [SRL<sup>+</sup>09] I. L. Soroka, M. Rooth, J. Lu, M. Boman, P. Svedlindh, J. O. Carlsson, and A. Harsta. 'Template-based multiwalled TiO<sub>2</sub>/iron oxides nanotubes: Structure and magnetic properties'. *J. Appl. Phys.*, **106**:084313, 2009.
- [STRS63] S. Shtrikman, D. Treves, G. T. Rado, and H. Suhl. 'Micromagnetics'. in *Magnetism, Academic Press, New York* ., vol. III:415–461, 1963.
- [SW48] E. Stoner and E. C. Wohlfarth. 'A mechanism of Magnetic Hysteresis in Heterogeneous Alloys'. *Philos. T. R. Soc. A*, **A240**:599, 1948.
- [THGRB09] J. M. Thomas, J. C Hernandez-Garrido, R. Raja, and R. G. Bell. 'Nanoporous oxidic solids: the confluence of heterogeneous and homogeneous catalysis'. *Phys. Chem. Chem. Phys.*, **11**:2799–2825, 2009.
- [TJCF92] R. J. Tonucci, B. L. Justus, A. J. Campillo, and C. E. Ford. 'Nanochannel Array Glass'. *Science*, **258**:783–785, 1992.
- [TK80] M. Tinkharn and R.E. Krieger. '*Introduction to Superconductivity*'. Pubnet, 1980.
- [TL10] D. D. Tang and Y. J. Lee. '*Magnetic memory : Fundamentals and technology*'. Cambridge University Press, 2010.
- [TW81] G. E. Thompson and G. C. Wood. 'Porous Anodic Film Formation On Aluminum'. *Nature*, **290**:230–232, 1981.

- [UEK11] K. Uusi-Esko and M. Karppinen. 'Extensive series of hexagonal and orthorhombic  $\text{RMnO}_3$  ( $R = \text{Y, La, Sm, Tb, Yb, Lu}$ ) thin films by atomic layer deposition'. *Chem. Mater.*, **23**:1835–1840, 2011.
- [UERL<sup>+</sup>10] K. Uusi-Esko, E.-L. Rautama, M. Laitinen, T. Sajavaara, and M. Karppinen. 'Control of oxygen nonstoichiometry and magnetic property of  $\text{MnCo}_2\text{O}_4$  thin films grown by atomic layer deposition'. *Chem. Mater.*, **22**:6297–6300, 2010.
- [VBM<sup>+</sup>12] V. Vega, T. Böhnert, S. Martens, M. Waleczek, L. Akinsinde, J.M. Montero-Moreno, D. Görlitz, V.M. Prida, and K. Nielsch. 'Tuning the magnetic anisotropy of Co-Ni nanowires: Comparison between single nanowires and nanowire arrays in hard-anodic alumina membranes'. *submitted*, 2012.
- [WC09] D. B. Williams and C. B. Carter. '*The Transmission Electron Microscope*'. Springer, Berlin, 2009.
- [WFAvM98] S. Wirth, M. Field, D. D. Awschalom, and S. von Molnár. 'Magnetization behavior of nanometer-scale iron particles'. *Phys. Rev. B*, **57**:R14028, 1998.
- [WJSC93] T. M. Whitney, J. S. Jiang, P. C. Searson, and C. L. Chien. 'Fabrication and magnetic-properties of arrays of metallic nanowires'. *Science*, **261**:1316–1319, 1993.
- [WNU04] R. Wieser, U. Nowak, and K. D. Usadel. 'Domain wall mobility in nanowires: Transverse versus vortex walls'. *Phys. Rev. B*, **69**:064401, 2004.
- [WO70] G. C. Wood and J. P. O'Sullivan. 'Anodizing of aluminium in sulphate solutions'. *Electroch. Ac.*, **15**:1865, 1970.
- [WSYB86] K. Wada, T. Shimohira, M. Yamada, and N. Baba. 'Microstructure of porous anodic oxide-films on aluminum'. *J. Mater. Sci.*, **21**:3810–3816, 1986.
- [XKD<sup>+</sup>01] T. Xu, H.-C. Kim, J. DeRouchey, C. Seney, C. Levesque, P. Martin, C.M. Stafford, and T.P. Russell. 'The influence of molecular weight on nanoporous polymer films'. *Polymer*, **42**:9091–9095, 2001.
- [XYS<sup>+</sup>03] Y. Xia, P. Yang, Y. Sun, Y. Wu, D. B. Mayers, B. Gates, Y. Yin, F. Kim, and Y. Yan. 'One-dimensional nanostructures: Synthesis, characterization, and applications'. *Adv. Mater.*, **15**:353–389, 2003.
- [YAK<sup>+</sup>11] M. Yan, C. Andreas, A. Kakay, F. Garcia-Sanchez, and R. Hertel. 'Fast domain wall dynamics in magnetic nanotubes: Suppression of Walker breakdown and Cherenkov-like spin wave emission'. *Appl. Phys. Lett.*, **99**:122505, 2011.

- [YLK<sup>+</sup>08] S. S. Yim, D. J. Lee, K. S. Kim, S. H. Kim, T. S. Yoon, and K. B. Kim. 'Nucleation kinetics of Ru on silicon oxide and silicon nitride surfaces deposited by atomic layer deposition'. *J. Appl. Phys.*, **103**:113509, 2008.
- [YZL05] C. Yang, D. Z. Zhong, and C.M. Lieber. 'Encoding electronic properties by synthesis of axial modulation-doped silicon nanowires'. *Science*, **310**:1304–1307, 2005.
- [ZBMM<sup>+</sup>11] A. Zolotaryov, J. Bachmann, J. M. Montero-Moreno, K. Pitzschel, and K. Nielsch. 'Processing of hollow micro- and nanostructures using the hydrophilic nature of MgO'. *Precis. Eng.*, **35**:496–499, 2011.
- [ZLZ<sup>+</sup>06] L. Zhao, T. Lu, M. Zacharias, J. Yu, J. Shen, H. Hofmeister, M. Steinhart, and U. Gösele. 'Integration of Erbium-Doped Lithium Niobate Microtubes into Ordered Macroporous Silicon'. *Adv. Mater.*, **18**:363–366, 2006.
- [ZWB<sup>+</sup>11] R. Zierold, Z. Y. Wu, J. Biskupek, U. Kaiser, J. Bachmann, C. E. Krill, and K. Nielsch. 'Magnetic, multilayered nanotubes of low aspect ratios for liquid suspensions'. *Adv. Func. Mater.*, **21**:226–232, 2011.
- [ZYN<sup>+</sup>01] H. Zhu, S. G. Yang, G. Ni, D. L. Yu, and Y. W. Du. 'Study on magnetic property of Fe<sub>14</sub>Ni<sub>86</sub> alloy nanowire array'. *J. Magn. Magn. Mater.*, **234**:454–458, 2001.

# A. Appendix

## A.1. ALD process parameters

SiO <sub>2</sub>				
Precursor	Temperature	Pulse time	Exposure time	Pumping time
3-aminopropyl-triethoxysilane	100°C	2 s	20 s	20 s
water	50°C	0.5 s	20 s	25 s
ozone	room temp.	0.2 s	20 s	20 s
Chamber temperature	150°C			
Flush gas	nitrogen flow 40 sccm			
Deposition rate	0.6 Å cycle <sup>-1</sup>			

**Table A.1.:** Parameter for the deposition of SiO<sub>2</sub> process.

Fe <sub>2</sub> O <sub>3</sub>				
Precursor	Temperature	Pulse time	Exposure time	Pumping time
ferrocene	100°C	2 s	20 s	20 s
ozone	room temp.	0.2 s	20 s	20 s
Chamber temperature	200°C			
Flush gas	nitrogen flow 40 sccm			
Deposition rate	0.2 Å cycle <sup>-1</sup>			

**Table A.2.:** Parameter for the deposition of Fe<sub>2</sub>O<sub>3</sub> process.

NiO				
Precursor	Temperature	Pulse time	Exposure time	Pumping time
nickelocene	80°C	2 s	20 s	30 s
ozone	room temp.	0.2 s	20 s	20 s
Chamber temperature	220°C			
Flush gas	nitrogen flow 20 sccm			
Deposition rate	0.1 Å cycle <sup>-1</sup>			

**Table A.3.:** Parameter for the deposition of NiO process.

NiCo				
Precursor	Temperature	Pulse time	Exposure time	Pumping time
nickelocene/ cobaltocene (mixing ratio: 50 : 50)	80°C	2 s	10 s	30 s
ozone	room temp.	0.2 s	10 s	20 s
Chamber temperature	220°C			
Flush gas	nitrogen flow 20 sccm			
Deposition rate	0.1 Å cycle <sup>-1</sup>			

**Table A.4.:** Parameter for the deposition of NiCo process.



# B. Appendix

## B.1. Figures

### B.1.1. Ni tubes hysteresis loops

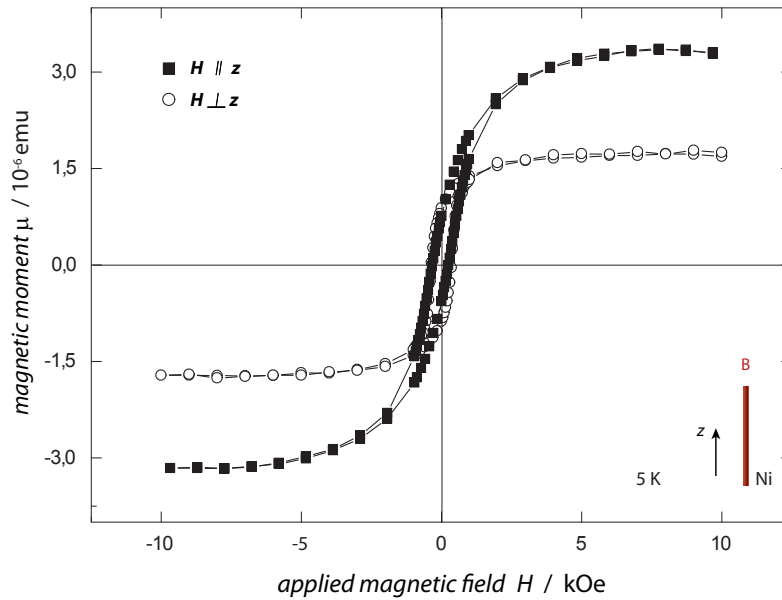


**Figure B.1.:** Magnetic hysteresis loops of the second sample of *Ni* nanotubes (10 nm wall thickness) in a field applied parallel to the long axis ( $z$  axis) of the tubes at 5 K. The coercive fields are not affected by the orientation of the sample ( $H_c^{\parallel} = 328 \text{ Oe}$  and  $H_c^{\perp} = 328 \text{ Oe}$ ); The remance differs 50 % from  $\mu_{rem}^{\parallel} = 0.4 \mu_{sat}$  to  $\mu_{rem}^{\perp} = 0.8 \mu_{sat}$ . Here also no shape anisotropy can be seen

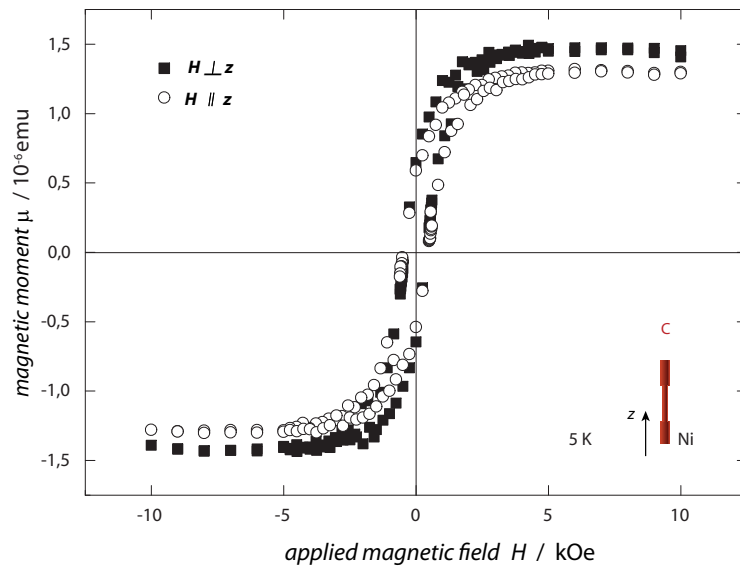


**Figure B.2.:** The last sample of the Ni tube samples is also measured at 5 K: The various orientations with respect to the applied field are shown: the coercive fields ( $H_c^{\parallel} = 430$  Oe and  $H_c^{\perp} = 430$  Oe) are the same, the remance ( $\mu_{rem}^{\parallel} = 0.45 \mu_{sat}$  and  $\mu_{rem}^{\perp} = 0.35 \mu_{sat}$ ) is 10 % smaller in perpendicular configuration to the applied field.

### B.1.2. Nickel/ cobalt tubes hysteresis loops

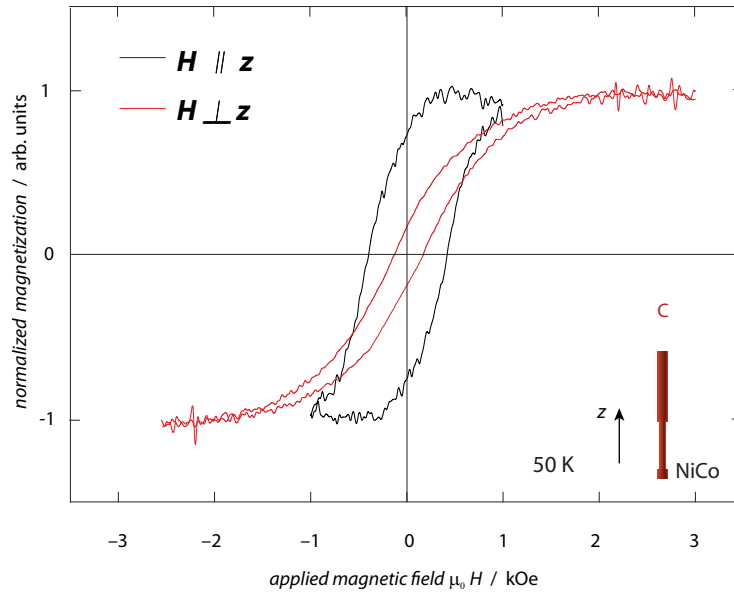


**Figure B.3.:** Magnetic hysteresis loops of an array of nickel/ cobalt nanotubes (10 nm wall thickness) in a field applied parallel to the long axis ( $z$  axis) of the tubes at 50 K. Both the coercive field  $H_c$  ( $x$  intercept) and the remanence  $\mu_{rem}$  ( $y$  intercept) are strongly affected by the orientation of the sample  $H_c^{\parallel} = 428$  Oe;  $\mu_{rem}^{\parallel} = 0.7 \mu_{sat}$  and  $H_c^{\perp} = 126$  Oe;  $\mu_{rem}^{\perp} = 0.2 \mu_{sat}$ . Anodization conditions of the template: mild 10  $\mu\text{m}$  and hard 8  $\mu\text{m}$ , and mild 1  $\mu\text{m}$ .

## B.2. Simulation figures of Ni nanowires

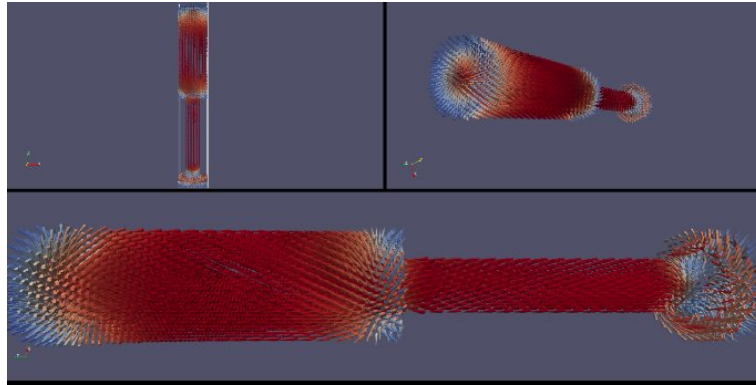


**Figure B.4.:** Snapshot of the simulated spin configuration of wire A at an applied field done by OOMMF[Esc10].

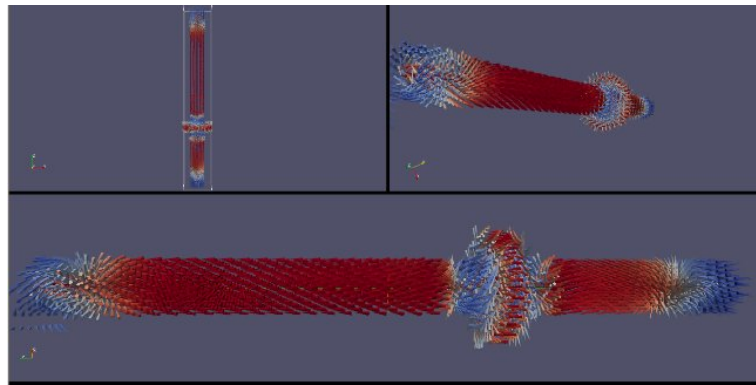


**Figure B.5.:** Snapshot of the simulated spin configuration of wire B at an applied field done by OOMMF[Esc10].

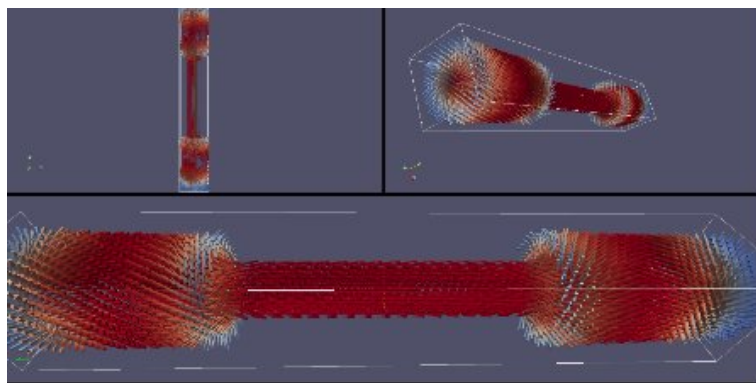


**Figure B.6.:** Snapshot of the simulated spin configuration of wire D at an applied field done by OOMMF[Esc10].

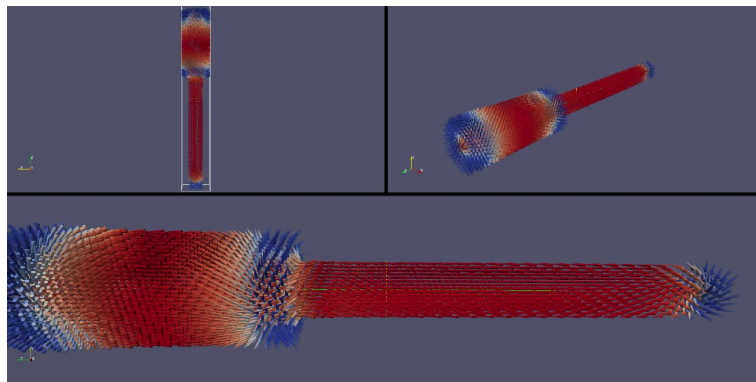


**Figure B.7.:** Snapshot of the simulated spin configuration of wire E at an applied field done by OOMMF[Esc10].

## C. Appendix

### C.1. Publications

- [1] Kristina Pitzschel, 'Atomic Layer Deposition', Welt der Physik, 12.06.2009, <http://www.weltderphysik.de/gebiete/stoffe/duenne-schichten-und-oberflaechen/atomic-layer-deposition> Atomlagenabscheidung
- [2] Kristina Pitzschel, Josep M. Montero Moreno, Juan Escrig, Ole Albrecht, Kornelius Nielsch, and Julien Bachmann. 'Controlled introduction of diameter modulations in arrayed magnetic iron oxide nanotubes', *ACS Nano*, **3**:3463–3468, 2009
- [3] Julien Bachmann, Juan Escrig, Kristina Pitzschel, Josep M. Montero Moreno, Jing Jing, Detlef Görlitz, Dora Altbir, and Kornelius Nielsch. 'Size effects in ordered arrays of magnetic nanotubes: Pick your reversal mode', *J. Appl. Phys.*, **105**:07B521, 2009
- [4] Andriy Zolotaryov, Julien Bachmann, Josep M. Montero Moreno, Kristina Pitzschel, and Kornelius Nielsch. 'Processing of hollow micro- and nanostructures using the hydrophilic nature of MgO', *Precis. Eng.*, **35**:496–499, 2011
- [5] Kristina Pitzschel, Julien Bachmann, Stephan Martens, Josep M. Montero-Moreno, Judith Kimling, Guido Meier, Kornelius Nielsch, Detlef Görlitz, and Juan Escrig. 'Magnetic reversal of cylindrical nickel nanowires with modulated diameters', *J. Appl. Phys.*, **109**:033907, 2011

### C.2. Presentations

- [03/2009] DPG spring conference of section condensed matter in Dresden  
*Posterpresentation*: Kristina Pitzschel, Josep M. Montero Moreno, Julien Bachmann, Ole Albrecht and Kornelius Nielsch. 'Magnetic nanowires and tubes with modulated diameter based on ordered  $Al_2O_3$  membranes'
- [03/2009] DPG spring conference of section condensed matter in Regensburg  
*Posterpresentation*: Kristina Pitzschel, Julien Bachmann, Stephan Martens, Josep M. Montero Moreno, Juan Escrig, Kornelius Nielsch and Detlef Görlitz. 'Ensemble and single-object measurements of magnetic nanowires with modulated diameter'
- [08/2010] Joint European Magnetic Symposia (JEMS) in Krakau  
*Posterpresentation*: Kristina Pitzschel, Julien Bachmann, Stephan Martens, Josep M. Montero Moreno, Juan Escrig, Mohamed S. Salem, Kornelius Nielsch and Detlef Görlitz. 'Characterization of complex magnetic nanotubes'
- Posterpresentation*: Kristina Pitzschel, Julien Bachmann, Stephan Martens, Josep M. Montero Moreno, Mohamed S. Salem, Juan Escrig, Kornelius Nielsch and

Detlef Görlitz. 'Ensemble and single-object measurements of magnetic nanowires with modulated diameter'

[12/2011] CINaM-CNRS, France

*Invited Talk* : 'Magnetic nanotubes with modulated diameter based on perfectly ordered Al<sub>2</sub>O<sub>3</sub> membranes'

## Acknowledgements

Many people have contributed to the production of my thesis, so I owe my gratitude to all those people without whose motivation, support, encouragement, supervision, patience, confidence, and companionship would not have been possible.

My deepest gratitude is to Prof. Dr. *K. Nielsch* for supervising my thesis, his encouragement, motivation, support and for admitting me in his group.

I thank Dr. *D. Görlitz*, for the great supervision and who has been always there to listen and give advice. I am deeply grateful to him for the long discussions.

Prof. Dr. *M. Albrecht* for being the referee of the dissertation and Prof. Dr. *H.-P. Oepen* for being the referee of the defense.

Jun. Prof. Dr. *J. Bachmann*, has been always there to listen and give advice. I am deeply grateful to him for the long discussions.

Prof. Dr. *J. Escrig* for the major support in calculating theoretical models for my nanostructures.

Prof. Dr. *M. Eich* for the opportunity to use the TEM of the TUHH and I. Bucher and F. Riazi for the technical support.

Dr. *J. M. Montero-Moreno* for interesting discussions, for encouragement and practical advice and support.

Dr. *O. Albrecht* for his interest in the work, advice and support concerning the SQUID.

Dr. *A. Zolotaryov* for technical support concerning ALD.

Dr. *Y. T. Chong* for technical support concerning ALD.

*S. Martens* for sharing his insight into theory, for his interest in the work and unwavering support.

*R. Zierold* for advice and support concerning the SQUID and the ALD.

*M. Waleczek* for advice and support concerning the SQUID.

*L. Akinsinde* for technical support and for commenting on my reports.

*A. Abel* for always supporting me with the TEM measurements.

*T. Böhnert* for advice and support concerning the VSM.

*P. Sergelius* for support concerning the VSM and especially VSM measurements.

*R. Meissner* for the technical advice and support.

*J. Kimling* for interesting discussions and MFM measurements.

*I. Klüver* and *S. Baer* for the support concerning the administration.

The whole *group K* for support and interesting discussions.

*R.-P. Benecke* and the whole mechanical workshop for technical support.

*H. Biedermann* and the whole electronical workshop for technical support.

*T. Krugmann* for the chemical analysis of my samples.

*My family, my parents* and *C. Usupova* for always supporting me with the and *my husband*.



Eidesstattliche Erklärung

Ich versichere an Eides statt, dass ich die Inanspruchnahme fremder Hilfen  
aufgeführt habe, sowie, dass ich die wörtlich oder inhaltlich aus anderen Quellen  
entnommenen Stellen als solche kenntlich gemacht habe.

Kristina Pitzschel

Hamburg, den 16. Februar 2012